Doklady Physics, Vol. 47, No. 10, 2002, pp. 709–711. Translated from Doklady Akademii Nauk, Vol. 386, No. 5, 2002, pp. 606–608.

PHYSICS

Temperature Dependence for the Frequency Position of the Low-Frequency Dielectric Dispersion in the Polyacenequinone Spectrum and Quantum Measurements

R. V. Afanas'eva, T. G. Ermakova, A. A. Maksimov, and Academician M. G. Voronkov

Received June 11, 2002

The current state of the art in the physics of mesoscopic and strongly correlated electron systems [1] necessitates an appeal to the conceptual tenets of quantum mechanics [2, 3]. We associate the low-frequency (LF) dispersion region in the dielectric spectrum of polyacenequinone (PAQ) synthesized by polycondensation of pyrene with pyromellitic dianhydride at 300°C with the phenomenon of quantum coherence in a system of donor–acceptor (D–A) complexes. We imply a system of atmospheric oxygen intercalated into graphite-like fragments of the surface-layer structure of PAQ granules and two-dimensional polyaromatic layers [4]. In the present paper, the temperature behavior of the LF maximum in the frequency dependence of the tangent $\tan\delta(\nu)$ of the dielectric-loss angle $\delta(\nu)$ is interpreted on the basis of a scheme of quantum measurements that was recently proposed [3]. For definiteness, we assume that the intercalated oxygen interacts with the π-conjugate system of only one of the adjacent polyaromatic layers. The problem of possible elementary mechanisms of the relaxation polarization is beyond the scope of the present discussion.

In the temperature dependence of the position $\nu_{m\,LF}$ of the LF maximum of $\tan\delta(\nu)$, a plateau similar to that of the rate constant for tunnel chemical reactions [5] is observed (Fig. 1a, segment *I*). This plateau has the meaning of a low-temperature limit for the electron-tunneling rate and, as a rule, is replaced by the activation dependence only upon elevation of temperature. This behavior is also characteristic of known examples in which tunneling is revealed in the phenomenon of dielectric polarization [6]. Such behavior corresponds to the well-known concept of an increase in the probability of above-barrier transitions compared to tunneling under these conditions. From this standpoint, the dependence $\nu_{m\,LF}(T)$ is unusual. As is seen from Fig. 1a (segment *I*), electron tunneling is observed at higher temperatures compared to the corresponding activation dependences (segment *II*). In this case, an attribute of the activation behavior is a shift of the maximum of $\tan\delta(\nu)$ towards low frequencies at –90°C (Fig. 1b). However, according to [7], the effect of dissipative processes in a medium does not always accelerate the tunneling reaction, and as $T \longrightarrow 0$ K, a quantum particle may be localized in a potential well of the initial state. Using this conclusion for interpreting the dependence $\nu_{m\,LF}(T)$, we should associate segment *II* in Fig. 1a (in the simplest structure model) with the passage from the tunneling of an electron in the two-well potential, which is induced by an alternating electric field, to the localization of the electron in the donor part of the D–A complex.

The effect of dissipative processes in a medium on the tunneling kinetics is considered, not only in the quasiclassical approximation [7], but as a violation of the coherence in the quantum system [8]. With allowance for the existing concepts of open continuously measurable quantum systems, the process of coherence violation is associated with quantum measurements, since, in this model, the medium plays the role of a measuring device [3, 9, 10]. This implies that the electron localization in the donor part of the D–A complex at a temperature of –90°C may be considered the result of a quantum measurement. In this case, segments *I* and *II* in Fig. 1a are, respectively, the macroscopic manifestation of the coherent superposition of two alternative results of the quantum measurement and the choice of one of them. A hypothetical segment *III* (Fig. 1a) could correspond to the realization of the second choice (electron localization on the acceptor). In this case, evidently, at temperatures exceeding room temperature, a shift of the maximum of $\tan\delta(\nu)$ towards high frequencies should be observed (Fig. 1b). In principle, this is possible under certain experimental conditions. In such an interpretation, the appearance of the temperature dependence in the rate of the LF relaxation process beyond the plateau from the sides of both low and high temperatures has the following natural explanation: in

Favorsky Irkutsk Institute of Chemistry, Siberian Division, Russian Academy of Sciences, ul. Favorskogo 1, Irkutsk, 664033 Russia

1028-3358/02/4710-0709$22.00

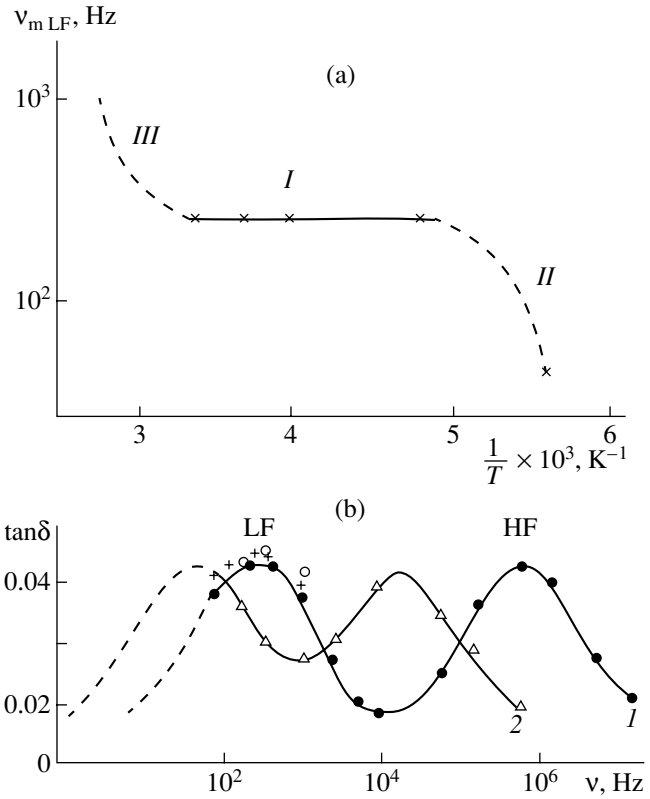

Fig. 1. (a) Temperature dependence of the position $\nu_{m\,LF}$ of the low-frequency maximum for the tangent of the dielectric-loss angle ($\tan\delta$) in the spectrum of a composite containing a mixture of PAQ granules with paraffin (polymer concentration is 10%; specimen thickness is 242 μm; diameter of electrodes is 15 mm). Experimental points of segment *I* correspond to the data of Fig. 1b. Segment *II* demonstrates a shift of the low-frequency maximum for $\tan\delta(\nu)$ towards low frequencies (see Fig. 1b). In this case, values of $\nu_{m\,LF}$ correspond to an approximate estimate. (b) Frequency dependence of the low-frequency (LF) maximum of $\tan\delta(\nu)$ for the same specimen at temperatures: (*1*) 20; (*2*) –90; (Δ) 0; (○) 20; (+) –60°C. Frequency dependences of the high-frequency (HF) maximum of $\tan\delta(\nu)$ at the same temperatures are not shown.

both cases, the activation behavior is associated with the incoherence phenomenon [3]. It turns out that by varying the temperature, we are capable of parametrically controlling the rather fine mechanism of the choice of alternative possibilities in quantum measurements. Parametric control of the collective reaction of a system of bistable quantum elements in the surface layer of PAQ granules can be realized on the basis of the quantum-measurement scheme proposed by Menskiĭ [3]: a system ⟷ a microsensor ⟷ a reservoir.

The basis of this scheme is the author's conception of a reversible incoherence, which is possible provided that the interaction of the medium and the quantum system being measured is limited by the small number of the degrees of freedom at a microscopic or mesoscopic structural level. These selected degrees of freedom are functionally equivalent to a microsensor, i.e., to a device in which the quantum information is recorded [3]. This possibility arises due to the appearance as a result of the interaction of a two-content entangled (quantum-correlated) state of an Einstein–Podolsky–Rosen (EPR) pair [2, 3, 10]. With allowance for this model, we may assume that an external alternating electric field reads out the quantum information recorded in the polarized state of the microsensor and transformed by it into a macroscopic information signal, namely, the maximum of $\tan\delta(\nu)$ (Fig. 1b). The plateau region in the dependence $\nu_{m\,LF}(T)$ (Fig. 1a) corresponds to the state of reversible incoherence.

The transition from reversible incoherence to irreversible incoherence is accompanied by the disappearance of the coherent-superposition contribution to the polarization of the medium (Fig. 1a, segment *I*). This transition occurs in accordance with the scheme of [3] and has a reservoir that also corresponds to a part of the environment for the quantum system being measured but possesses, however, a considerably larger number of degrees of freedom. The author of [3] did not discuss the problem of the interior functional system of this block. We assume that it can be defined as an ordered system of these degrees of freedom, which possesses an information behavior involving a stage of analog processing of information [4]. The realization of the functions of the parametric control in such a system may be represented as a certain sequence of elementary events that is caused by quantum correlations and whose chain penetrates the entire structure of temporal hierarchies and connects quantum and mesoscopic levels. The final result is the formation of particular steric conditions promoting or preventing electron transport in D–A complexes.

The scheme of quantum measurements proposed in [3] is in fact close to the principle of the functional integration that represents the basis of an approach to controlling quantum processes in the context of the theory of automatic control systems with distributed parameters, which was developed in [11, 12]. The suggested interpretation of the phenomenon of the irreversible incoherence in the quantum-measurement scheme allows us to make the following assumption. We may assume that the function of an analog control device can be realized with respect to a system of D–A bonds in the surface layer of PAQ granules as a result of the regulatory properties of the polymeric surface layer in itself.

In biological objects, a similar mechanism of analog information processing and decision making apparently acts at the level of cell membranes. At the same time, in solid-state structures, this occurs at the level of interface surfaces and is associated with the phenomenon often called interphase polarization [13]. As follows from the above, there exists a basis for the development of a nontraditional approach to studies of mechanisms regulating nonequilibrium surface pro-

cesses. This basis consists in the integration of the physics of polarizable media and the physics and chemistry of high-molecular compounds, as well as the theory of automatic control of systems with distributed parameters.

REFERENCES

1. M. V. Feĭgel'man, V. V. Ryazanov, and V. B. Timofeev, Usp. Fiz. Nauk **171**, 1099 (2001).
2. B. B. Kadomtsev, *Dynamics and Information* (Red. Zhurnala Usp. Fiz. Nauk, Moscow, 1997).
3. M. B. Menskiĭ, *Quantum Measurements and Incoherence: Models and Phenomenology* (Kluwer, Dordrecht, 2000; Fizmatlit, Moscow, 2001).
4. R. V. Afanas'eva, A. A. Maksimov, and T. G. Ermakova, Dokl. Akad. Nauk **381**, 469 (2001) [Dokl. Phys. **46**, 829 (2001)].
5. K. I. Zamaraev, R. F. Khairutdinov, and V. P. Zhdanov, *Tunneling of Electrons in Chemistry* (Nauka, Novosibirsk, 1985).
6. M. P. Tonkonogov, V. A. Veksler, and E. F. Orlova, Izv. Vyssh. Uchebn. Zaved., Fiz., No. 1, 97 (1982).
7. Yu. I. Dakhnovskiĭ, A. A. Ovchinnikov, and M. B. Semenov, Zh. Éksp. Teor. Fiz. **92**, 955 (1987) [Sov. Phys. JETP **65**, 541 (1987)].
8. A. D. Zaikin and S. V. Panyukov, Zh. Éksp. Teor. Fiz. **91**, 1677 (1986) [Sov. Phys. JETP **64**, 991 (1986)].
9. M. B. Menskiĭ, Usp. Fiz. Nauk **168**, 1017 (1998).
10. I. V. Bargatin, B. A. Grishanin, and V. N. Zaĭtsev, Usp. Fiz. Nauk **171**, 625 (2001).
11. A. G. Butkovskiĭ and Yu. I. Samoĭlenko, *Control of Quantum-Mechanical Processes and Systems* (Nauka, Moscow, 1984; Kluwer, Dordrecht, 1990).
12. Y. I. Samoĭlenko, V. F. Gubarev, and Yu. G. Krivonos, *Control of Fast Processes in Thermonuclear Facilities* (Naukova Dumka, Kiev, 1988).
13. N. G. Ryvkina, I. A. Chmutin, and A. T. Ponomarenko, Izv. Vyssh. Uchebn. Zaved., Fiz., No. 9, 1750 (2000).

Translated by G. Merzon

Doklady Physics, Vol. 47, No. 10, 2002, pp. 712–714. Translated from Doklady Akademii Nauk, Vol. 386, No. 5, 2002, pp. 609–611.

PHYSICS

Surface Waves Induced by Breakdown

M. Yu. Volokobinskiĭ, Yu. M. Volokobinskiĭ, J. Kaufhold, and A. S. Sotenko

Presented by Academician Yu.V. Gulyaev June 11, 2002

Received June 11, 2002

Acoustic waves in solids are actively studied. The effect of acoustic oscillations on the mobility of charge carriers and electrical conductivity were studied in [1, 2].

In semiconductor samples, where a strong-field region is produced in *p–n* junctions, we observed surface waves that accompany a breakdown and propagate from sources of concentrated energy release.

In the micrographs taken on optical (Fig. 1) and electron (Fig. 2) microscopes, three developed and one incomplete breakdown channels are seen (at the initial stage, several breakdown channels can be formed); channels *1* and *2* partially overlap.

In the lower part of channels *1*, *2*, and *4*, "solidified" waves generated by the explosive energy release upon a breakdown are seen. Wave crests are separated by 25–70 μm, and the channel length and width are equal to ~300 and ~150 μm, respectively.

The waves can be photographed, because a molten film is formed on the surface and is rapidly solidified in a time less than the period of wave propagation. Taking into account the velocity of acoustic waves, we find that the period of waves is equal to 15–50 ns. Thermal calculations indicate that the thickness of the molten layer does not exceed fractions of a micron, and the temperature jump between the molten layer and crystal is several hundred degrees.

In the breakdown channels (Figs. 2 and 3) at the boundary between C^+ and C^-, as well as at the boundary between C^- and B, thin grooves intersecting the breakdown channels in the transverse direction are observed. The length, average depth and width, and volume of a groove are equal to ~150, 10 μm, and $\sim 1.5 \times 10^{-5}$ mm^3, respectively. The small sizes of grooves indicate that the process is short-term.

In the micrographs (Figs. 2 and 4), it is seen that a substance evaporates and is ejected from grooves. Therefore, temperature reached 2783 K (for silicon) and 1693 K on the boundary molten surface. An energy of 7.2×10^{-4} and $\sim 1.5 \times 10^{-3}$ J is expended on forming one and two grooves in the channel, respectively (taking into account short-term energy losses due to thermal conductivity). The 0.1-μm-thick layer over the surface B and the 1-μm-thick layer over the surface C^- melt in 1 and 10 ns, respectively. An energy of 0.12 mJ is expended in one channel. The total energy expenditure on forming the breakdown channel is equal to 2 mJ.

Samples under a blocking voltage of 800–1000 V are periodically exposed to gate voltage pulses. The pulse duration is from 1 μs up to tens of milliseconds, and the pulse period-to-pulse duration ratio is no less than 100. At a current of 15 A, voltage of 800 V, and dissipated power of 12 kW, an energy of 2.4 mJ is released in 200 ns. During this time, the energy is accumulated and released through explosive evaporation.

A breakdown is indicated if blocking voltage is not restored after the end of a pulse.

A voltage pulse gives rise to the redistribution of the electric field and creates conditions for breakdown development. The electric field is redistributed in a time depending on the time it takes for charge carriers to penetrate through the layer C^-, which is equal to about 2 ns.

A gate voltage pulse initiates the energy release and heating of the surface layer. Near the region B, electrons compensate for the positive space charge. As a result, the strong-field region is displaced toward the highly doped region C^+. Under the action of the strong field in the region C^-, electrons cover a distance of 100 μm in approximately 1 ns, and the strong-field region is displaced by the same distance from the boundary of the region B. Therefore, conditions suitable for ionization processes are produced. The rate of these processes increases when the thickness of the

St. Petersburg State University of Telecommunications, ul. Moĭka 61, St. Petersburg, 191186 Russia

1028-3358/02/4710-0712$22.00

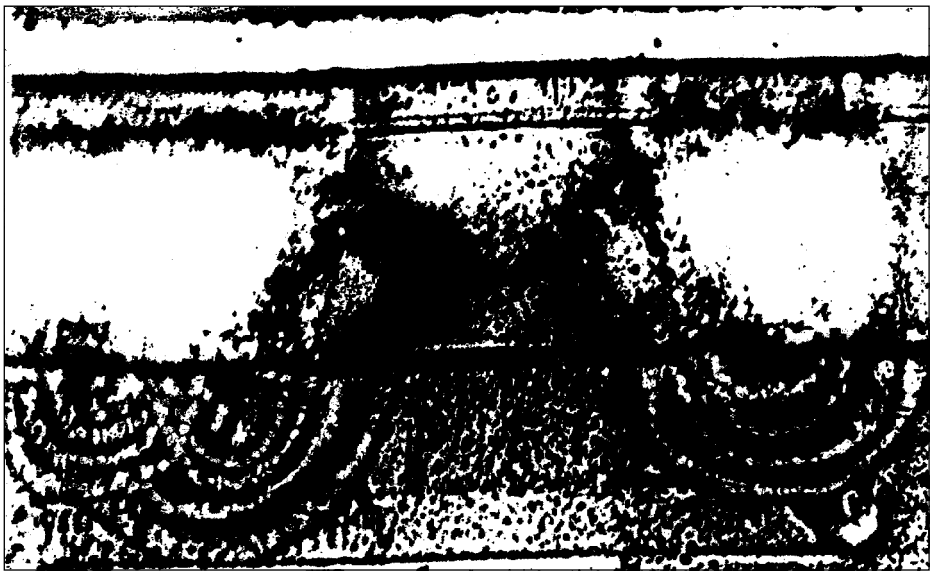

Fig. 1. Tracks of shock waves fixed in the solidified film of the melt on the surface of the breakdown channel (optical microscope).

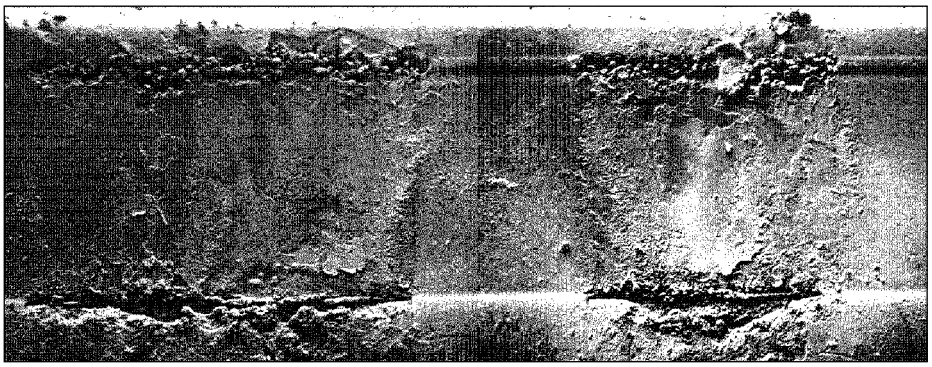

Fig. 2. Breakdown channels (electron microscope).

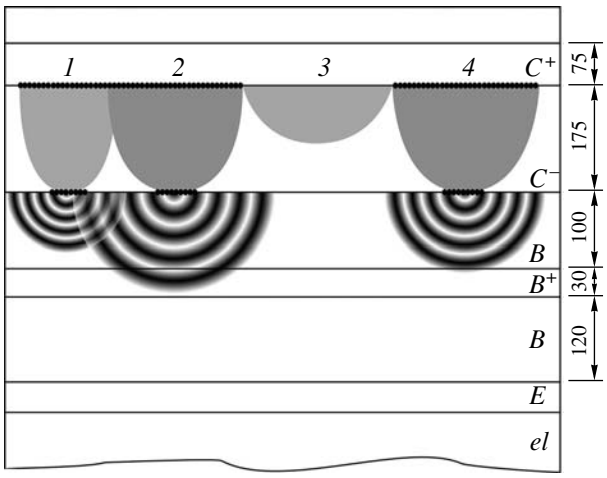

Fig. 3. Schematic image of the sample; *1*, *2*, *3*, and *4* are the breakdown channels; *el* is the electrode; C^+, C, C^-, and E are the *n*-type regions; B and B^+ are the *p*-type regions; resistivities of the regions are equal to (C^+) 0.002, (C) 15, (C^-) 50, (B) 0.06, and (B^+) 0.001 Ω cm, respectively.

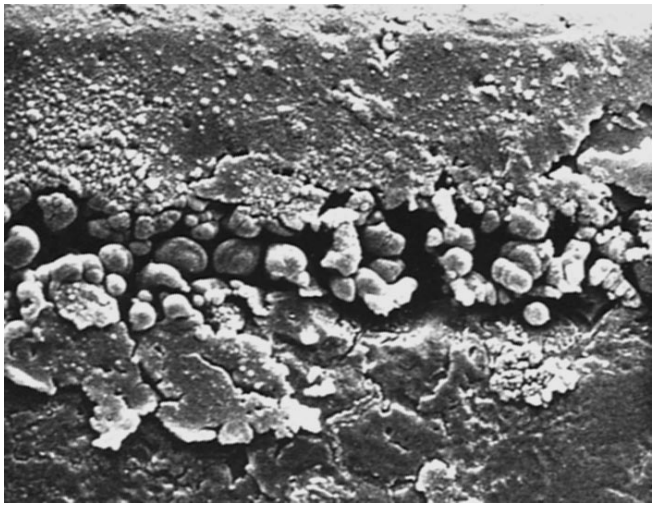

Fig. 4. Tracks of the material melting in the transverse groove of the breakdown channel (electron microscope).

space charge decreases to 15 μm. As a result, the substance in the groove at the C^+–C^- boundary evaporates. Holes formed in the process of ionization are driven by the field and transferred to region *B*, where they recombine.

The generation of shock waves is caused by the repeated redistribution of the electric field, as well as by the processes of impact ionization and recombination of charge carriers.

REFERENCES

1. Yu. P. Kuznetsov, V. V. Novikov, É. E. Pakhomov, and V. A. Chetskiĭ, Pis'ma Zh. Tekh. Fiz. **15** (5), 88 (1989) [Sov. Tech. Phys. Lett. **15**, 202 (1989)].
2. V. V. Novikov, R. R. Vardanyan, and É. E. Pakhomov, Fiz. Tekh. Poluprovodn. (St. Petersburg) **34** (5), 625 (2000) [Semiconductors **34**, 606 (2000)].

Translated by T. Galkina

Doklady Physics, Vol. 47, No. 10, 2002, pp. 715–716. Translated from Doklady Akademii Nauk, Vol. 386, No. 5, 2002, pp. 612–613.

PHYSICS

Modeling the Effect of the Transconductance Increase in GaAs Field-Effect Transistors

V. A. Gergel', Corresponding Member of the RAS V. G. Mokerov, A. P. Zelenyĭ, and M. V. Timofeev

Received June 13, 2002

In [1], we formulated the concept of the possibility of substantial elevation of transconductance and operation speed of field-effect transistors. This concept can be realized through sectioning the transistor channel by low-resistance local inclusions that provide for the efficient cooling of electrons and the corresponding increase in their mobility and drift velocity. The quantitative estimates performed in [1] to reveal advantages of the structural modification of the transistor channel which had been proposed by us were based on a quasi-hydrodynamic (thermal) model [2] of the electron drift. This model was simplified by ignoring the contribution of the thermal relaxation and thermal current. Nevertheless, the model made it possible to demonstrate the basic features of the so-called overshoot effect [3].

The goal of the present study is a more rigorous substantiation of the concept for the super-speed electron drift in a profiled channel, which is being developed by us. In doing this, we exploited the complete stationary quasi-hydrodynamic electron-drift model, which was developed on the basis of the well-known PISCES-2ET software package. In due course, we even used this program package to study features of the avalanche breakdown of GaAs field-effect transistors [4]. The package was modified by introducing exact dependences of kinetic coefficients on the electron temperature, which were obtained by the Monte Carlo method [5].

Unfortunately, properties intrinsic to the given software package did not allow us to advance deeply into the nanometer-size region which we were interested in. We had to restrict our analysis to the corresponding numerical experiments with three submicron model structures. The first of them was a usual GaAs field-effect transistor with channel length $L = 0.6$ μm. In the second model structure, the channel was divided into two parts by a central quasi-drain highly doped region with a length of 0.2 μm. In the third structure, two intermediate quasi-drain regions were formed, whereas the channel itself was divided into three equal parts (Fig. 1). It is worth noting that for all three cases, the total length of active (high-resistance) channel parts was equal to the same value of 0.6 μm.

In Fig. 2, we present a typical distribution of the electron temperature along the channel length, which

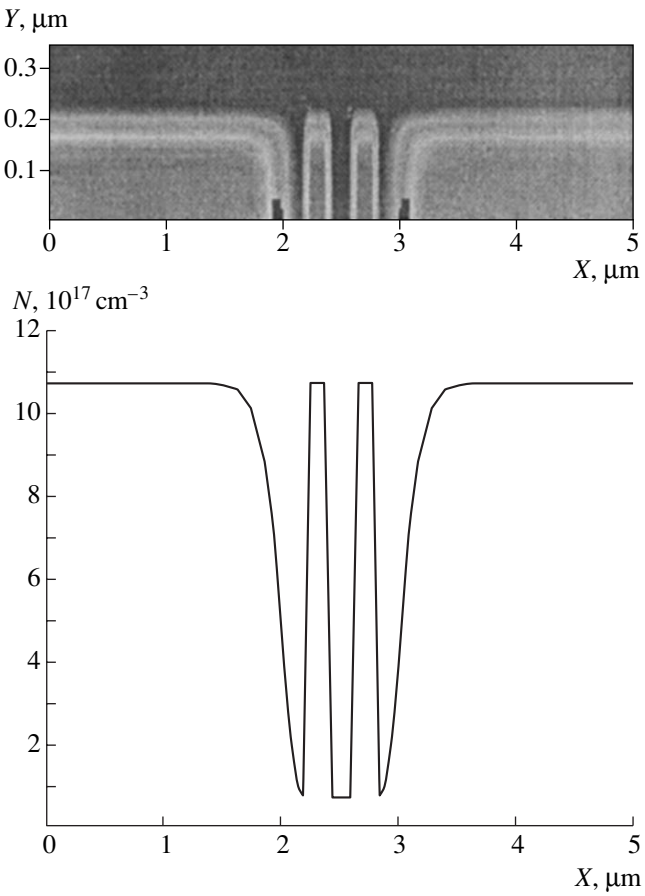

Fig. 1. Profile of the donor-admixture distribution in a field-effect transistor with the sectioned channel.

Institute of Radio Engineering and Electronics, Russian Academy of Sciences, Mokhovaya ul. 18, Moscow, 103907 Russia

1028-3358/02/4710-0715$22.00

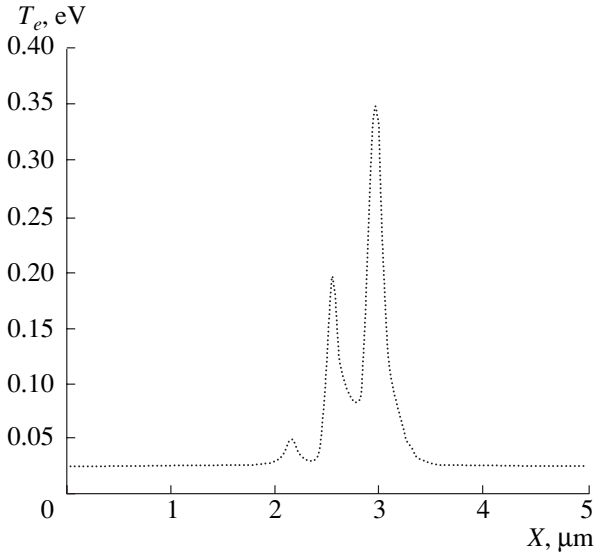

Fig. 2. Typical electron-temperature distribution in the sectioned structure of a field-effect transistor.

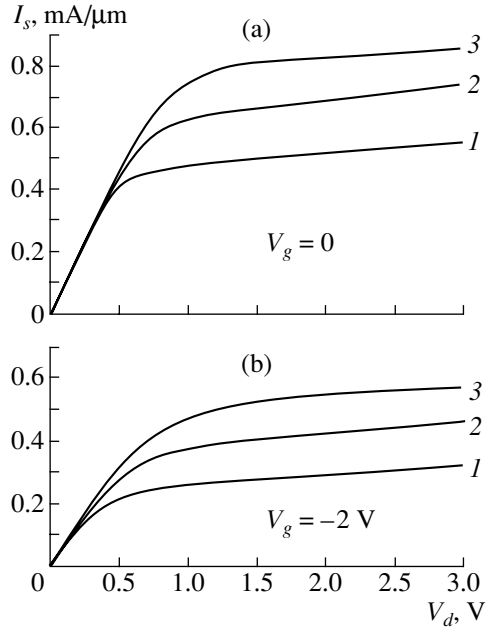

Fig. 3. Calculated current–voltage characteristics of a field-effect transistor with a sectioned channel in (a) open regime (the gate voltage $V_g = 0$) and (b) in the case of $V_g = -2$ V. Denotations *1*, *2*, and *3* correspond to the ordinal number of a high-resistance section.

was obtained in the course of numerical experiments. This distribution clearly demonstrates an effect of cooling of carriers in intermediate quasi-drains. Plots of Fig. 3 exhibit typical calculated current–voltage characteristics for all three modeled structures. These plots clearly show the expected tendency of an increase in currents and in the transconductance for the sectioned structures.

In conclusion, we emphasize that limitations inherent in the software package employed by us did not allow us to model situations we were interested in, namely, those with 10 or more nanometer-size inclusions. Nevertheless, the obtained results for submicron inclusions clearly and convincingly demonstrate a tendency to the improvement of device characteristics as a result of sectioning the channel of a field-effect transistor.

ACKNOWLEDGMENTS

The work was supported by the Russian Foundation for Basic Research, project no. 01-02-16360.

REFERENCES

1. V. A. Gergel' and V. G. Mokerov, Dokl. Akad. Nauk **375**, 609 (2000) [Dokl. Phys. **45**, 647 (2000)].
2. V. A. Gergel', V. G. Mokerov, M. V. Timofeev, and Yu. V. Fedorov, Fiz. Tekh. Poluprovodn. (St. Petersburg) **34**, 239 (2000) [Semiconductors **34**, 228 (2000)].
3. T. Enoki, S. Sugitani, and Y. Yamane, IEEE Trans. Electron Device **37**, 935 (1990).
4. V. A. Gergel' and G. Yu. Khrenov, *Abstracts of Reports, All-Russia Conference on Semiconductors-97* (Fiz. Inst. Akad. Nauk, Moscow, 1997), p. 137.
5. V. A. Nikolaeva, V. D. Pishchalko, V. I. Ryzhiĭ, and G. Yu. Khrenov, Mikroélektronika **17**, 504 (1988).

Translated by G. Merzon

Doklady Physics, Vol. 47, No. 10, 2002, pp. 717–720. Translated from Doklady Akademii Nauk, Vol. 386, No. 5, 2002, pp. 614–617.

PHYSICS

Simulation of the Properties of Periclase by Minimizing Atomization Energy

Corresponding Member of the RAS V. S. Urusov and I. Yu. Kantor

Received June 7, 2002

Periclase (MgO) has long been actively studied both theoretically and experimentally. A large body of data concerning the structure, properties, and features of the chemical bond of this oxide, which has a NaCl-type structure stable over a very wide range of temperatures and pressures, was accumulated. For this reason, periclase is often used to test new theories, experiments, and even as a standard for determining pressure in high-pressure investigations. In addition, most researchers admit that periclase is one of the primary components of the Earth's lower mantle. Thus, the properties of MgO at high temperatures and pressures are of great significance for interpretation of geophysical data on the structure of deep geospheres.

In this study, we simulate the properties of periclase in terms of the semiclassical atomistic method [1], where semiempirical potentials of interatomic interaction are used to calculate atomization energy and elastic and thermodynamic properties and to derive the equation of state for MgO in a wide range of pressures. The results are compared with measurements and theoretical data obtained by advanced simulation methods based on quantum-chemical calculations [2].

In terms of the semiclassical atomistic approach, atoms, which have definite size (radius) and carry certain effective charges, are bound by the Coulomb and short-range interatomic forces to an infinite three-dimensional periodic structure. The most stable and thermodynamically probable structure has the lowest structural energy E_{str}, which is determined as the sum of all interatomic interactions over all atomic pairs. Among the available software packages for minimizing the energy of this system, the package GULP1.3 for the LINUX operating system [3] has the widest capabilities and highest operation speed.

In the pure ionic model, which is completely applicable only to a narrow set of alkali-metal halides, the structural energy coincides in physical meaning with the energy of the ionic crystal lattice. The ionic model fails to reproduce the structure and properties of periclase in most cases. For example, the lattice constant and bulk modulus calculated in [4] much exceed the experimental values: a_{theor} = 2.178 Å, a_{exp} = 2.104 Å, K_{theor} = 234 GPa, and K_{exp} = 163 GPa. In fact, most oxide inorganic compounds and minerals have an intermediate type of bond rather than pure ionic or covalent chemical bond. In this case, ions have effective charge $q = fz$, where f is the bond ionicity ($0 \le f \le 1$) and z is the formal valence. In this case, the structural energy E_{str} cannot be directly associated with either the lattice energy or the atomization energy. The atomization energy is the sum of E_{str} and the energy ΔE of the charge transfer from a cation to an anion:

$$E_{at} = E_{str} + \Delta E. \quad (1)$$

The calculation of the charge-transfer energy ΔE is complicated primarily because, instead of using the subsequent ionization potentials of isolated atoms in their ground state, it is necessary to take into account the formation of a valence state and an effective (positive and negative) charge when an atom passes into the crystalline substance. For example, for Mg with the electron configuration $[1s^2 2s^2 2p^6]3s^2$, it is necessary to take into account the energy of the s–p valence-electron hybridization, which is not known with certainty. The simplest and most natural method is to take the average ionization energy for the 3s and 3p electrons instead of the first ionization potential. The method of calculation of the charge-transfer energy ΔE was detailed in [5]. For an oxygen atom O, the charge-transfer energy due to the attachment of a fraction of magnesium valence electrons is determined more precisely [5].

In the total-minimization method, the structural energy E_{str} is calculated for the whole range of the ionicity f from 0 to 1 (corresponding to effective charges q from 0 to $\pm 2e_0$) and, according to Eq. (1), is added to the corresponding charge-transfer energy ΔE.

The structural energy E_{str} is described by the expression

$$E_{str} = E_{el} + E_{sr}, \quad (2)$$

Moscow State University, Vorob'evy gory, Moscow, 119899 Russia

1028-3358/02/4710-0717$22.00

$$E_{el} = \sum \frac{q_i q_j}{r_{ij}},$$

$$E_{sr} = \sum_{Mg-O} V_B + \sum_{O-O} V_B + \sum_{Mg-O} V_M + \sum_{O-Mg-O} V_\theta,$$

$$V_B = A_{ij}\exp\left(\frac{-r_{ij}}{\rho_{ij}}\right) - \frac{C_{ij}}{r_{ij}^6},$$

$$V_M = D_{ij}\{[1 - \exp(-a_{ij}(r_{ij} - r_{ij0}))]^2 - 1\},$$

$$V_\theta = k(\theta - \theta_0)^2.$$

Here, E_{el} is the Coulomb electrostatic interaction, r_{ij} is the distance between atoms i and j, E_{sr} is the energy of the short-range potentials, the Buckingham potential V_B describes the repulsion between oppositely charged Mg and O ions and the van der Waals attraction, V_M is the Morse potential responsible for the covalent Mg–O bond, the three-particle angular O–Mg–O potential V_θ taking into account that the bond is partially oriented is necessary for reproducing the deviation from the Cauchy relationship for the elastic constants ($C_{12} = C_{44}$), θ is the O–Mg–O angle, and $\theta_0 = 90°$ is the equilibrium angle.

The parameters of interatomic potentials were found by fitting the calculated properties (lattice constant, bulk modulus, and elastic constants under normal conditions) to the corresponding experimental values and are presented below.

For the electrostatic interactions, $q = 1.84e_0$, the action range is 0–∞.

For the Buckingham potential between (i) Mg–O, $A = 224.18$ eV, $\rho = 0.463$ Å, $C = 0.0$, the action range is 0–8.0 Å; and (ii) O–O, $A = 22764.0$ eV, $\rho = 0.149$ Å, $C = 27.88$ eV Å^6, the action range is 0–8.0 Å.

For the Morse Mg–O potential, $D = 1.023$ eV, $a = 1.043$ Å^{-1}, $r_0 = 1.83$ Å, the action range is 0–8.0 Å.

For the three-particle O–Mg–O potential, $\theta_0 = 90°$, $k = 1.736$ eV, the action range is 0–3.2 Å.

When calculating the structural energy $E_{str}(f)$ as a function of f, it is necessary to introduce the corresponding weight function f^2 for the short-range Buckingham potential V_B and the weight function $1 - f^2$ for the Morse potential V_M and three-particle potential V_θ. After adding the corresponding values of $\Delta E(f)$ to $E_{str}(f)$, we find the atomization energy $E_{at}(f)$ as a function of the ionic character. The minimum of this function corresponds to the most stable state of a crystal for certain optimal effective charges, which cannot be found from experiment with sufficient accuracy, and the atomization energy E_{at} (Fig. 1). The effective charge for MgO turned out to be equal to $\pm 1.84e_0$, and the effective charge found from the quantum-chemical calculations [2] for various pressures in MgO ranges from ± 1.93 to $\pm 1.77e_0$. The energy E_{at} has a minimum value of –1035 kJ/mole, which is very close to the experimental atomization energy for MgO at 0 K (–1012 kJ/mol). Thus, minimizing the atomization energy makes it possible to find both the effective charges (or ionicity) and a crystal cohesive energy by using only the density and elastic properties of the crystal. This is a substantial advantage of the above approach.

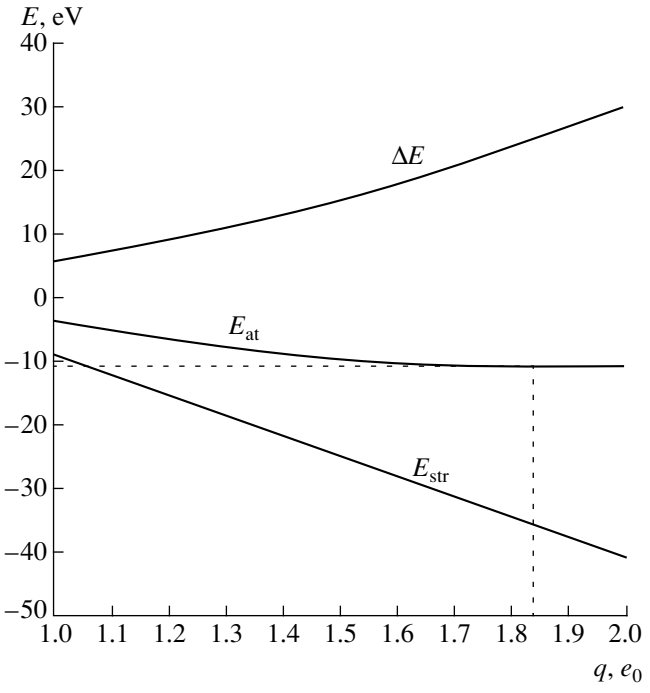

Fig. 1. Structural energy E_{str}, charge-transfer energy ΔE, and atomization energy E_{at} on the effective charge of ions. The dashed line shows the atomization-energy minimum corresponding to an effective charge of $\pm 1.84\ e_0$ and to the calculated atomization energy.

Using the above parameters of interatomic potentials, one can calculate certain basic properties of the crystal: the unit-cell volume, bulk modulus, and the matrix of the elastic constants among which only three constants C_{11}, C_{12}, and C_{44} are independent for a cubic crystal. Performing calculations for various pressures, we find the elastic properties of the crystal as functions of pressure. Figure 2 shows the bulk modulus and elastic constants calculated in this study, as well as the theoretical [2] and experimental [6–9] values of these quantities. The bulk modulus K calculated here is virtually in the middle of the range given by other studies. At the same time, the elastic constant C_{11} is systematically lower, whereas C_{44} is systematically higher than most other data. Furthermore, all the elastic properties calculated in this study depend almost linearly on pressure. This behavior agrees only with some of the reported data [2, 7]. The pressure dependence of the MgO molar volume is shown in Fig. 3 along with the published data. It is seen that all the data agree satisfac-

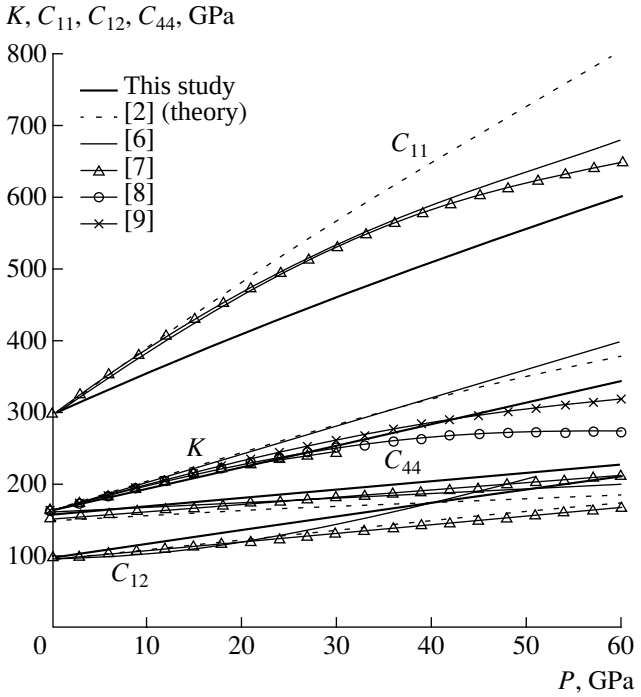

Fig. 2. Bulk modulus K and elastic constants C_{11}, C_{12}, and C_{44} vs. pressure.

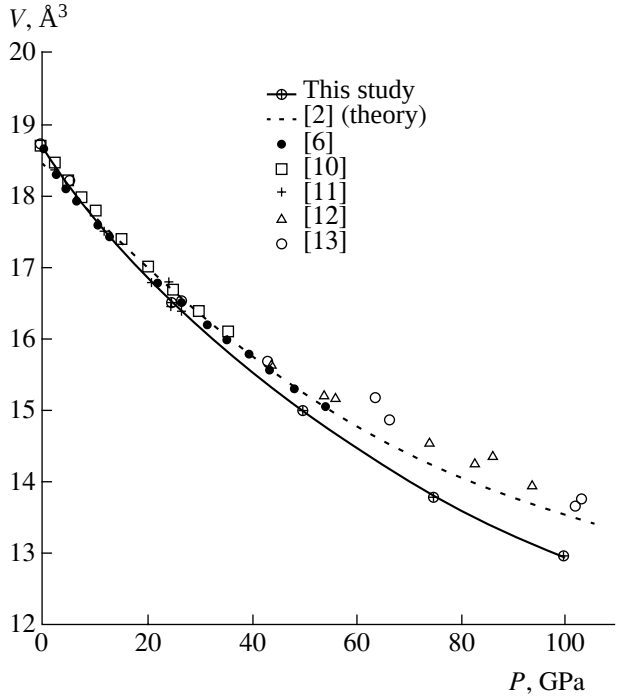

Fig. 3. P–V diagram for MgO.

torily up to pressures of about 40 GPa, whereas our results for higher pressures point to a noticeably higher compressibility of this crystal than follows from the most reliable experiments [6, 10–13].

Using molecular dynamics, one can find the unit-cell volume as a function of temperature and calculate the thermal-expansion coefficient α. The calculation of phonon properties makes it possible to find important thermodynamic quantities such as the entropy S and specific heat at constant volume C_V and their temperature dependences (Fig. 4). Although the specific heat found here differs significantly from the experimental value for normal conditions, the corresponding function $C_V(T)$ is quite close both to the experimental and theoretical curves at higher temperatures. However, entropy is systematically lower than the standard experiment data [14] and is somewhat closer to the theoretical *ab initio* calculations [2].

The table presents the fundamental physical properties both calculated and measured for the crystal. As is seen, the calculated thermal-expansion coefficient, specific heat, and entropy differ considerably from the respective experimental data. Furthermore, the elastic constants and volume differ substantially from the experimental values at high pressures. This means that the semiclassical atomistic calculations with fixed

Calculated and experimental properties of periclase

Property	Calculation	Experiment
Lattice constant a, Å (0 K)	4.203	4.199
a, Å (300 K)	4.213	4.211
Bulk modulus K, GPa	163.06	162.5
Elastic constants, GPa: C_{11}	297.08	297.0
C_{12}	96.05	95.3
C_{44}	156.00	155.7
Thermal-expansion coefficient α, K^{-1} (300 K)	2.11×10^{-5}	3.12×10^{-5}
Specific heat C_V, J mol^{-1} K^{-1} (300 K)	33.37	37.67
Entropy S, J mol^{-1} K^{-1} (300 K)	23.04	26.9
Atomization energy E_{at}, kJ mol^{-1} (0 K)	–1035	–1012

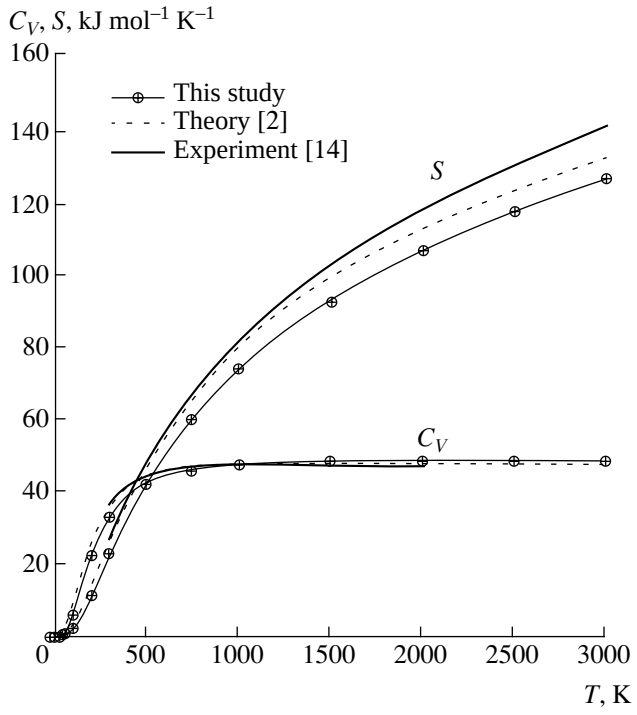

Fig. 4. Temperature dependence of the heat capacity C_V and entropy S.

effective charges of atoms cannot be sufficiently accurate, because there are strong reasons to believe that the degree of covalency of the chemical bond increases considerably with pressure, as was shown, for example, in [2]. The inclusion of this effect can likely improve the simulation results, but computer-time expenditure increases substantially in this case.

REFERENCES

1. V. S. Urusov and L. S. Dubrovinskiĭ, *Computer Simulation of the Structure and Properties of Minerals* (Mosk. Gos. Univ., Moscow, 1989).
2. B. B. Karki, R. M. Wentzcovitch, S. de Gironcoli, and S. Baroni, Phys. Rev. B **61**, 8793 (2000).
3. J. D. Gale, *GULP User's Manual* (London Royal Institution and Imperial College, London, 1992).
4. W. C. Mackrodt and R. S. Steward, J. Phys. C **12**, 5015 (1979).
5. V. S. Urusov and N. N. Eremin, Phys. Chem. Miner. **25**, 374 (1997).
6. C.-S. Zha, H. K. Mao, and R. J. Hemley, Proc. Natl. Acad. Sci. USA **97**, 13494 (2000).
7. S. V. Sinogeikin and J. D. Bass, Phys. Rev. B **59**, 14141 (1999).
8. A. Chopelas, Earth Planet. Sci. Lett. **114**, 185 (1992).
9. B. B. Karki, L. Strixrude, S. J. Clark, *et al.*, Am. Mineral. **82**, 51 (1997).
10. E. A. Perez-Albuerne and H. G. Drickamer, J. Chem. Phys. **43**, 1381 (1965).
11. J. S. Weaver, T. Takahashi, and W. A. Basset, *Accurate Characterization of the High Pressure Environment* (National Bureau of Standards, Washington, DC, 1971).
12. H. K. Mao and P. M. Bell, J. Geophys. Res. **84**, 4533 (1979).
13. T. H. Duffy, R. J. Hemley, and H. K. Mao, Phys. Rev. Lett. **74**, 1371 (1995).
14. *Thermal Constants of Materials, Handbook*, Ed. by V. P. Glushko (VINITI, Moscow, 1965–1981), Nos. 1–10.

Translated by V. Bukhanov

Doklady Physics, Vol. 47, No. 10, 2002, pp. 721–724. Translated from Doklady Akademii Nauk, Vol. 386, No. 6, 2002, pp. 749–752.

PHYSICS

Dispersion Equations for the Directional Modes of a Gradient Elliptic Waveguide

V. I. Krivenkov

Presented by Academician E.M. Dianov March 15, 2002

Received March 18, 2002

To create wideband systems of coherent optical communication and many other optical-fiber devices, e.g., optical-fiber interferometers, it is necessary to have waveguides conserving the polarization of radiation passing through them. One type of such waveguides are single-mode elliptic waveguides, which, with the appropriately chosen refractive-index profile, can ensure the single-polarization mode [1] and have quite high dispersion characteristics [2, 3].

In this paper, the problem of the natural waves of a gradient elliptic waveguide with an arbitrary refractive-index profile is rigorously solved. For all directional modes of this waveguide, the exact expressions for field components, dispersion equations, and equations for critical wavelengths are obtained. Dispersion equations and equations for critical wavelengths are derived from the condition that a determinant whose order is virtually independent of the refractive-index profile of the waveguide is equal to zero.

Let us treat a gradient elliptic waveguide as a dielectric structure (light guide) homogeneous along a certain axis, which is taken as the z axis. This structure consists of (i) a core whose dielectric constant is stepwise continuous in the ξ coordinate in the elliptic-cylinder coordinate system ξ, η, z and (ii) an infinitely thick shell with constant permittivity.

In the general case, the permittivity of this waveguide has the form [4]

$$\varepsilon(\xi) = \begin{cases} \sum_{k=0}^{\infty} \varepsilon_{lk}\left(\frac{\xi - \xi_{l-1}}{\xi_l - \xi_{l-1}}\right)^k \\ \xi_{l-1} \le \xi < \xi_l,\ l = 1, 2, \ldots, N \\ \varepsilon_{00},\ \xi_N \le \xi < \infty, \end{cases}$$

where $\varepsilon_{00} < \max\varepsilon(\xi)$ (otherwise, all modes of this light guide are outflowing), $\xi_0 = 0$, and $\xi_1, \xi_2, \ldots, \xi_{N-1}$ are singular points of the permittivity of the waveguide core.

All components of the electric $\mathbf{E} = (E_\xi, E_\eta, E_z)$ and magnetic $\mathbf{H} = (H_\xi, H_\eta, H_z)$ fields of a directional mode of the waveguide depend on time t and longitudinal coordinate z as $\exp[j(\omega t - \beta z)]$, where ω and β are the circular frequency and constant of the longitudinal propagation of the mode, respectively. In what follows, this dependence will be omitted.

Let us consider the vectors

$$\mathbf{e} = \sqrt{\varepsilon_0}\begin{pmatrix} E_z \\ jG(\xi, \eta)E_\eta \end{pmatrix},$$

$$\mathbf{h} = \sqrt{\mu_0}\begin{pmatrix} H_z \\ jG(\xi, \eta)H_\eta \end{pmatrix},$$

where

$$G(\xi, \eta) = k_0\rho\sqrt{\sinh^2\xi + \sin^2\eta},\ k_0 = w\sqrt{\varepsilon_0\mu_0},$$

ε_0 and μ_0 are the electric and magnetic constants, respectively; and ρ is half the distance between the foci of the elliptic-cylinder coordinate system, in the form

$$\mathbf{e}(\xi, \eta) = \sum_{k=0}^{\infty} \mathbf{S}^{\mu}_{2k+\nu}(\xi, \eta)\mathbf{e}_k(\xi),$$

$$\mathbf{h}(\xi, \eta) = \sum_{k=0}^{\infty} \mathbf{S}^{1-\mu}_{2k+\nu}(\xi, \eta)\mathbf{h}_k(\xi),$$

$$\mu, \nu \in \{0, 1\}.$$

Here,

$$\mathbf{S}^{\alpha}_m(\xi, \eta) = \begin{pmatrix} sc^{\alpha}_m(\eta, q(\xi)) & 0 \\ 0 & sc^{1-\alpha}_m(\eta, q(\xi)) \end{pmatrix},$$

$$\alpha = 0, 1,$$

Moscow State Academy of Instrument Engineering and Informatics, ul. Stromynka 20, Moscow, 107846 Russia

1028-3358/02/4710-0721$22.00

$$q(\xi) = \begin{cases} q_1 & \text{for } 0 \le \xi < \xi_1 \\ q_2 & \text{for } \xi_1 \le \xi < \xi_2 \\ \dots & \\ q_{N+1} & \text{for } \xi_N \le \xi < \infty \end{cases}$$

$$q_l = -\frac{k_0^2 \rho^2 u_l^2}{4}, \quad u_l^2 = \gamma^2 - \varepsilon_{l0},$$

$$l = 1, 2, \dots, N+1, \quad \gamma = \frac{\beta}{k_0}$$

$$(\varepsilon_{N+1,0} = \varepsilon_{00}, u_{N+1}^2 > 0),$$

$$sc_{2m+\nu}^0(\eta, q) \equiv se_{2m+2-\nu}(\eta, q),$$

$$sc_m^1(\eta, q) \equiv ce_m(\eta, q), \quad m = 0, 1, \dots,$$

$se_m(\eta, q)$, $ce_m(\eta, q)$ are the angular Mathieu functions [5]. This form corresponds to even modes ${}_e\mathrm{HE}_{mn}$ and ${}_e\mathrm{EH}_{mn}$ for $\mu = 0$ and to odd modes ${}_o\mathrm{HE}_{mn}$ and ${}_o\mathrm{EH}_{mn}$ for $\mu = 1$, where the azimuthal index m is odd and even for $\nu = 0$ and 1, respectively.

Excluding the components E_ξ and H_ξ from Maxwell's equations for a nonmagnetic dielectric medium, we arrive at the set of equations

$$\varepsilon(\xi)\frac{d\mathbf{e}_m}{d\xi} = \sum_{n=0}^{\infty} \mathbf{A}_{2m+\nu, 2n+\nu}^{1-\mu}(\xi)\mathbf{h}_n,$$

$$\frac{d\boldsymbol{h}_m}{d\xi} = -\sum_{n=0}^{\infty} \mathbf{A}_{2m+\nu, 2n+\nu}^{\mu}(\xi)\mathbf{e}_n,$$

$$m = 0, 1, \dots \quad (\mu, \nu \in \{0, 1\}),$$

where

$$\mathbf{A}_{mn}^{\alpha}(\xi) = \begin{pmatrix} -\gamma f_{mn}^{\alpha 1}(q(\xi), q(\xi)) & -\delta_{mn}(\gamma^2 - \varepsilon(\xi)) \\ G_{mn}^{\alpha}(\xi) + 2q(\xi)g_{mn}^{\alpha}(q(\xi)) - \delta_{mn}\lambda_n^{\alpha}(q(\xi)) & \gamma f_{mn}^{1-\alpha, 1}(q(\xi), q(\xi)) \end{pmatrix},$$

$$G_{mn}^{\alpha}(\xi) = \frac{\varepsilon(\xi)k_0^2\rho^2}{2}[\delta_{mn}\cosh^2\xi - g_{mn}^{\alpha}(q(\xi))], \quad \delta_{mn} = \begin{cases} 1 & \text{for } m = n \\ 0 & \text{for } m \ne n, \end{cases}$$

$$g_{mn}^{\alpha}(q) = \frac{1}{\pi}\int_0^{2\pi} \cos 2\eta\, sc_m^{\alpha}(\eta, q) sc_m^{\alpha}(\eta, q) d\eta,$$

$$f_{mn}^{\alpha j}(q, q') = \frac{1}{\pi}\int_0^{2\pi} sc_m^{|j-\alpha|}(\eta, q')\frac{d^j}{d\eta^j}[sc_n^{\alpha}(\eta, q)]d\eta, \quad j = 0, 1, \ \alpha = 0, 1,$$

$\lambda_n^{\alpha}(q_l)$ are eigenvalues for the functions $sc_n^{\alpha}(\eta, q_l)$, $l = 1, 2, \dots, N+1$.

The continuous solution of this set of equations, which satisfies the familiar boundary conditions at $\xi = 0$ and $\xi \longrightarrow \infty$, is represented as

$$\begin{pmatrix} \mathbf{e}_m(\xi) \\ \dots \\ \mathbf{h}_m(\xi) \end{pmatrix} = \sum_{n=0}^{\infty} \begin{cases} \sum_{k=0}^{\infty} \left(a_n \begin{pmatrix} \mathbf{e}_{mnk}^{0l} \\ \dots \\ \mathbf{h}_{mnk}^{0l} \end{pmatrix} + b_n \begin{pmatrix} \mathbf{e}_{mnk}^{1l} \\ \dots \\ \mathbf{h}_{mnk}^{1l} \end{pmatrix} \right) \left(\frac{\xi - \xi_{l-1}}{\xi_l - \xi_{l-1}} \right)^k, & \text{for } \xi_{l-1} \le \xi < \xi_l, \ l = 1, 2, \dots, N \\ \left(c_n \begin{pmatrix} \mathbf{e}_{mn}^{\mu}(\xi) \\ \dots \\ -\varepsilon_{00}\mathbf{h}_{mn}^{\mu}(\xi) \end{pmatrix} + d_n \begin{pmatrix} \mathbf{h}_{mn}^{1-\mu}(\xi) \\ \dots \\ \mathbf{e}_{mn}^{1-\mu}(\xi) \end{pmatrix} \right), & \text{for } \xi_N \le \xi < \infty, \ m = 0, 1, \dots, \end{cases}$$

where

$$\mathbf{e}^{\alpha 1}_{mn0} = \mu\delta_{mn}\begin{pmatrix}\alpha\\ 1-\alpha\end{pmatrix},$$

$$\mathbf{h}^{\alpha 1}_{mn0} = (1-\mu)\delta_{mn}\begin{pmatrix}\alpha\\ 1-\alpha\end{pmatrix},$$

$$\mathbf{e}^{\alpha, l+1}_{mn0} = \sum_{j=0}^{\infty}\sum_{k=0}^{\infty}\mathbf{F}^{\mu l}_{2m+\nu, 2j+\nu}\mathbf{e}^{\alpha l}_{jnk},$$

$$\mathbf{h}^{\alpha, l+1}_{mn0} = \sum_{j=0}^{\infty}\sum_{k=0}^{\infty}\mathbf{F}^{1-\mu, l}_{2m+\nu, 2j+\nu}\mathbf{h}^{\alpha l}_{jnk},\quad l = 1, 2, \ldots, N,$$

$$\mathbf{e}^{\alpha l}_{m,n,k+1} = -\frac{1}{\varepsilon_{l0}(k+1)}$$

$$\times\sum_{j=0}^{k}\left(j\varepsilon_{l,k-j+1}\mathbf{e}^{\alpha l}_{mnj} - \sum_{i=0}^{\infty}\mathbf{A}^{1-\mu, l}_{2m+\nu, 2i+\nu, k-j}\mathbf{h}^{\alpha l}_{inj}\right),$$

$$\mathbf{h}^{\alpha l}_{m,n,k+1} = -\frac{1}{k+1}\sum_{j=0}^{k}\sum_{i=0}^{\infty}\mathbf{A}^{\mu l}_{2m+\nu, 2i+\nu, k-j}\mathbf{e}^{\alpha l}_{inj}),$$

$$k = 0, 1, \ldots,$$

$$\mathbf{F}^{\alpha l}_{mn} = \begin{pmatrix} f^{\alpha 0}_{mn}(q_l, q_{l+1}) & 0\\ 0 & f^{1-\alpha, 0}_{mn}(q_l, q_{l+1})\end{pmatrix},$$

$$\mathbf{A}^{\alpha l}_{mnk} = \begin{pmatrix} -\gamma f^{\alpha 1}_{mn}(q_l, q_l)\delta_{0k} & -\delta_{mn}(\delta_{0k}\gamma^2 - \varepsilon_{lk})\\ G^{\alpha l}_{mnk} + \delta_{0k}(2q_l g^{\alpha}_{mn}(q_l) - \delta_{mn}\lambda^{\alpha}_{n}(q_l)) & \gamma f^{1-\alpha, 1}_{mn}(q_l, q_l)\delta_{0k}\end{pmatrix},$$

$$G^{\alpha l}_{mnk} = \frac{k_0^2\rho^2}{2}\left\{\delta_{mn}\sum_{i=0}^{k}\frac{[1+(-1)^i]^i}{i!}\varepsilon_{l,k-i} - \varepsilon_{lk}g^{\alpha}_{mn}(q_l)\right\},$$

$$\mathbf{e}^{\alpha}_{mn}(\xi) = \begin{pmatrix}\delta_{mn}\\ -f^{\alpha}_{2m+\nu, 2n+\nu}\end{pmatrix},$$

$$\mathbf{h}^{\alpha}_{mn}(\xi) = \begin{pmatrix}0\\ \delta_{mn}K^{\alpha}_{2n+\nu}(\xi)\end{pmatrix},$$

$$f^{\alpha}_{mn} = \frac{\gamma}{u^2_{N+1}}f^{\alpha 1}_{mn}(q_{N+1}, q_{N+1}),$$

$$K^{\alpha}_{n}(\xi) = \frac{\dfrac{d}{d\xi}[M^{(3)}_{\alpha n}(\xi, q_{N+1})]}{u^2_{N+1}M^{(3)}_{\alpha n}(\xi_N, q_{N+1})},$$

$$\alpha = 0, 1,\ \mu, \nu \in \{0, 1\},$$

$$M^{(3)}_{0, 2m+\nu}(\xi, q) \equiv Ms^{(3)}_{2m+2-\nu}(\xi, q),$$

$$M^{(3)}_{1m}(\xi, q) \equiv Mc^{(3)}_{m}(\xi, q),\ m = 0, 1, \ldots,$$

$Ms^{(3)}_m(\xi, q)$ and $Mc^{(3)}_m(\xi, q)$ are the radial Mathieu functions of the third kind [5], and constants a_n, b_n, c_n, and d_n, $n = 0, 1, \ldots$ present the nontrivial solution of the homogeneous linear set of equations

$$\sum_{n=0}^{\infty}\left(a_n\begin{pmatrix}\mathbf{e}^{0, N+1}_{mn0}\\ \ldots\ldots\\ \mathbf{h}^{0, N+1}_{mn0}\end{pmatrix} + b_n\begin{pmatrix}\mathbf{e}^{1, N+1}_{mn0}\\ \ldots\ldots\\ \mathbf{h}^{1, N+1}_{mn0}\end{pmatrix}\right)$$

$$= \sum_{n=0}^{\infty}\left(c_n\begin{pmatrix}\mathbf{e}^{\mu}_{mn}(\xi_N)\\ \ldots\ldots\ldots\\ -\varepsilon_{00}\mathbf{h}^{\mu}_{mn}(\xi_N)\end{pmatrix} + d_n\begin{pmatrix}\mathbf{h}^{1-\mu}_{mn}(\xi_N)\\ \ldots\ldots\ldots\\ \mathbf{e}^{1-\mu}_{mn}(\xi_N)\end{pmatrix}\right),$$

$$m = 0, 1, \ldots,$$

whose determinant must be equal to zero.

Excluding unknowns c_n and d_n, $n = 0, 1, \ldots$ from the last set of equations and equating the determinant of the resulting set of equations to zero, we obtain the following dispersion equation for directional modes of the gradient elliptic light guide:

$$\det(\mathbf{P}^{\mu\nu}\mathbf{Q}^{\mu\nu}) = 0,\ \mu, \nu \in \{0, 1\},$$

where

$$\mathbf{Q}^{\mu\nu} = (\mathbf{Q}^{\mu\nu}_{mn}),\ m, n = 0, 1, \ldots,$$

$$\mathbf{Q}^{\mu\nu}_{mn} = \left(\begin{array}{c:c}\mathbf{e}^{0, N+1}_{mn0} & \mathbf{e}^{1, N+1}_{mn0}\\ \hdashline \mathbf{h}^{0, N+1}_{mn0} & \mathbf{h}^{1, N+1}_{mn0}\end{array}\right),$$

$$\mathbf{P}^{\mu\nu} = (\mathbf{P}^{\mu\nu}_{mn}),\ m, n = 0, 1, \ldots,$$

$$\mathbf{P}^{\mu\nu}_{mn} = \begin{pmatrix} f^{\mu}_{2m+\nu,\,2n+\nu} & \delta_{mn} - \delta_{mn}K^{1-\mu}_{2n+\nu}(\xi_N) & 0 \\ \delta_{mn}\varepsilon_{00}K^{\mu}_{2n+\nu}(\xi_N) & 0 & f^{1-\mu}_{2m+\nu,\,2n+\nu} \quad \delta_{mn} \end{pmatrix}.$$

This equation corresponds to even modes ${}_e\mathrm{HE}_{mn}$ and ${}_e\mathrm{EH}_{mn}$ for $\mu = 0$ and to odd modes ${}_o\mathrm{HE}_{mn}$ and ${}_o\mathrm{EH}_{mn}$ for $\mu = 1$, where the azimuthal index $m = 2k + \nu$, $k = 0, 1, \ldots$.

For given wavelength $\lambda = \dfrac{2\pi}{k_0}$, the dispersion equation is an equation for unknown phase constant γ, which can take values $\gamma > \sqrt{\varepsilon_{00}}$. For the limiting case $\gamma = \sqrt{\varepsilon_{00}}$, we have the following equation for unknown wavelength λ:

$$\det(\mathbf{R}^{\mu\nu}(\mathbf{Q}^{\mu\nu})_{\gamma = \sqrt{\varepsilon_{00}}}) = 0, \quad \mu, \nu \in \{0, 1\},$$

where

$$\mathbf{R}^{\mu\nu} = (\mathbf{R}^{\mu\nu}_{mn}), \quad m, n = 0, 1, \ldots,$$

$$\mathbf{R}^{\mu 0}_{0n} = \delta_{0n}(\mu, 0, 1-\mu, 0),$$

$$\mathbf{R}^{\mu 1}_{0n} = \delta_{0n}\begin{pmatrix} 1 & 0 & 0 & 0 \\ 0 & 0 & 1 & 0 \end{pmatrix}, \quad n = 0, 1, \ldots,$$

$$\mathbf{R}^{\mu 0}_{m,\,m-\mu} = \mathbf{D}_{2m},$$

$$\mathbf{R}^{\mu 0}_{m,\,m-\mu\pm 1} = \frac{[1 \mp (-1)^{\mu}]}{2}\mathbf{I}^{\mu} + \mathbf{T}_{2m,\pm 1},$$

$$\mathbf{R}^{\mu 1}_{mm} = \mathbf{I}^{\mu} + \mathbf{D}_{2m+1}, \quad \mathbf{R}^{\mu 1}_{m,\,m-\mu\pm 1} = \mathbf{T}_{2m+1,\pm 1},$$
$$m = 1, 2, \ldots, \quad m - \mu \pm 1 \geq 0,$$

$$\mathbf{R}^{\mu\nu}_{mn} = [0], \quad n \neq m, \quad n \neq m \pm 1,$$
$$m = 1, 2, \ldots, \quad n = 0, 1, \ldots,$$

$$\mathbf{I}^{\mu} = (-1)^{\mu}\sqrt{\varepsilon_{00}}\begin{pmatrix} 1 & 0 & 0 & 0 \\ 0 & 0 & 0 & 1 \end{pmatrix},$$

$$\mathbf{D}_n = \begin{pmatrix} 0 & 0 & 1 & 0 \\ 0 & \varepsilon_{00} & -s_n & 0 \end{pmatrix},$$

$$T_{nk} = k\frac{\varepsilon_{00}k_0^2\rho^2(n+2k)}{8(n+k)}\begin{pmatrix} 0 & 0 & 0 & 0 \\ 0 & 0 & 1 & 0 \end{pmatrix}, \quad k = \pm 1,$$

$$s_n = n - \frac{\varepsilon_{00}k_0^2\rho^2}{4}\left[\frac{\exp(2\xi_N)}{n-1} + \frac{\exp(-2\xi_N)(2n+1)}{n+1}\right],$$
$$n = 2, 3, \ldots,$$

and [0] is the zero 2×4 matrix. This equation is an equation for the critical wavelengths of even and odd directional modes for $\mu = 0$ and 1, respectively, where the azimuthal index is even and odd for $\nu = 0$ and 1, respectively.

The order of the determinant in the left-hand side of the above equations is equal to double the number of terms in the decomposition of the field components of the mode in terms of the angular Mathieu functions and is virtually independent of the refractive index profile of the waveguide in question.

REFERENCES

1. A. S. Belanov, E. M. Dianov, and V. I. Krivenkov, Kvantovaya Élektron. (Moscow) **11**, 1273 (1984).
2. S. R. Rengarajan and J. E. Lewis, Radio Sci. **16** (4), 541 (1981).
3. A. S. Belanov and V. I. Krivenkov, Sov. Lightwave Commun. **1** (2), 139 (1991).
4. V. I. Krivenkov, Dokl. Akad. Nauk **378** (6), 751 (2001) [Dokl. Phys. **46**, 407 (2001)].
5. *Handbook of Mathematical Functions*, Ed. by M. Abramowits and I. Stegun (Dover, New York, 1971; Nauka, Moscow, 1979).

Translated by R. Tyapaev

Doklady Physics, Vol. 47, No. 10, 2002, pp. 725–727. Translated from Doklady Akademii Nauk, Vol. 386, No. 6, 2002, pp. 753–755.

PHYSICS

The Lack of the Stabilization of Quasi-Stationary Electron States in a Strong Magnetic Field

V. N. Rodionov, G. A. Kravtsova, and A. M. Mandel'

Presented by Academician V.G. Kadyshevskiĭ May 24, 2002

Received June 7, 2002

1. Studies of ionization of atoms and ions, as well as of photoabsorption processes in crystals in intense electromagnetic fields, began more than 35 years ago [1–3]. However, up to now, complete understanding of a number of questions having a vital importance for both atomic physics and solid-state physics is absent. This statement is valid, e.g., for investigations of nonlinear phenomena in strong electromagnetic fields of complicated configurations, which again have attracted the attention of researchers in recent years [4–7]. In particular, the possibility of retarded decays of unstable atomic nuclei with increasing field intensity (the so-called stabilization regime) was studied. However, independently of the type of electromagnetic-field configurations being applied, only the case of scalar charged particles was analyzed. This constraint made it impossible to reveal physically interesting polarization regularities arising in a strong magnetic field. We have managed to clarify the problem on the possibility of stabilizing decays of bound states of spinor and scalar particles in high-intensity magnetic fields. The results obtained require a fresh examination of the accepted concept that the growth of a magnetic field reduces the width of atomic energy levels and thereby stabilizes an atom and suppresses its ionization by an electric field.

2. We consider a process of ejecting charged particles from a potential well of short-range forces by a constant electric field F in the presence of a normal (with respect to the electric field) constant magnetic field H, with field intensities being assumed to be not low. To do this, we exploit the model of the three-dimensional delta-potential, which is applicable to many realistic physical systems, including atoms and ions [1–4]. We now analyze the decay process of quasi-stationary states for particles with spins $s = 0$ and $\frac{1}{2}$ under the action of external fields. Using the method of exact solutions [8] and performing standard calculations for the probability of the process per unit time, we arrive at the expression

$$W_q = \frac{\exp\left(-i\frac{3}{4}\pi\right)}{\sqrt{\pi}}\frac{eHE_0^{1/2}}{m^{3/2}} \times \int_{-\infty}^{\infty}\frac{d\rho}{(\rho - i\cdot 0)^{1/2}} f_q(\nu)\exp(iS). \quad (1)$$

Below, the system of units with $\hbar = c = 1$ is used; e and m are the electron charge and mass; and E_0 is the particle coupling energy in the short-range potential, which is unperturbed by the external field. The subscript $q = 1, 2$, which corresponds to the functions $f_1(\nu) = (\sin\nu)^{-1}$ and $f_2(\nu) = \cot\nu$ for scalar and spinor particles, respectively (after summation over polarization states). Poles in expression (1) are bypassed from below, and

$$S = \rho\left(-\frac{E_0}{m} + \frac{F^2}{2H^2}\right) - \frac{m^2F^2}{eH^3}\tan\frac{\nu}{2}, \quad \nu = \frac{\rho eH}{m^2}.$$

The integral entering into (1) can be calculated analytically by expanding $\exp\left(ia\tan\frac{\nu}{2}\right)$ into the Laguerre polynomials [9]. However, it is more convenient to use a simpler and physically more justified approximation based on the fact that the basic contribution to (1) occurs from the vicinity of the zero point. Thus, employing the calculation method thoroughly described in [10] and passing to normalized field intensities and coupling energies inherent in atomic physics,

$$F_a = m^2e^5, \quad H_a = m^2e^3c, \quad E_0 = \frac{k^2me^4}{2}$$

(in ordinary units, $F_a = 5.14 \times 10^9$ V cm^{-1} and $H_a = 2.35 \times 10^9$ G and the dimensionless parameter k characterizes different energy states of an atom and negative

Moscow State University of Geological Exploration, ul. Miklukho-Maklaya 23, Moscow, 118873 Russia

1028-3358/02/4710-0725$22.00

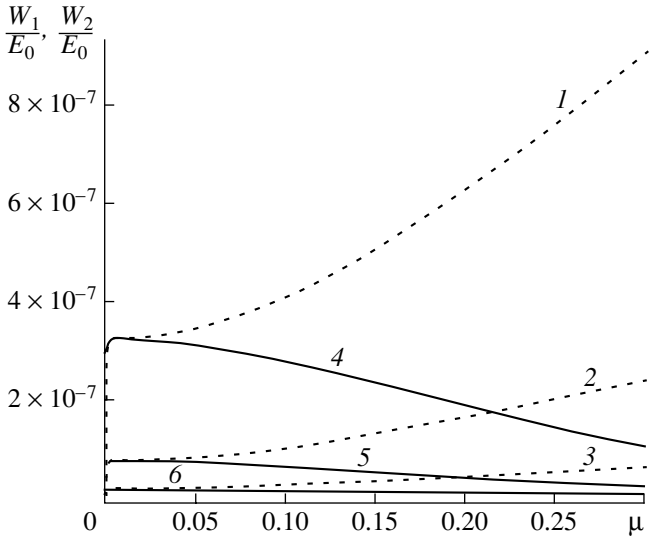

Normalized probabilities for the ejection from a short-range potential of scalar $\frac{W_1}{E_0}$ and spinor $\frac{W_2}{E_0}$ particles at fixed values of the electric field as a function of the magnetic field intensity.

ions), we find that the probability of the ejection from the potential well of a spinless particle and a particle with a spin is described, respectively, by the expressions

$$W_1 = \frac{4E_0}{\pi}\frac{\mu}{\varepsilon^{1/3}}\sum_{n=0}^{\infty}\mathrm{Ai}^2(y_n), \tag{2}$$

$$W_2 = \frac{4E_0}{\pi}\frac{\mu}{\varepsilon^{1/3}}\left[\frac{1}{2}\mathrm{Ai}^2(z_0) + \sum_{n=1}^{\infty}\mathrm{Ai}^2(z_n)\right]. \tag{3}$$

Here, Ai(x) are the Airy functions regular at infinity [8] whose arguments equal

$$y_n = \frac{1 + \mu/2 + n\mu}{\varepsilon^{2/3}}; \quad z_n = \frac{1 + n\mu}{\varepsilon^{2/3}}$$

and are determined by dimensionless external-field intensities

$$\varepsilon = \frac{2F}{k^3F_a}, \quad \mu = \frac{2H}{k^2H_a}.$$

3. We now discuss the results obtained. As is seen from relationships (2) and (3), the ejection probabilities at a constant coupling energy are determined by only the two parameters ε and μ. We emphasize that the argument z_0 of the Airy function in the first term of expression (3) is independent of μ. In expression (2), there are no such terms, a fact which acquires a fundamental significance in the case of a strong magnetic field.

Plots of the normalized particle-ejection probabilities by an electric field as a function of the intensity μ of the magnetic field, which are calculated by formulas (2) and (3) for a fixed coupling energy corresponding to a negative helium ion He($2p$) with $k = 0.075$, are presented in the figure. Solid and dashed lines correspond to scalar and spinor particles, respectively. In this cases, curves *1* and *4*, *2* and *5*, and *3* and *6* relate to the electric-field intensity $\varepsilon_1 = 0.11$, 0.1, and 0.09, respectively. In usual units, the intensities turn out to be on the order of 10^5 V cm^{-1}.

It is easy to see that in weak fields, the dependences of the ejection probabilities on the intensity μ of an external magnetic field in the case of scalar and spinor particles differ rather negligibly. Indeed, in the case of $\varepsilon \ll 1$ and $\mu < \varepsilon$, we can derive from formulas (2), (3) for spinless and spinor particles

$$\left.\begin{matrix} W_1 \\ W_2 \end{matrix}\right\} = \frac{E_0}{2}(\varepsilon \mp g_{1,2})\exp\left(-\frac{4}{3\varepsilon}\right), \tag{4}$$

where $g_1 = \frac{\mu^2}{6\varepsilon}$ and $g_2 = 2g_1$.

Relationship (4) is quite expected: the ionization probability in a weak electromagnetic field is exponentially suppressed and for $\mu = 0$ transforms to the known Demkov–Drukarev expression for a pure electric field [11]. In the limiting case $\mu \ll \varepsilon$, corrections to the probability given in [11] are quadratic over the magnetic field and their signs for W_1 and W_2 are different. It is worth noting that in this approximation, the relationship for W_1 is also consistent with the corresponding results of [12].

As follows from the same figure, for a spinless particle in a strong magnetic field, the decay probability as a function of an external magnetic field decreases with an increase in μ. In contrast, for particles with the spin $\frac{1}{2}$, in the case of $\mu > \varepsilon$, we observe a practically linear rise of W_2 with the magnetic-field intensity. The analytical estimate of expression (2) at $\mu \gg \varepsilon^{2/3}$, $\varepsilon \ll 1$ yields

$$W_1 = \mu\left(1 + \frac{\mu}{2}\right)^{-1/2}E_0\exp\left[-\frac{4(1 + \mu/2)^{3/2}}{3\varepsilon}\right]. \tag{5}$$

In the same limit, it follows from formula (3) that

$$W_2 = \frac{\mu E_0}{2}\exp\left(-\frac{4}{3\varepsilon}\right). \tag{6}$$

Thus, the results obtained testify to the fact that the stabilizing role of a strong magnetic field in the case of ionization of atoms [4, 12] is restricted only by the case of scalar charged particles. Indeed, expressions (2) and (5) are quite consistent with this statement: according to them, the probability of the process is exponentially suppressed with an increase of the magnetic-field inten-

sity. However, relationships (3), (4), (6), in which contributions of various particle spin states in the magnetic field are taken into account, demonstrate a rise of the ionization probability with the increase in μ. Evidently, a cause of the different behavior of the ionization probabilities W_1 and W_2 in strong magnetic fields is the fact that the Landau level with the minimal energy (ground state) is attained only by particles with their spins aligned opposite to the direction of the magnetic field. With an elevation of the magnetic-field intensity, energies of all Landau levels different from the ground level increase. Therefore, the defining contribution to the level width of a spinor particle in a quantizing magnetic field is determined by the particle transition into the ground state whose energy is independent of H. However, for spinless particles, such a selected level is absent. As a result, as opposed to scalar particles, in the case of particles with the spin $s = \frac{1}{2}$, a rise in ionization, not its suppression, takes place with an increase of the magnetic-field intensity.

Similar differences in the dependences of the probabilities and cross sections of reactions in strong magnetic fields with participating spinor and scalar particles are well known. They are manifested, e.g., in the processes of e^+e pair photoproduction [3, 8, 9], as well as when studying the induced photoabsorption of nonconducting crystals in a quantizing magnetic field [13] and in reactions of the induced nuclear beta decay [14].

As is well known, numerous data obtained while investigating tunnel ionization of atoms and ions were accumulated in experiments with the application of optical radiation of the infrared, visible, and near ultraviolet ranges at wave-field intensities having attained $F \sim 0.1$ a.u. [7]. Under laboratory conditions, stationary magnetic fields $H \sim 3 \times 10^5$ G are formed with the help of cooled superconducting solenoids. Thus, the calculated values presented in figure are accessible presently in experiments with the use of laser beams and modern superconducting magnets. We can also expect the applications of the results obtained in experimental studies of processes associated with tunneling weakly coupled electrons in semiconductors in the case of crossed electric and magnetic fields.

ACKNOWLEDGMENTS

The authors are grateful to V.G. Kadyshevskiĭ and V.R. Khalilov for discussions of the results of the present study and important remarks.

The work was supported by the Russian Foundation for Basic Research, project no. 02-02-16784. It was also supported in part by the Competition Center of Fundamental Natural Science, St. Petersburg University, project no. E 00-3.1-457.

REFERENCES

1. L. V. Keldysh, Zh. Éksp. Teor. Fiz. **47**, 1945 (1964) [Sov. Phys. JETP **20**, 1307 (1964)].
2. A. M. Perelomov, V. S. Popov, and M. V. Terent'ev, Zh. Éksp. Teor. Fiz. **50**, 1393 (1966) [Sov. Phys. JETP **23**, 924 (1966)]; Zh. Éksp. Teor. Fiz. **51**, 309 (1966) [Sov. Phys. JETP **24**, 207 (1966)].
3. A. I. Nikishov and V. I. Ritus, Zh. Éksp. Teor. Fiz. **50**, 255 (1966) [Sov. Phys. JETP **23**, 168 (1966)].
4. V. S. Popov, B. M. Karnakov, and V. D. Mur, Zh. Éksp. Teor. Fiz. **113**, 1579 (1998) [JETP **86**, 860 (1998)].
5. N. P. Manakov, M. V. Frolov, B. Borca, and A. F. Starase, Pis'ma Zh. Éksp. Teor. Fiz. **52**, 426 (2000) [JETP Lett. **72**, 294 (2000)].
6. V. G. Kadyshevskiĭ and V. N. Rodionov, Teor. Mat. Fiz. **125**, 432 (2000).
7. N. B. Delone and V. P. Kraĭnov, Usp. Fiz. Nauk **168**, 531 (1998) [Phys. Usp. **41**, 469 (1998)].
8. I. M. Ternov, V. R. Khalilov, and V. N. Rodionov, *Interaction of Charged Particles with a Strong Electromagnetic Field* (Mosk. Gos. Univ., Moscow, 1982).
9. V. N. Rodionov, Zh. Éksp. Teor. Fiz. **113**, 23 (1998) [JETP **86**, 11 (1998)].
10. N. V. Rodionov and A. M. Mandel', Vestn. Mosk. Univ., Ser. 3: Fiz., Astron., No. 3, 25 (2001).
11. Yu. N. Demkov and G. F. Drukarev, Zh. Éksp. Teor. Fiz. **47**, 918 (1964) [Sov. Phys. JETP **20**, 614 (1964)].
12. G. F. Drukarev and B. S. Monozon, Zh. Éksp. Teor. Fiz. **61**, 956 (1971) [Sov. Phys. JETP **34**, 509 (1971)].
13. V. N. Rodionov, Vestn. Mosk. Univ., Ser. 3: Fiz., Astron., No. 2, 5 (1999).
14. V. N. Rodionov, Zh. Éksp. Teor. Fiz. **111**, 3 (1997) [JETP **84**, 1 (1997)].

Translated by G. Merzon

Doklady Physics, Vol. 47, No. 10, 2002, pp. 728–730. Translated from Doklady Akademii Nauk, Vol. 386, No. 4, 2002, pp. 468–470.

TECHNICAL PHYSICS

Barkhausen Effect in Alloys with Amorphous and Nanocrystalline Structures

Corresponding Member of the RAS É. S. Gorkunov*, V. V. Shulika, A. G. Lavrent'ev**, A. P. Potapov**, and G. S. Korzunin****

Received April 27, 2002

Depending on treatment conditions, $Fe_{73.5}Cu_1Nb_3Si_{13.5}B_9$ alloy can exist in both amorphous and nanocrystalline states. The magnetic behavior of this alloy is associated with its structural state, specific features of the domain structure, and the degree of stabilization of domain walls. By modifying the structure of ferromagnetic materials, it is possible to control their magnetic properties. Using the Barkhausen effect, additional information concerning both magnetic and structural properties of an alloy under study can be extracted [1].

In this study, we investigate the effect of phase inhomogeneity of the alloy on the distribution of Barkhausen jumps along the field applied and on a change of the critical fields of the magnetization reversal [2]. The comparison of distributions of the Barkhausen jumps in the chosen alloy with the nanocrystalline structure is performed for cases with stabilized and destabilized domain walls. The possibility of decreasing the interval of critical fields for the magnetization reversal in the nanocrystalline alloy under study by means of the destabilization of domain walls is analyzed.

Amorphous ribbons of $Fe_{73.5}Cu_1Nb_3Si_{13.5}B_9$ alloy were obtained by the method of melt quenching. The experiments were performed with strip and toroidal samples fabricated from these ribbons. In order to avoid quenching stresses, the amorphous samples were subjected to one-hour annealing in vacuum at a temperature of 350°C. To obtain the nanocrystalline structure, the samples were also annealed in vacuum at a temperature of 530°C for one hour. Various domain structures of the samples were obtained after annealing in a magnetic field. The thermomagnetic treatment was carried out in the following way. A sample was heated to a temperature of 530°C in a magnetic field and was held in the field at the same temperature for one hour. It was then cooled to room temperature at a rate of 200°C h^{-1} (the thermomagnetic treatment was combined with the phase transition in the alloy from its amorphous state into the nanocrystalline one). The magnetic field was oriented either along the long side of a sample or normally to it. To eliminate the destabilization of domain walls, a number of nanocrystalline samples were subjected to water quenching from the Curie temperature of 570°C (the classical method of domain-wall destabilization).

For the strip samples, we measured the electromotive force (EMF) $\bar{\varepsilon}$ (averaged over a period) of the Barkhausen jumps with a lay-on sensor. A lay-on electromagnet with a 7-mm pole gap served as a transducer. The magnetization reversal of the samples was performed by an alternating current at a frequency of 10 kHz. The magnetic-field intensity in the electromagnet gap was 0.5 A cm^{-1}. The signal from the measuring coil was fed to an amplitude detector determining the value of $\bar{\varepsilon}$ via a broadband amplifier with a transmission band of 200 kHz:

$$\bar{\varepsilon} = \frac{1}{T}\int_0^T |\varepsilon(t)|dt.$$

The flux of the Barkhausen jumps was visually observed on the oscilloscope screen [3]. For the toroidal samples, we measured static hysteresis loops and the initial magnetic permeability μ_a. In addition, we measured static hysteresis loops for the strip samples.

Figure 1 shows a histogram for the EMF (averaged over a period) of Barkhausen jumps, which was measured for $Fe_{73.5}Cu_1Nb_3Si_{13.5}B_9$-alloy samples under different conditions of the thermal and thermomagnetic treatments.

The magnetic properties of the samples manufactured from $Fe_{73.5}Cu_1Nb_3Si_{13.5}B_9$ alloy, which were obtained after the thermal and thermomagnetic treatments in the conditions indicated in Fig. 1, are listed in the table.

* *Institute of Engineering Science, Ural Division, Russian Academy of Sciences, Yekaterinburg, Russia*

** *Institute of Metal Physics, Ural Division, Russian Academy of Sciences, ul. S. Kovalevskoĭ 18, Yekaterinburg, 620219 Russia*

1028-3358/02/4710-0728$22.00 © 2002 MAIK "Nauka/Interperiodica"

Analysis of the experimental data shows that the value of $\bar{\varepsilon}$ is minimal for the amorphous sample rather than for the nanocrystalline sample with unique soft magnetic properties (see Figs. 1*a* and 1*b*). This result can be readily understood by analyzing Fig. 2, in which oscillograms of amplitude envelopes of the flux of the Barkhausen jumps for the amorphous and nanocrystalline samples are presented. In the amorphous alloy, the distribution of the Barkhausen jumps along the field obeys the Gaussian law (Fig. 2a). This is caused by the presence in the sample of small domains of magnetization reversal with critical fields distributed in a random fashion. In the nanocrystalline sample, we observe two regions of the critical fields of the magnetization reversal on an oscillogram of the amplitude envelope for the flux of the Barkhausen jumps (Fig. 2b). This is associated with the existence of two magnetic phases characterized by different distribution of critical fields and different coercive forces: remnants of the amorphous phase and the appearance of the α-Fe/Si phase [4]. The presence of the magnetic inhomogeneity results in an increase in $\bar{\varepsilon}$ of the nanocrystalline sample compared to that in the amorphous one.

The destabilization of domain walls in the nanocrystalline sample by the thermomagnetic treatment in an alternating magnetic field increases their mobility [5]. Magnetically, the material becomes more homogeneous: the distribution of the critical fields of the magnetization reversal in two phases becomes closer and, accordingly, the interval between field dependences of the critical fields becomes narrower. This results in an overlapping of the distributions of the critical fields (Fig. 2c). In this case, the value of $\bar{\varepsilon}$ decreases by 30% compared to that measured in the sample after the annealing in the absence of an external magnetic field, i.e., in the sample with stabilized domain walls (Figs. 1*b* and 1*c*).

It should be noted that the classical method of destabilizing the domain structure, namely, water quenching from the Curie temperature, increases $\bar{\varepsilon}$ in the nanocrystalline $Fe_{73.5}Cu_1Nb_3Si_{13.5}B_9$ alloy. Apparently, this is caused by the fact that, as a result of quenching, internal stresses in the sample are increased, as evidenced by an increase in H_c (see table), an effect which leads to a rise of $\bar{\varepsilon}$.

In the nanocrystalline sample, the maximum value of $\bar{\varepsilon}$ is observed after the thermomagnetic treatment in a longitudinal field (Fig. 1*d*). This is explained by the fact that the uniaxial anisotropy arising after thermomagnetic treatment in a longitudinal constant field leads to an increase in the magnetic texture and to the formation of larger complexes of domains that undergo magnetization reversal in several large jumps. The resemblance of the hysteresis loop to a rectangular one

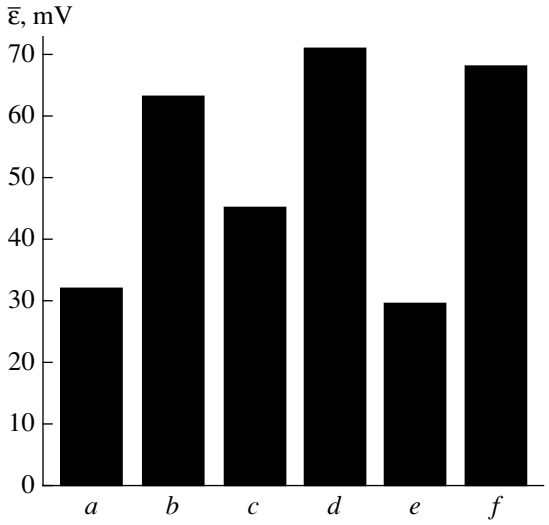

Fig. 1. Histogram of the EMF (averaged over a period) for the flux of Barkhausen jumps for samples of $Fe_{73.5}Cu_1Nb_3Si_{13.5}B_9$ alloy after different treatments: (*a*) annealing at a temperature of 350°C; (*b*) annealing at a temperature of 530°C; (*c*) thermomagnetic treatment of a nanocrystalline sample in a longitudinal alternating magnetic field; (*d*) thermomagnetic treatment of a nanocrystalline sample in a longitudinal constant field; (*e*) thermomagnetic treatment of a nanocrystalline sample in a transverse constant magnetic field; and (*f*) water quenching from the temperature of 570°C.

$\left(\frac{B_r}{B_m} = 0.99\right)$ and the high maximum magnetic permeability testify to the validity of this assumption.

For thermomagnetic treatment in a transverse constant magnetic field, a uniaxial anisotropy perpendicular to the field direction appears when measuring. As a result of the treatment, the domain structure is comminuted, and, as a consequence, $\bar{\varepsilon}$ decreases. It is worth

Magnetic properties of $Fe_{73.5}Cu_1Nb_3Si_{13.5}B_9$ alloy after different treatments

Treatment	μ_a	μ_{max}	H_c, A cm^{-1}
350°C, 1 h	5000	40000	0.04
530°C, 1 h	40000	500000	0.007
Thermomagnetic treatment, $H_{\sim\parallel}$	60000	1000000	0.005
Thermomagnetic treatment, $H_{=\parallel}$	35000	1200000	0.005
Thermomagnetic treatment, $H_{=\perp}$	1000	25000	0.06
Water quenching	10000	30000	0.02

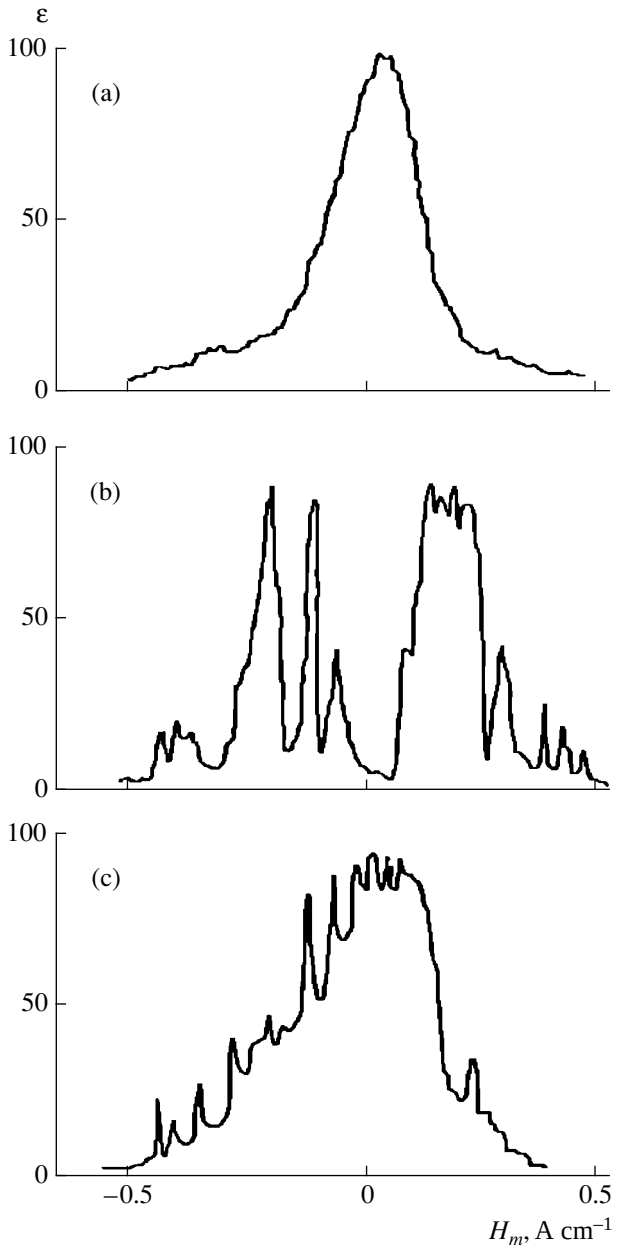

Fig. 2. Oscillograms of amplitude envelopes for the flux of the Barkhausen jumps ε in the case of $Fe_{73.5}Cu_1Nb_3Si_{13.5}B_9$ alloy after treatments: (a) annealing at a temperature of 350°C, (b) annealing at a temperature of 530°C, and (c) thermomagnetic treatment of a nanocrystalline sample in a longitudinal alternating magnetic field.

noting that under this treatment, the initial and maximum magnetic permeabilities considerably decrease.

Thus, based on the investigation carried out, we may conclude that

(i) the EMF (averaged over a period) for the flux of the Barkhausen jumps in $Fe_{73.5}Cu_1Nb_3Si_{13.5}B_9$ alloy is smaller in its amorphous state than that in the crystalline one;

(ii) destabilization of the domain walls in the nanocrystalline alloy by means of thermomagnetic treatment in an alternating magnetic field increases the magnetic permeability of the alloy and decreases the EMF (averaged over a period) of the flux of Barkhausen jumps by 30% compared to that for the alloy with the stabilized domain structure;

(iii) the refining of the domain structure of the nanocrystalline sample for $Fe_{73.5}Cu_1Nb_3Si_{13.5}B_9$ alloy after the thermomagnetic treatment in a transverse magnetic field decreases the EMF (averaged over a period) for the flux of the Barkhausen jumps by a factor of two compared to that observed after annealing in the absence of the magnetic field. However, the magnetic permeability is lowered in this case; and

(iv) parameters of the Barkhausen jumps can be used to determine the structural and magnetic states of alloys.

ACKNOWLEDGMENTS

This work was supported by the Russian Foundation for Basic Research, project no. 01-02-96442.

REFERENCES

1. É. S. Gorkunov and Yu. N. Dragoshanskiĭ, Defektoskopiya, No. 6, 3 (1999).
2. V. M. Rudyak, Usp. Fiz. Nauk **101**, 420 (1970) [Sov. Phys. Usp. **13**, 461 (1970)].
3. G. S. Korzunin and A. G. Lavrent'ev, Defektoskopiya, No. 6, 24 (1999).
4. T. Kulik, A. Hernando, and M. Vázquez, J. Magn. Magn. Mater. **133**, 310 (1994).
5. V. V. Shulika and A. P. Potapov, *Non-Linear Electromagnetic Systems* (IOS Press, Oxford, 1998), pp. 579–581.

Translated by Yu. Vishnyakov

Doklady Physics, Vol. 47, No. 10, 2002, pp. 731–734. Translated from Doklady Akademii Nauk, Vol. 386, No. 4, 2002, pp. 471–474.

ASTRONOMY, ASTROPHYSICS, COSMOLOGY

On a Large-Scale Model of the Universe

Academician S. S. Grigoryan

Received January 15, 2002

In modern cosmology, that is, the science of the Universe, concepts and results based on the construction and analysis of the simplest solutions to equations of the general theory of relativity (GTR) (Einstein's gravitational theory and its modern modifications) are altogether accepted and almost canonized. A substantial initial assumption is the so-called Cosmological Principle, namely, the assumption that the spatial distribution of the parameters of the Universe is homogeneous and isotropic. However, solutions to the ordinary differential equations obtained in this case (Friedmann solutions and others similar to them) have a number of properties presenting challenging problems. We have in mind the finiteness of the lifetime of the Universe; the possible spatial boundedness (closure) of the Universe; the singularity of its initial state; the necessity of an explosive pulse giving rise to its expansion; and the production of strange (also singular) formations in the course of the evolution of localized masses of matter: black holes, etc. These are the unavoidable predictions of the solutions obtained in the framework of the GTR. Therefore, it is natural that attempts to radically improve the gravitational theory of matter with the goal of obtaining more realistic results in describing the structure and dynamics of the Universe are still in progress.

Fairly recently, Academician A.A. Logunov and coworkers constructed a gravitational-field theory [called the relativistic theory of gravitation (RTG)]. This theory radically differs from the GTR and is free of all the awkwardnesses of GTR predictions with respect to the large-scale model of the Universe, the evolution of localized masses of matter, etc. [1]. The RTG is based on the natural concept of the gravitational field as a conventional physical field similar to the electromagnetic and other fields embedded in the pseudo-Euclidean Minkowski space in which all physical laws are represented uniformly and invariantly with respect to the Lorentz transformations. In [1], there is a section devoted to analyzing the large-scale model of the Universe in terms of the RTG. In this study, as in other ones devoted to modern cosmology, the Cosmological Principle is taken as an initial assumption, and a time-dependent solution for describing the structure and dynamics of the Universe is constructed. According to this solution, matter is at rest in the large-scale consideration of the Universe, and its unsteadiness is induced by the time variability of the gravitational field; this is a variability that is quantitatively described by the constructed solution. This solution does not have the unacceptable properties of the Friedmann solutions and their modifications. Although fluctuations of the Universe's parameters are strictly periodic in time, no singular states appear: the density, temperature, and pressure do not become infinite, the linear scale does not vanish, etc. However, this solution has another drawback. As was noted above, according to this solution, the gravitational field oscillates with time synchronously at all points with the matter being quiescent. However, the nature of this effect and its adequacy are not discussed in this study. We consider this effect as unacceptable for the large-scale description of the Universe, because this is a purely theoretical or mathematical result arising due to the fact that the author, following Friedmann, assumed the unsteadiness of universal dynamics and, naturally, constructed a time-dependent solution. In this regard, we recall that Einstein also tried to construct a time-independent solution to the gravitational equations in due time and, because of the absence of such a solution, had to modify the GTR equations, i.e., had to supplement them with λ terms. (Later, this λ modification of the GTR equations was declared by him as his most serious mistake.) The intention of Einstein to solve this problem in such a way was natural: from the initial concepts regarding a spatially infinite and time-invariant Universe (which, of course, arose from the observation of the picture of "immobile" stars by many generations of people), an attempt followed to primarily construct just a time-invariant theoretical picture of the Universe on a large scale. However, in contrast to the GTR equations, the Logunov RTG equations admit a time-independent solution for the model of the homogeneous and isotropic Universe. This solution is constructed by a very simple method, which is made in this study.

The basic RTG equations for a homogeneous and isotropic model of the Universe are Eqs. (10.24) and (10.25) from [1]:

$$\frac{1}{R}\frac{d^2R}{dt^2} = -\frac{4\pi G}{3}\left(\rho + \frac{3p}{c^2}\right) - 2\omega\left(1 - \frac{1}{R^6}\right), \qquad (10.24)$$

Research Institute of Mechanics, Moscow State University, Vorob'evy gory, Moscow, 119899 Russia
Central Clinical Hospital "Uzkoe," Moscow

1028-3358/02/4710-0731$22.00

$$\left(\frac{1}{R}\frac{dR}{dt}\right)^2 = \frac{8\pi G}{3}\rho - \frac{\omega}{R^6}\left(1 - \frac{3R^4}{a} + 2R^6\right). \quad (10.25)$$

Here, R is the dimensionless scale parameter of the model;[1] t is time; ρ and p are the density and pressure of matter, respectively; G is the gravitational constant; c is the speed of light in free space; ω is the constant of the model, and

$$\omega = \frac{1}{12}\left(\frac{mc^2}{\hbar}\right)^2. \quad (10.26)$$

Furthermore, m is the graviton mass (this quantity necessarily arises in the RTG) and $\hbar$ is Planck's constant. The parameter a is a certain integration constant linking the quantities V and U by the relation $V = aU^{1/3}$, where U and V are the parameters of the metric of the effective Riemann space induced by the gravitational field. The metric in this model has the form

$$(dS)^2 = U(cdt)^2 - V\{(dr)^2 - r^2[(d\theta)^2 + \sin^2\theta(d\Phi)^2]\},$$

where r, θ, and Φ are the spherical coordinates. The quantities U and R are connected by the relationship $U = R^6$.

We construct the time-independent solution to Eqs. (10.24) and (10.25) by assuming that $p = 0$, which is well corroborated by the observational data within the visible region of the Universe. For R = const (stationary case), $p = 0$, and $\omega \neq 0$, Eqs. (10.24) and (10.25) yield the steady-model relationships

$$\begin{aligned} \rho &= \frac{3\omega}{2\pi G}(x-1) \equiv \rho_*(x-1), \\ p &= 0, \quad v_i = 0, \quad i = 1, 2, 3, \\ (dS)^2 &= \frac{1}{x}(Cdt)^2 \\ &- \frac{1}{2-x}\{(dr)^2 - r^2[(d\theta)^2 + \sin^2\theta(d\Phi)^2]\}, \\ a &= \frac{x^{1/3}}{2-x}, \quad R^6 = \frac{1}{x}. \end{aligned} \quad (1)$$

Here, v_i is the velocity of matter. The constant parameters a and R should satisfy the inequality

$$R^2(R^4 - a) \leq 0, \quad (10.30)$$

which expresses the causality principle [1]. This implies that values of the parameter x in model (1) must lie within the interval

$$1 \leq x \leq 2. \quad (2)$$

For the constructed time-independent solution, it follows from relationships (10.20) and (10.21) of [1] that the curvature tensor of the effective Riemann space is zero; i.e., this space is pseudo-Euclidean like the initial Minkowski space in which the steady model is embedded. In the absence of matter ($\rho = 0$ but $\omega \neq 0$), $x = a = R = 1$, and these two spaces coincide, which in the general case is predicted by the RTG [1]. As $x \longrightarrow 2$, the effective-space metric very strongly deviates from the initial Minkowski-space metric, although, according to (1), the density varies only slightly and remains limited from above by a very small value ρ_*. In this case, the speed of light sharply decreases (there is a factor $\sqrt{\frac{2-x}{x}}$ ahead of c).

It is significant that the constructed solution is nontrivial only due to the presence of a nonzero graviton rest mass ($\omega \neq 0$), which is the most important property of the RTG. For $\omega = 0$, relationships (1) cannot be derived from (10.24), (10.25) when R = const.

The time-independent solution has a very important property. It is infinite in time and space, the space is pseudo-Euclidean and homogeneous, and matter is quiescent with respect to it. But this is just the natural material reference space into which an inertial coordinate system is introduced. This space represents a concrete and very simple realization of the Mach principle [1]. Indeed, according to this solution, the matter homogeneously and invariably in time fills the Minkowski empty space, with all its parts being equivalent and identical. In the case of conceptual displacements along this space in an arbitrary direction, no changes are observed, because everywhere there exists a mass distributed geometrically identically. This occurs at arbitrary distances; i.e., no problem arises concerning the particular understanding of physical infinity (everywhere, there is quiescent matter with respect to which it is possible to count off geometrical quantities, and to which the coordinate system mathematically expanded into infinity can be related).

At the same time, the constructed model has a feature requiring the discussion and formulation of a new and apparently very difficult mathematical problem. The case in point is that matter actually moves instead of being at rest as follows from (1), and, at small scales, the model constructed is certainly unsuitable for describing the Universe. This model should be considered only as that obtained by the mathematical operation of averaging from a more complicated essentially inhomogeneous and unsteady model thoroughly describing the Universe filled with various scales of

[1] In [1], the following units of measurement are taken: $L = \sqrt{\frac{G\hbar}{c^3}} = 1.6 \times 10^{-33}$ cm, $T = \frac{L}{c} = 5.3 \times 10^{-44}$ s, $M = \sqrt{\frac{G\hbar}{G}} \approx 2.1 \times 10^{-5}$ g.

Although these values are very small and cannot serve as characteristic quantities in cosmological problems, this fact does not interfere with the general analysis performed in [1].

clumps of matter which participate in an infinite process of gravitational compression and their replacement by explosive disintegration and matter divergence. The observed motion of matter (e.g., of stars, galaxies, various sizes of clusters of galaxies) and its inhomogeneous spatial distribution must be considered as fluctuations against an averaged, homogeneous, isotropic, and steady background. The dynamics and structure of the Universe in such a detailed consideration, instead of that averaged over vast scales, is described by the author in general (principal) outlines in [2]. According to [2], the detailed dynamics of the Universe represent a struggle between gravitation tending to ultimately compress various sizes of matter clumps and the processes of high-energy physics proceeding in these clumps in the case of their severe compression. For relatively large masses of the clumps, these processes initiate evolution accomplished by the explosive disintegration of the clumps and divergence of their matter to significant distances (the processes of the supernova-explosion type). The Big Bang, effects of recession of galaxies observed at present, and the existence of relic radiation are examples of the evolution of such a clump, but a very large one. (For this example, an important and still unsolved problem on the unsteady evolution of a so-called island system arises. A steady case of such a system was studied in [1].) Thus, according to [2], the matter in the Universe represents a specific gas that is composed of various scales of clumps compressed by gravitation and disintegrated by their internal explosion and is then formed anew from the diverged matter of the previous clumps. This gas dynamics is played out against the homogeneous, isotropic, and steady background.

Here, the question arises as to whether or not the steady model obtained by averaging the detailed model over large scales coincides with the model constructed above. This question is nontrivial, because the mathematical relationships of the RTG are essentially nonlinear and, in their formal mathematical averaging with a given averaging scale, residuals of the Reynolds stress type existing in hydrodynamics arise due to the nonlinearity. For this reason, when constructing the model in terms of average values, a closure problem arises as in the theory of turbulence in hydrodynamics. For example, it is clear that in the averaged model, in particular, a certain averaged quantitative measure for the motion of matter must appear, which is absent in the above-constructed model. In this regard, this model is valuable in the qualitative but not quantitative sense: a possibility is shown of constructing a steady, homogeneous, and isotropic solution, namely, in terms of the RTG. With this solution, it is possible to relate the physical (material) pseudo-Euclidean space playing the role of the absolute space (instead of the physical ether) and satisfying the Mach principle [1].

The solution to the closure problem leading to the construction of the model in terms of average values depends, generally speaking, on the averaging scale. For our cosmological problem, the following result must certainly be obtained: the averaged model is independent of the averaging scale starting with a certain value of this scale. Only in this case is it possible to construct a homogeneous and isotropic solution of the above type for the averaged model and connect the physical reference space with it. Whether or not such a solution to the averaged model coincides in both form and principal details of final formulas with that constructed above remains an open question. To answer this question, which depends on the possibility of an efficient realization of the averaging procedure for the RTG exact equations in the model of the Universe, the following estimates, which are of substantial importance for this paper and for themselves, may help.

Using for the graviton rest mass the value $m = 10^{-66}$ g taken in [1], we obtain for ρ_* from [1] the value $\rho_* = 5 \times 10^{-31}$ g cm^{-3}. The steady background density ρ taken in (1) is lower than ρ_* by virtue of (2). At the same time, the averaged density of the Universe region under current observation is $\rho_m = 10^{-29}$ g cm^{-3}, i.e., 20 times higher than ρ_*. This fact must not confuse us, because, according to the empirical Hubble law, an intense expansion continues in our very large matter bunch, and the bunch density gradually decreases. Of course, in due time, according to (1), it will become substantially lower than both ρ_* and the background density ρ because, when the bunch diverges, the matter can also diverge, so that a rarefaction is developed in the bunch with respect to the background. However, another factor is of importance, namely, that values of ρ_* (and the background density ρ) and ρ_m differ only slightly (by only a factor of 20, which can be considered as a trivial distinction in this problem). On the other hand, since the graviton mass m quadratically enters into the expression for ρ_*, it is sufficient to increase the value of m only by a factor of $\sqrt{20} \approx 4.5$ in order to equalize ρ_* and ρ_m. At the same time, an increase in m by the factor of 45 leads to increasing ρ_* by 2000 times; i.e., we have $\rho_* = 10^{-27}$ g cm^{-3}, and we need the value of $x - 1 = \dfrac{\rho_m}{\rho_*} = 0.01$ in order to equalize the background density and ρ_m. The background density can be substantially lower than ρ_m. For example, for this reason, if our bunch expands by further 10 times, ρ_m decreases by three orders of magnitude and becomes equal to the background density. In this case, we obtain $x - 1 = 0.02$ even for $m = 10^{-66}$ g. If in this case m is increased by a factor of 4.5, we arrive at $x - 1 = 10^{-3}$. Since the variations in m under consideration are quite acceptable (an exact value of m is unknown), the general conclusion from the presented estimates is that $x - 1 \equiv \varepsilon \ll 1$. By virtue of (1), this implies that the deviation of the effective averaged material space from the

empty Minkowski space is negligibly small (on the order of ε). In other words, we may state that the initial Minkowski space with a high accuracy represents the actual material physical space corresponding to the Mach principle. On the other hand, the background averaged density $\rho = \rho_*\varepsilon$ of matter is also quite low; i.e., the matter is very rarefied in the Universe. These two arguments enable us to hope that substantial simplifications can be made in the procedure of averaging the RTG nonlinear relationships for the problem under consideration. These simplifications will make it possible to efficiently solve this problem and to answer the posed question. In this case, it is possible that the above analogy between a cluster of pulsating-matter bunches and gas will turn out to be deeper. We imply that, when averaging, we will succeed in introducing the notion of temperature, pressure, and other averaged characteristics for the gas of these bunches and in constructing the corresponding thermodynamics and gas kinetics of the Universe.

We present one more formula for estimating the maximum scale l of averaging. When exceeding this scale, the averaged model is independent of the averaging scale. This formula can be derived from the considerations of dimensional theory after accepting an assumption natural for our problem that the scale l (the same scale determines on the order of magnitude of a maximum size for a material bunch in the gas of the Universe) determines unsteady gravitational processes (with the possible participation of relativistic effects) of the evolution of inhomogeneities against a homogeneous background. These inhomogeneities are induced by the dynamic instability of the background. (The problem of background stability in terms of the RTG must be formulated and solved.) This implies that l depends on the parameters G, c, $\rho = \rho_*(x - 1)$. From dimensional theory, we find

$$l = \frac{c}{\sqrt{\rho_*(x-1)G}}\text{const}. \qquad (3)$$

The substitution of values c, G, and the results of the above estimates for ρ_* and $x - 1$ into (3) yields $l \sim 10^{29}$ cm $\sim 10^{11}$ light years. For comparison, this is only 5–7 times larger than the age of the Universe according to modern cosmology.

It should also be noted that, according to (1), the speed of light $\tilde{c}$ in averaged space differs from the speed c in free space by the value $\Delta c = \tilde{c} - c = \varepsilon c$; the smallness of ε also implies the smallness of this deviation. It is possible that using only this estimate of Δc, we can obtain an independent estimate of ε from observations.

The fundamental mathematical problems generated by the problem of averaging physical fields were formulated and discussed by the author in [3].

REFERENCES

1. A. A. Logunov, *Theory of the Gravitational Field* (Nauka, Moscow, 2001).
2. S. S. Grigoryan, Tr. Mat. Inst. Akad. Nauk SSSR **186**, 91 (1989).
3. S. S. Grigoryan, Dokl. Akad. Nauk **254**, 846 (1980) [Sov. Phys. Dokl. **25**, 827 (1980)].

Translated by V. Bukhanov

Doklady Physics, Vol. 47, No. 10, 2002, pp. 735–737. Translated from Doklady Akademii Nauk, Vol. 386, No. 4, 2002, pp. 475–477.

MECHANICS

The Wave Field in a Medium with a Complicated Dispersion Law

A. A. Vikhorev and E. M. Chesnokov

Presented by Academician V.P. Myasnikov May 16, 2002

Received May 18, 2002

Modeling and investigating wave processes in macroinhomogeneous and microinhomogeneous anisotropic media are one of the topical problems in both seismology and composite-materials theory. In geophysics, modeling wave fields is often aimed at the comparison of seismic signals for a vertical-inhomogeneous (reference) reservoir with a perturbed one that contains certain three-dimensional inclusions and more general macroscopic inhomogeneities. The present study is devoted to the development of a normal-wave method suitable for investigating wave processes in complicated media with three-dimensional inhomogeneity.

Microscopic inhomogeneities are taken into account with the help of efficient-parameter theory [1, 2]. As a result, a microinhomogeneous medium is replaced by an equivalent medium having nontrivial dispersion properties, which allows the resonance and dissipative phenomena inherent in an actual medium to be observed [3, 4]. If a macroscopic inhomogeneity is additionally presented in the medium, then along with the appearance of dispersion, the coordinate dependence is preserved in its local quantities. In this case, the equivalent medium remains inhomogeneous but contains only large-scale inhomogeneities. Therefore, the application of spectral methods makes it possible to simplify the problem under consideration and to present the wave field generated by a point source in the form of a superposition of normal waves, each of them being an independent scalar wave. An arbitrary scalar wave (or normal mode) may be interpreted as an excitation propagating in such a homogeneous equivalent medium in which the dispersion law corresponding to this medium is realized. Hence, in the momentum representation, a normal wave is a generalized solution to the equation that determines the interconnection between the frequency and the wave vector [5, 6].

Gamburtsev Institute of Earth's Physics, Russian Academy of Sciences, Bol'shaya Gruzinskaya ul. 10, GSP-5, Moscow D242, 123995 Russia

E-mail: vikhorev@uipe.ras.scgis.ru; echesnok@hoth.gcn.ou.edu

We now use denotations for space–time 4-vectors $x = \{x_0, \mathbf{x}\}$, where $x_0 = ct$, and a wave vector $k = \{k_0, \mathbf{k}\}$ with the frequency ω, where $k_0 = \frac{\omega}{c}$. The dispersion law for a normal wave can be formulated in the implicit form

$$L(k) = k^\nu k_\nu - M^2(\mathbf{k}) = 0, \quad \nu = 0, 1, 2, 3. \qquad (1)$$

The function $L(k)$ must vanish on the dispersion branch

$$M^2(\mathbf{k}) = \left(\frac{\omega(\mathbf{k})}{c}\right)^2 - \mathbf{k}^2, \quad \mathbf{k}^2 = -k^i k_i, \quad i = 1, 2, 3, \qquad (2)$$

where $\omega(\mathbf{k})$ is the explicit dependence of the frequency on the wave vector and $\omega(\mathbf{k}) = \omega(-\mathbf{k})$. According to our assumption, at large $|\mathbf{k}|$, the function $\omega(\mathbf{k})$ approaches a hyperbolic one. The short-wave limit of the phase velocity c plays the role of the absolute velocity. Below, function (2) representing a deviation from the linear law of dispersion is conditionally called the mass squared.

A wave excited by a point source in a homogeneous medium given by dispersion law (1) is described by a retarding Green's function ψ:

$$\begin{aligned} \psi(x) &= \theta(x_0)\mathcal{F}_k[\tilde{\varphi}(k)](x), \\ \tilde{\varphi}(k) &= -i\,\mathrm{sgn}(k_0)\delta(L(k)), \end{aligned} \qquad (3)$$

where $\mathcal{F}_k$ is an inverse four-dimensional Fourier transformation. The spectral density $\tilde{\varphi}$ is the δ-function on the manifold $L(k) = 0$. It satisfies the homogeneous equation

$$(k^\nu k_\nu - M^2(\mathbf{k}))\tilde{\varphi}(k) = 0. \qquad (4)$$

The Fourier transform of the retarding Green's function $\psi(x)$ is a solution to corresponding inhomogeneous equation

$$(k^\nu k_\nu - M^2(\mathbf{k}))\tilde{\psi}(k) = 1,$$

which corresponds to Eq. (4).

The goal of the present study is to derive a form of Eq. (4) that is invariant with respect to transformations of the Poincaré group and to find the solution $\psi(x)$ in

1028-3358/02/4710-0735$22.00

the coordinate representation. The invariance of the equation is necessary to satisfy the causality principle in the process of the wave propagation. According to theorems proved in [7], an equation of the form $L\varphi = 0$ is invariant with respect to the continuous transformation group if the equation operator L commutes with all elements of the Lee algebra for this group. For constant mass parameter, Eq. (4) coincides with the Klein–Gordon–Fok equation, and its operator commutes with all elements of the Poincaré algebra [7]. It turns out that in the case of a complicated dispersion law when the parameter M depends on the vector $\mathbf{k}$, for the preservation of the Poincaré invariance, a special extension of the mass-squared function beyond the dispersion branch is required. This is caused by the fact that, in the general case, the operator of Eq. (4) does not commute with generators of the rotation and of the Lorentz transformations

$$J_{\mu\nu} = k_\mu \frac{\partial}{\partial k^\nu} - k_\nu \frac{\partial}{\partial k^\mu}.$$

The behavior of the function $L(k)$ in the zero point completely determines the solution to Eq. (4). Therefore, the continuation of the function $\tilde{\Lambda}(k)$ of the mass squared satisfies the boundary conditions on the dispersion branch:

$$\tilde{\Lambda}(k)\big|_{L(k)=0} = M^2(\mathbf{k}), \quad [J_{\mu\nu}, \tilde{\Lambda}(k)]\big|_{L(k)=0} = 0. \quad (5)$$

The desired invariant form of Eq. (4) is

$$(k^\nu k_\nu - \tilde{\Lambda}(k))\tilde{\varphi}(k) = 0. \quad (6)$$

By virtue of conditions (5), the operator of Eq. (6) commutes on the dispersion branch with all elements of the Poincaré algebra. In the k-representation, the solutions to Eqs. (4) and (6) coincide; however, these equations possess different transformation properties. In the case of the replacement of k_0 by a new variable

$$\eta = k_0 - \mathrm{sgn}(k_0)\sqrt{\mathbf{k}^2 + M^2(\mathbf{k})}$$

equal to zero on the manifold $L(k) = 0$, conditions (5) consisting of seven equations are reduced to two "initial" conditions for the function $\tilde{\Lambda}(\eta, \mathbf{k})$:

$$\tilde{\Lambda}(\eta, \mathbf{k})\big|_{\eta=0} = M^2(\mathbf{k}), \quad \left.\frac{\partial\tilde{\Lambda}(\eta, \mathbf{k})}{\partial\eta}\right|_{\eta=0} = 2k_0, \quad k_0 = \pm\sqrt{\mathbf{k}^2 + M^2(\mathbf{k})}. \quad (7)$$

Since the behavior of the function $\tilde{\Lambda}(k)$ on the three-dimensional manifold $L(k) = 0$ completely determines solution (6), the four-dimensional Fourier transformation

$$\tilde{\Lambda}(k) = \int d^4x \Lambda(x) e^{-ix^\nu k_\nu} \quad (8)$$

must be reversible on a three-dimensional manifold. In other words, the function $\Lambda(x)$ must be completely determined only by the behavior of $\tilde{\Lambda}(k)$ on the dispersion branch. Hence, $\Lambda(x)$ is the function of a simple layer on an invariant three-dimensional manifold in space–time:

$$\Lambda(x) = \theta(x_0)\delta(x_\nu x^\nu - a^2)\lambda(x). \quad (9)$$

Here, the choice of the positive time coordinate $x_0 > 0$ corresponds only to retarding solutions for the wave field. Integrating over the coordinate x_0 in representation (8) with allowance for form (9) and reversing the three-dimensional transform obtained, we arrive at (see [6])

$$\lambda(x) = \int d^3\mathbf{k} e^{ik_\nu x^\nu}\left(x_0 - i\frac{\partial}{\partial k_0}\right)\tilde{\Lambda}(k), \quad k_0 = \pm\sqrt{\mathbf{k}^2 + M^2(\mathbf{k})}. \quad (10)$$

Here, integration of the function $\tilde{\Lambda}(k)$ occurs on the dispersion branch, i.e., at $L(k) = 0$. However, in this case, the integrand is completely determined by conditions (7)

$$\lambda(x) = \int d^3\mathbf{k} e^{ik_\nu x^\nu}(x_0 M^2(\mathbf{k}) - i\cdot 2k_0), \quad k_0 = \pm\sqrt{\mathbf{k}^2 + M^2(\mathbf{k})}. \quad (11)$$

In this case, in integrals (10) and (11), the value of the coordinate $x_0 = \sqrt{\mathbf{x}^2 + a^2}$ is fixed.

Differentiating representation (8) with respect to components k with allowance for form (9), we find that beyond the dispersion branch, the function of the continuation of $\tilde{\Lambda}(k)$ is the solution to the Cauchy problem for the equation

$$(\Box_k + a^2)\tilde{\Lambda}(k) = 0 \quad (12)$$

with initial conditions (7) (for the change of variable $k_0 \longrightarrow \eta$). The condition of the uniqueness of the solution to the given problem is proved in [5]. For constant mass squared, the continuation function must also be constant; this is the condition of the limiting process. However, in this case, in accordance with Eq. (12), the parameter a should be set to zero.

We write out Eq. (6) in the coordinate representation. The corresponding inhomogeneous equation has the form

$$\Box_x\psi(x) + \int d^4x' \Lambda(x')\psi(x - x') = \delta^4(x), \quad (13)$$

where the D'Alembert operator is denoted by its usual symbol. We now begin to search for a retarding solution $\psi(x)$. We perform the Laplace transformation for both

parts of Eq. (13) over the time coordinate x_0 with the parameter $p_0 = p$ and seek the transform $\breve{\psi}(p, \mathbf{x})$ of the desired function $\psi(x_0, \mathbf{x})$ in the form of a convolution

$$\breve{\psi}(p, \mathbf{x}) = \int d^3\mathbf{x}' \times \sum_{s=1}^{n} \bar{V}_s(p, 0) V_s(p, \mathbf{x}') \breve{D}(p, \mathbf{x} - \mathbf{x}'; m_s(p)). \quad (14)$$

Here, $V_s(p, \mathbf{x}')$ are the eigenfunctions of the symmetric kernel $\breve{\Lambda}(p, \mathbf{x} - \mathbf{x}')$ that corresponds to the Laplace transform of the original function $\Lambda(x)$ [formulas (9), (11)]:

$$\int d^3\mathbf{x}' \frac{e^{-p|\mathbf{x}'|}}{2|\mathbf{x}'|} \lambda(\mathbf{x}') V_s(p, \mathbf{x} - \mathbf{x}') = m_s^2(p) V_s(p, \mathbf{x}). \quad (15)$$

The transform $\breve{D}(p, \mathbf{x}; m)$ of Green's function with the mass parameter m is of the form

$$\breve{D}(p, \mathbf{x}; m) = \frac{1}{4\pi|\mathbf{x}|} e^{-|\mathbf{x}|\sqrt{p^2 + m^2}} \quad (16)$$

and satisfies the equation

$$(p^2 - \Delta_x + m^2) \breve{D}(p, \mathbf{x}; m) = \delta(\mathbf{x}).$$

Function (14) is the solution to transformed equation (13) provided that the eigenfunctions of problem (15) form a complete orthogonal system and, hence, at each fixed p, with an increase in the number of terms n, the sum

$$\lim_{n \to \infty} \sum_{s=1}^{n} \bar{V}_s(p, 0) V_s(p, \mathbf{x}) = \delta(\mathbf{x}), \quad \mathrm{Re}(p) > 0$$

converges to the δ function. Thus, if problem (15) admits constructing a discrete finite-dimensional analog, then solution (14) can be represented as a sum of transforms for elementary waves forming the desired wave $\psi(x)$. The transform of each elementary wave is described by Green's function (16) with the mass parameter $m = m_s(p)$.

REFERENCES

1. T. D. Shermergor, *Elasticity Theory of Microinhomogeneous Media* (Nauka, Moscow, 1977).
2. I. O. Bayuk and E. M. Chesnokov, Fiz. Zemli, No. 11, 40 (1999).
3. S. A. Shapiro and P. Hurbal, *Elastic Waves in Random Media* (Springer, Berlin, 1999).
4. E. M. Chesnokov, J. H. Queen, A. A. Vikhorev, *et al.*, in *Expanded Abstracts of LXXI Annual Meeting of SEG International Exposition, Frequency-Dependent Anisotropy, September 9–14, 2001, San Antonio*, Vol. 1, ANI 1.9.
5. V. S. Vladimirov, *Equations of Mathematical Physics* (Nauka, Moscow, 1988; Mir, Moscow, 1984; M. Dekker, New York, 1971).
6. N. N. Bogolyubov and D. V. Shirkov, *Introduction to the Theory of Quantized Fields* (Nauka, Moscow, 1984; Wiley, New York, 1980; Interscience Publishers, New York, 1959).
7. V. I. Fushchich and A. G. Nikitin, *Symmetries of Quantum-Mechanical Equations* (Nauka, Moscow, 1990; Naukova Dumka, Kiev, 1983; Reidel, Dordrecht, 1987).

Translated by G. Merzon

Doklady Physics, Vol. 47, No. 10, 2002, pp. 738–741. Translated from Doklady Akademii Nauk, Vol. 386, No. 4, 2002, pp. 478–481.

MECHANICS

The Influence of Small Defects on the Stress Concentration near a Hole

V. A. Levin* and K. M. Zingerman**

Presented by Academician V.P. Myasnikov April 29, 2002

Received May 7, 2002

We discuss the effect of small defects (pores) on the stress concentration near a hole formed in a preliminarily loaded nonlinearly elastic material with finite strains. The shape of the new stress concentrator is assumed to be known at the moment of its formation. We compare two approaches to this problem. The first one is based on the calculation of the stressed–strained state near a hole perforated in the effective medium (also subjected to large initial strains).

The second approach is based on the analysis of local strains in a porous body after the formation of a hole in it. As an example, these local stresses are calculated in the case of the boundary value problem for a body with two closely situated circular holes, one being considerably larger than another in its size. Finally, we consider an important case when a pore turns out to be located at the boundary of the perforated hole and forms a dimple-shaped projection.

In the specific calculations, the mechanical properties of the material are described by the constitutive relations for the Murnaghan potential [1]

$$\overset{0}{\boldsymbol{\Sigma}} = \lambda(\overset{0}{\mathbf{E}} : \mathbf{I})\mathbf{I} + 2G\overset{0}{\mathbf{E}} + 3G_3(\overset{0}{\mathbf{E}} : \mathbf{I})^2\mathbf{I} + C_4(\overset{0}{\mathbf{E}}{}^2 : \mathbf{I})\mathbf{I} + 2C_4(\overset{0}{\mathbf{E}} : \mathbf{I})\overset{0}{\mathbf{E}} + 3C_5\overset{0}{\mathbf{E}}{}^2. \quad (1)$$

In the present paper, all calculations are performed for the following values of constants [2]: $\frac{\lambda}{G} = 2.096$, $\frac{C_3}{G} = -0.07$, $\frac{C_4}{G} = -0.38$, and $\frac{C_5}{G} = 0.34$.

We use the following approach to the construction of the effective constitutive relations [3–5]. We isolate a representative domain in the material (in its undistorted state) containing pores. For this domain, we solve a static problem of nonlinear elasticity theory for fixed stresses at the boundary by the method of successive approximations. We perform averaging of the displacement gradient over this domain and of the true strain tensor over the corresponding domain in the deformed state. Then, we find the Green strain tensor and the second Piola–Kirchhoff stress tensor for the effective material. The effective constitutive relations are constructed as relationships between these tensors. Such calculations are carried out for different kinds of pore arrangements in the representative domain, and then averaging over the ensemble is performed. Furthermore, we perform averaging over various orientations of the coordinate axes [3]. This allows us to write out the effective constitutive relations for the porous material in the form

$$\overset{0}{\boldsymbol{\Sigma}}{}^e = \lambda^e(\overset{0}{\mathbf{E}}{}^e : \mathbf{I})\mathbf{I} + 2G^e\overset{0}{\mathbf{E}}{}^e + 3C_3^e(\overset{0}{\mathbf{E}}{}^e : \mathbf{I})^2\mathbf{I} + C_4^e[(\overset{0}{\mathbf{E}}{}^e)^2 : \mathbf{I}]\mathbf{I} + 2C_6^e(\overset{0}{\mathbf{E}}{}^e : \mathbf{I})\overset{0}{\mathbf{E}}{}^e + 3C_5^e(\overset{0}{\mathbf{E}}{}^e)^2, \quad (2)$$

where superscript e implies that the corresponding parameter is pertinent to the effective material.

The problem of the hole formation is formulated on the basis of the theory of repeatedly superimposed large strains [4, 6] in coordinates related to the intermediate state. It can be posed as follows. In the initial (unstressed) state, the body is free of stresses and strains. Then, under the effect of the initial load applied to the body, large strains are accumulated in it. The body passes into an intermediate state. In the domain occupied by the body, we mentally select a closed surface (or contour in the two-dimensional case). The part of the body bounded by this surface is removed, and its action on the rest of the body is replaced by the forces distributed over this surface (according to the principle of releasing from bonds). Further on, these forces, being now external ones, are quasistatically reduced to zero. In the rest of the body, this causes the formation of additional large (at least, in the vicinity of the newly formed boundary surface) strains and stresses, which are superimposed on the initial ones. The boundary of the body changes, and the body passes into the final state.

* *Moscow State University, Vorob'evy gory, Moscow, 119899 Russia*

** *Tver State University, Sadovyĭ per. 35, Tver, 170000 Russia*

1028-3358/02/4710-0738$22.00

The problem concerning hole formation in the effective medium at a certain fixed porosity is solved in the following way. Effective elastic moduli λ^e, G^e, and C_i^e of the porous material are determined (for a given porosity) according to the procedure described above [3–5] for the case of plane deformation. Then, for the preliminarily loaded infinite body made of the effective material, we solve the static boundary value problem of the nonlinear elasticity theory on the formation of an initially circular hole in this body. The procedure of solving this problem is described in [4] and is based on the method of successive approximations [1, 7]. The linearized problem is solved using the Kolosov–Muskhelishvili method [7, 8]. In our calculations, we used the "Superposition" special-purpose program package for analytical computer calculations [4, 9].

Certain calculation results for the uniaxial initial loading with $q = 0.15G$ are shown in Fig. 1. In this figure, we present the dependence of maximum stress concentration $\frac{\sigma_{\varphi\varphi}}{q}$ on the hole contour on the porosity p in the linear (zeroth approximation) and nonlinear cases. Note that in the linear case, the stress concentration is independent of the porosity and is equal to three. This stems from the well-known property of the solution to the plane problem of linear elasticity for a hole in the infinite body made of the isotropic material. In this case, the stress concentration does not depend on the elasticity moduli of the material and is determined by both the hole shape and type of loading [8]. In the nonlinear case (see Fig. 1), the stress concentration grows slightly with the porosity. Note that both in the linear and nonlinear cases, the maximum stress concentration for values of the porosity, which were used in the calculations, is attained at the same points of the hole. These points lie at the ends of its diameter perpendicular to the direction of the initial loading (in Fig. 1, one of these points, point A, is indicated).

We now discuss the solution to the problem for the body with two closely situated circular holes, one being considerably larger than another. It is assumed that the small hole exists in the infinite-length body before the loading (in the initial state) and that in this state, it has a circular shape. External loads are applied to the body. As a result, the shape of the small hole varies, and the body passes into the intermediate state. In this state, a large hole is formed in the body. The hole acquires a circular shape at the moment of its formation.

We introduce the following notation: x^c_{large}, y^c_{large}, and R_{large} are the coordinates of the center and the radius of the large hole at the moment of its formation. Similarly, x^c_{small}, y^c_{small}, and R_{small} are the coordinates of the center of the small hole and its radius at the moment of its formation. In Fig. 2, the dependences of the maximum stress concentration in the contours of the holes

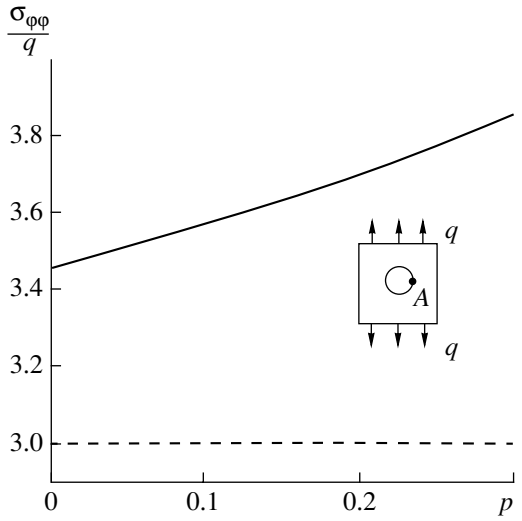

Fig. 1. Maximum stress concentration $\frac{\sigma_{\varphi\varphi}}{q}$ in the hole contour as a function of porosity p in the linear (dashed line) and nonlinear (solid line) cases of the problem on the formation of a hole in the effective medium.

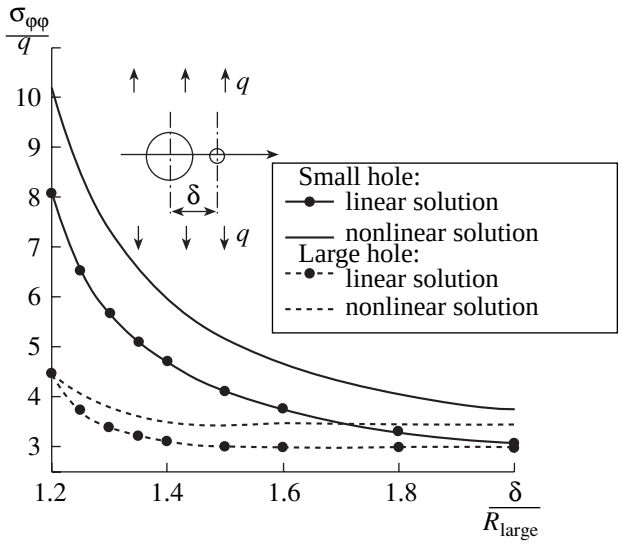

Fig. 2. Maximum stress concentration $\frac{\sigma_{\varphi\varphi}}{q}$ in the contours of holes as a function of the distance δ between their centers in the problem of subsequent formation of small and large holes.

on the distance between the hole centers $\delta = x^c_{\text{small}} - x^c_{\text{large}}$ are given. The case $y^c_{\text{large}} = y^c_{\text{small}} = 0$, $R_{\text{large}} = 10R_{\text{small}}$ at the uniaxial loading $q = 0.15G$ in the direction of the y axis for the linear and nonlinear problems is considered. Comparing the results presented in Figs. 1 and 2, we can see that for $\delta = 1.2R_{\text{large}}$, the stress concentration in the contour of the large hole exceeds by a factor of 1.2–1.5 (depending on the porosity) that in the vicinity of the hole formed in the effective

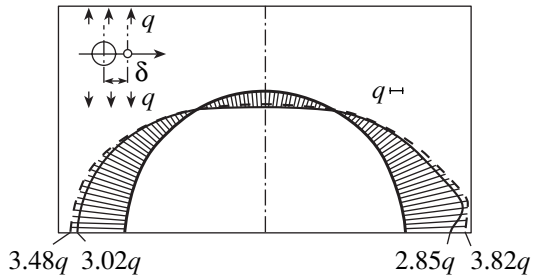

Fig. 3. The distribution diagram for true contour stresses in the contour of a large hole for the case $\delta = 1.25R_{large}$. The linear (solid line) and nonlinear (dashed line) solutions are presented.

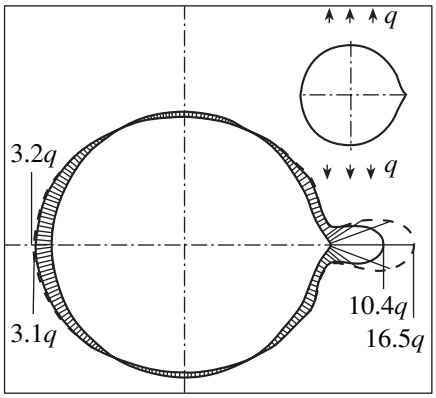

Fig. 4. The distribution diagram for true contour stresses in the contour of a hole in the problem of the hole formation, when the initial hole has circular shape with a hollow-shaped projection. The linear (solid line) and nonlinear (dashed line) solutions are presented.

medium. At the same time, in the contour of the small hole, this factor exceeds two. Note that if the holes are situated sufficiently close to each other ($\delta \le 1.5R_{large}$), the maximum stress concentration in the contour of the large hole is attained, not at a point lying in the x axis (as in the case of the isolated hole), but at a certain distance from this point. The contour stresses at the point of the large hole lying in the x axis turn out to be somewhat lower than in the case without the small hole. As an example, in Fig. 3, we present the distribution diagram for true contour stresses in the contour of the large hole for the case $\delta = 1.25R_{large}$. The thick solid line denotes the contour of the hole, while the thin solid line and dashed line correspond to the linear and nonlinear solutions, respectively. By virtue of symmetry of the problem, only one half of the distribution diagram is shown in Fig. 3. Numbers indicate the values of stress concentration $\frac{\sigma_{\varphi\varphi}}{q}$ at the hole points lying in the x axis for the solutions of the problem corresponding to its linear and nonlinear formulation.

The results of the solution to the problem concerning the formation of the hole in the preliminarily loaded body with the hole having circular shape with a hollow-shaped projection (the large hole absorbs a part of a pore) are illustrated in Fig. 4. In this figure, we present the distribution diagram for true stresses in the hole contour for the solutions to the problem corresponding to its linear and nonlinear formulations. The initial loading is directed along the y axis and has the same value $q = 0.15G$ as in the problem discussed above. The circle center lies on the x axis. The form of the hollow-shaped projection is close to an isosceles triangle with a rounded vertex. The triangle is symmetric with respect to the x axis. The altitude of the triangle is approximately equal to $0.1R$, and its base has a length of $0.4R$, where R is the radius of the circle. The function that performs the conformal mapping of the hole contour onto a unit circle is specified in the form

$$\omega(\xi) = R\left[\xi + \frac{h}{1+h}\xi\frac{1+\rho\xi}{1-\rho\xi}\right],$$

where $h = 0.01$ and $\rho = 1.15$ (in the course of calculations, we performed the Laurent series expansion of this function holding the terms up to ξ^{-15}). This function was constructed following the approach analogous to that discussed in [10].

Numbers in Fig. 4 indicate the values of stress concentration $\frac{\sigma_{\varphi\varphi}}{q}$ at the hole points lying on the x axis while solving the problem in its linear and nonlinear formulations. Comparing the results presented in Fig. 4 and in Fig. 1, we can see that the stress concentration at the hollow apex exceeds that about the circular hole in the effective medium by factors greater than three and four in the linear and nonlinear cases, respectively.

Thus, calculating stress concentration near a hole formed in the porous medium under finite strains, we can see variations of the results if we replace it with the homogeneous effective material. In this case, the calculated maximum stress concentration can be much lower than that calculated with a due account of local stresses related to the inhomogeneity of the material (by a factor of 1.5–4 for the problems considered here).

ACKNOWLEDGMENTS

The work was supported by the program "Universities of Russia," project no. 990858.

REFERENCES

1. A. I. Lur'e, *Nonlinear Theory of Elasticity* (Nauka, Moscow, 1980; Elsevier, London, 1990).
2. A. N. Guz', F. G. Makhort, and O. I. Gushcha, *Introduction to the Acoustoelasticity* (Naukova Dumka, Kiev, 1973).

3. V. A. Levin, V. V. Lokhin, and K. M. Zingerman, Izv. Akad. Nauk, Mekh. Tverd. Tela, No. 4, 45 (1997).
4. V. A. Levin, *Multiple Superposition of Large Deformations in Elastic and Viscoelastic Bodies* (Nauka, Moscow, 1999).
5. V. A. Levin and K. M. Zingerman, Dokl. Akad. Nauk **382**, 482 (2002) [Dokl. Phys. **47**, 136 (2002)].
6. V. A. Levin and G. S. Taras'ev, Dokl. Akad. Nauk **251**, 63 (1980) [Sov. Phys. Dokl. **25**, 215 (1980)].
7. G. N. Savin, *Distribution of Stresses Near Holes* (Naukova Dumka, Kiev, 1968).
8. N. I. Muskhelishvili, *Some Basic Problems in Mathematical Elasticity Theory: Fundamental Equations, Plane Theory of Elasticity, Torsion, and Bending* (Nauka, Moscow, 1966; Groningen, P. Noordhoff, 1963).
9. K. M. Zingerman and V. A. Levin, Izv. Akad. Nauk, Mekh. Tverd. Tela, No. 4, 162 (1999).
10. M. A. Lavrent'ev and B. V. Shabat, *Methods of Theory of Complex-Variable Functions* (Nauka, Moscow, 1987).

Translated by K. Kugel'

Doklady Physics, Vol. 47, No. 10, 2002, pp. 742–746. Translated from Doklady Akademii Nauk, Vol. 386, No. 4, 2002, pp. 482–486.

MECHANICS

Modification of the Method of Invariant Normalization of Hamiltonians by Parameterizing Canonical Transformations

A. G. Petrov

Presented by Academician D.M. Klimov April 16, 2002

Received April 17, 2002

Hamiltonian mechanics involves two constructive methods of constructing canonical changes: the generating function method and generator method.

In this paper, a new independent method of constructing canonical changes in the parametric form is proposed. A criterion of existence for a parametric representation of a canonical change of variables is formulated, and the law of Hamiltonian transformation is obtained. This method is applied to find the normal form of Hamiltonians, which is defined in [1, 2]. This choice of the definition of the normal form is convenient, because it ensures a unified approach for autonomous and nonautonomous cases as well as for resonant and nonresonant cases.

For asymptotics of the normal form, a set of equations similar to the equations obtained in [1, 2] is derived. A parameterized generating function, which is used instead of the method of a generator and generating Hamiltonian, enables us to derive the set of equations immediately for nonautonomous Hamiltonians in contrast to [1, 2], where the previous reduction to the autonomous form was required.

The method is applicable to Hamiltonian systems in both classical mechanics and hydrodynamics (motion of particles of a viscid incompressible fluid in a layer with a periodically varying boundary).

1. PARAMETRIC FORM OF CANONICAL TRANSFORMATIONS

The general result of parameterizing the canonical change of variables in Hamiltonian systems is formulated as a theorem.

Institute for Problems in Mechanics, Russian Academy of Sciences, pr. Vernadskogo 101, Moscow, 117526 Russia

Theorem 1. *Let*

$$\begin{aligned} \mathbf{q} &= \mathbf{x} - \frac{1}{2}\Psi_{\mathbf{y}}, \\ \mathbf{p} &= \mathbf{y} + \frac{1}{2}\Psi_{\mathbf{x}}, \\ \mathbf{Q} &= \mathbf{x} + \frac{1}{2}\Psi_{\mathbf{y}}, \\ \mathbf{P} &= \mathbf{y} - \frac{1}{2}\Psi_{\mathbf{x}} \end{aligned} \tag{1}$$

be the parametric form of the variable transformation $\mathbf{q}, \mathbf{p} \longrightarrow \mathbf{Q}, \mathbf{P}$. *Then, for any function* $\Psi(t, \mathbf{x}, \mathbf{y})$,

(i) *Jacobians of two transformations* $\mathbf{q} = \mathbf{q}(t, \mathbf{x}, \mathbf{y})$, $\mathbf{p} = \mathbf{p}(t, \mathbf{x}, \mathbf{y})$ *and* $\mathbf{Q} = \mathbf{Q}(t, \mathbf{x}, \mathbf{y})$, $\mathbf{P} = \mathbf{P}(t, \mathbf{x}, \mathbf{y})$ *are identical*:

$$\frac{\partial(\mathbf{q}, \mathbf{p})}{\partial(\mathbf{x}, \mathbf{y})} = \frac{\partial(\mathbf{Q}, \mathbf{P})}{\partial(\mathbf{x}, \mathbf{y})} = J(t, \mathbf{x}, \mathbf{y}); \tag{2}$$

(ii) *in the region* $J > 0$, *the transformation of variables* $\mathbf{q}, \mathbf{p} \longrightarrow \mathbf{Q}, \mathbf{P}$ *specified by Eqs.* (1) *transforms the Hamiltonian system* $H = H(t, \mathbf{q}, \mathbf{p})$ *into the Hamiltonian system* $\tilde{H} = \tilde{H}(t, \mathbf{Q}, \mathbf{P})$ *as*

$$\Psi_t(t, \mathbf{x}, \mathbf{y}) + H(t, \mathbf{q}, \mathbf{p}) = \tilde{H}(t, \mathbf{Q}, \mathbf{P}), \tag{3}$$

where $\mathbf{q}$, $\mathbf{p}$, $\mathbf{Q}$, *and* $\mathbf{P}$ *in the Hamiltonians* H *and* $\tilde{H}$ *are expressed in terms of* $\mathbf{x}$ *and* $\mathbf{y}$ *through Eqs.* (1).

Statement (ii) is proven by using the criterion of canonicity, according to which the differential form $\delta F = \mathbf{P}\delta\mathbf{Q} - \mathbf{p}\delta\mathbf{q} - (\tilde{H} - H)\delta t$ is the total differential of a certain function $\delta F(t, \mathbf{x}, \mathbf{y}) = F_t\delta t + F_{\mathbf{x}}\delta\mathbf{x} + F_{\mathbf{y}}\delta\mathbf{y}$ [1].

Substituting Eqs. (1) into the differential form δF, replacing $\tilde{H} - H$ by Ψ_t according to Eq. (3), and performing obvious manipulations, we obtain $\delta F = \delta(\mathbf{y}\Psi_{\mathbf{y}} - \Psi)$ Q.E.D.

Statement (i) follows from the fact that the Jacobian of the superposition of mappings is equal to the product of Jacobians of these mappings. Moreover, the Jacobian

1028-3358/02/4710-0742$22.00

of the canonical transformation $\mathbf{q}, \mathbf{p} \longrightarrow \mathbf{Q}, \mathbf{P}$ is equal to unity. Therefore,

$$1 = \frac{\partial(\mathbf{P}, \mathbf{Q})}{\partial(\mathbf{p}, \mathbf{q})} = \frac{\partial(\mathbf{P}, \mathbf{Q})}{\partial(\mathbf{x}, \mathbf{y})}\left(\frac{\partial(\mathbf{p}, \mathbf{q})}{\partial(\mathbf{x}, \mathbf{y})}\right)^{-1},$$

and Eq. (2) has been proven.

Let us study for which canonical transformations the parametrization exists.

2. GENERATING FUNCTIONS

The canonical transformation can be expressed in terms of the generating functions $S_1(t, \mathbf{q}, \mathbf{P})$ and $S_2(t, \mathbf{p}, \mathbf{Q})$ as

$$dS_1 = \mathbf{p}d\mathbf{q} + \mathbf{Q}d\mathbf{P} + (\tilde{H} - H)dt, \quad \det S_{1\mathbf{qP}} \neq 0,$$

$$dS_2 = -\mathbf{q}d\mathbf{p} - \mathbf{P}d\mathbf{Q} + (\tilde{H} - H)dt, \quad \det S_{2\mathbf{qQ}} \neq 0.$$

Let us introduce the new generating function

$$\Phi = \frac{1}{2}[S_1(t, \mathbf{q}, \mathbf{P}) - \mathbf{qP} + S_2(t, \mathbf{Q}, \mathbf{p}) + \mathbf{Qp}]. \quad (4)$$

Its differential form is

$$d\Phi = \frac{1}{2}\sum_{i=1}^{n}\begin{vmatrix} Q_i - q_i & P_i - p_i \\ dQ_i + dq_i & dP_i + dp_i \end{vmatrix} + (\tilde{H} - H)dt. \quad (5)$$

The differential form $d\Phi$ for $dt = 0$ was introduced in [3], where it was shown that, if $\mathbf{Q}(\mathbf{q}, \mathbf{p})$, $\mathbf{P}(\mathbf{q}, \mathbf{p})$ is a canonical transformation, $d\Phi$ is the total differential, and the function $\Phi(\mathbf{q}, \mathbf{p})$ exists. Solving Eqs. (1) with respect to $\mathbf{x}$, $\mathbf{y}$ and $\Psi_\mathbf{y}$, $\Psi_\mathbf{x}$, we obtain

$$\mathbf{x} = \frac{1}{2}(\mathbf{q} + \mathbf{Q}), \quad \mathbf{y} = \frac{1}{2}(\mathbf{p} + \mathbf{P}),$$
$$\Psi_\mathbf{y} = \mathbf{Q} - \mathbf{q}, \quad \Psi_\mathbf{x} = -\mathbf{P} + \mathbf{p}, \quad (6)$$

which, if the Jacobian of change (6) is nonzero, i.e., $\frac{\partial(\mathbf{x}, \mathbf{y})}{\partial(\mathbf{q}, \mathbf{p})} \neq 0$, leads to the equality $d\Phi = d\Psi$ and

$$\Psi(\mathbf{x}, \mathbf{y}) = \Psi\left(\frac{\mathbf{q} + \mathbf{Q}(\mathbf{q}, \mathbf{p})}{2}, \frac{\mathbf{p} + \mathbf{P}(\mathbf{q}, \mathbf{p})}{2}\right) = \Phi(\mathbf{q}, \mathbf{p}).$$

It follows from Eqs. (2) and (6) that $\frac{\partial(\mathbf{x}, \mathbf{y})}{\partial(\mathbf{q}, \mathbf{p})} = \frac{1}{J} = 2^{-2n}\det(E + A)$, where E is the identity matrix and $A = \frac{\partial(\mathbf{Q}, \mathbf{P})}{\partial(\mathbf{q}, \mathbf{p})}$ is the Jacobian matrix. Therefore, the condition that change (6) is not degenerate has the form $\det(E + A) \neq 0$.

The result is formulated as follows.

Theorem 2. *If the transformation* $\mathbf{Q}(\mathbf{q}, \mathbf{p})$, $\mathbf{P}(\mathbf{q}, \mathbf{p})$ *is canonical in the region* $(\mathbf{q}, \mathbf{p}) \in \Omega$ *and eigenvalues of the Jacobian matrix A differ from* –1, *parameterization* (1) *exists in* Ω.

3. INVARIANT NORMALIZATION OF HAMILTONIANS

The normal form of the Hamiltonian in a Hamiltonian system is called normal Birkhoff form [4], whose briefest definition was given in [5]. In all cases, the generated Hamiltonian is taken in the simplest quadratic form for a linear oscillating system, and the definition of the normal form is associated with the choice of the generated Hamiltonian and is noninvariant. Two methods of constructing canonical changes transforming the system to the normal form are most extensively used. The first method is based on generating functions and goes back to Birkhoff [4]. In the second method, Lee generators are used instead of generating functions. The second method is more convenient, because, in contrast to the first method, it does not involve the inversion of power series.

For the perturbed Hamiltonian

$$H(t, \mathbf{q}, \mathbf{p}) = H_0(t, \mathbf{q}, \mathbf{p}) + \varepsilon H_*(t, \mathbf{q}, \mathbf{p}).$$

Zhuravlev [1, 2] proposed the general criterion of the normal form: *The perturbed Hamiltonian has the normal form if and only if the perturbation is the first integral of the unperturbed part*; *i.e.*, $\frac{\partial H_*}{\partial t} + \{H_0, H_*\} = 0$, *where* $\{f, q\} = f_\mathbf{p}g_\mathbf{q} - f_\mathbf{q}g_\mathbf{p}$ *is the Poisson bracket*. Since the criterion is invariant, normalization does not require the preliminary simplification of the unperturbed part and separation of autonomous–nonautonomous and resonant–nonresonant cases. Moreover, the normal form defined in [1, 2] has an important property that simplifies the construction of a solution and is formulated as a theorem [2].

Zhuravlev's theorem. *If a system with the Hamiltonian H satisfies the condition of the normal form, for constructing the general solution to the corresponding Hamilton equation, it is sufficient*

(i) *to find the general solution to the generating system with the Hamiltonian* $H_0(t, p, q)$; *and*

(ii) *to find the general solution determined only by the perturbation* $\varepsilon H_*(0, p, q)$ *for zero time*.

In this case, the general solution to the original nonautonomous system is represented as the composition of the solutions in arbitrary order (*solutions to the first system are substituted for arbitrary constants in the solution to the second system and vice versa*).

Let us demonstrate that Theorem 1 reasonably leads to an analog of the normalization method [1, 2].

Let the Hamiltonian $H(t, \mathbf{q}, \mathbf{p}) = H_0(t, \mathbf{q}, \mathbf{p}) + \varepsilon H_*(t, \mathbf{q}, \mathbf{p})$ must be transformed to the normal form $\bar{H}(t, \mathbf{Q}, \mathbf{P})$, and $H_0 + \varepsilon\bar{H}_{*k-1}$ be the kth order asymptotic of the normal form $\bar{H}(t, \mathbf{Q}, \mathbf{P}) = H_0(t, \mathbf{Q}, \mathbf{P}) + \varepsilon\bar{H}_{*k-1}(t, \mathbf{Q}, \mathbf{P}) + O(\varepsilon^{k+1})$ with canonical change (1).

Table

This algorithm	Algorithm [1, 2]
Original system $H(t, \mathbf{q}, \mathbf{p})$ is nonautonomous	System $H(\mathbf{q}, \mathbf{p})$ is autonomous, original system reduces to a autonomous system with increasing order
Function $\psi(t, \varepsilon, \mathbf{x}, \mathbf{y})$	Generating Hamiltonian $G(\varepsilon, \mathbf{Q}, \mathbf{P})$
Canonical change $(\mathbf{q}, \mathbf{p}) \Rightarrow (\mathbf{Q}, \mathbf{P})$ in parametric form (1)	Canonical change $\frac{d\mathbf{Q}}{d\varepsilon} = \frac{\partial G}{\partial \mathbf{P}}, \frac{\partial \mathbf{P}}{\partial \varepsilon} = -\frac{\partial G}{\partial \mathbf{Q}}$, $\mathbf{Q}(0) = \mathbf{q}, \mathbf{P}(0) = \mathbf{p}$

According to Theorem 1, we arrive at Eq. (3), which reduces to the form

$$\frac{\partial \Psi}{\partial t} + H_0\left(t, \mathbf{x} - \frac{1}{2}\Psi_{\mathbf{y}}, \mathbf{y} + \frac{1}{2}\Psi_{\mathbf{x}}\right) - H_0\left(t, \mathbf{x} + \frac{1}{2}\Psi_{\mathbf{y}}, \mathbf{y} - \frac{1}{2}\Psi_{\mathbf{x}}\right) + \varepsilon H_{*k-1}\left(t, \mathbf{x} - \frac{1}{2}\Psi_{\mathbf{y}}, \mathbf{y} + \frac{1}{2}\Psi_{\mathbf{x}}\right) = \varepsilon \bar{H}_{*k-1}\left(t, \mathbf{x} + \frac{1}{2}\Psi_{\mathbf{y}}, \mathbf{y} - \frac{1}{2}\Psi_{\mathbf{x}}\right) + O(\varepsilon^{k+1}), \quad (7)$$

where the asymptotics

$$\Psi = \varepsilon\Psi_{k-1} + O(\varepsilon^{k+1}), \quad H_* = H_{*k-1} + O(\varepsilon^k)$$

are introduced according to the method [1, 2]. Equation (7) leads to the following chain of equations for determining the asymptotics of canonical changes Ψ_{k-1} and normalized Hamiltonians $H_0 + \varepsilon\bar{H}_{*k-1}$:

$$\varepsilon\left(\frac{\partial \Psi_{k+1}}{\partial t} + \{H_0, \Psi_{k-1}\}\right) + R_k = \varepsilon \bar{H}_{*k-1}, \quad \frac{\partial \bar{H}_{*k-1}}{\partial t} + \{H_0, \bar{H}_{*k-1}\} = 0, \quad k = 1, 2, \ldots . \quad (8)$$

Here, R_k are sequentially calculated by the formulas

$$R_1 = \varepsilon H_{*0}, \quad R_2 = \varepsilon H_{*1} + \frac{1}{2}\varepsilon^2\{H_{*0} + \bar{H}_{*0}, \Psi_0\}, \ldots . \quad (9)$$

It is easy to derive the general formula for the representation of R_k in terms of the calculated lower asymptotics of Ψ and $\bar{H}$. When H_0 is a polynomial whose power in $\mathbf{p}$ and $\mathbf{q}$ is no more than 2, Eq. (7) simplifies to

$$\frac{\partial \Psi}{\partial t} + \{H_0, \Psi\} + \varepsilon H_{*k-1}\left(t, \mathbf{x} - \frac{1}{2}\Psi_{\mathbf{y}}, \mathbf{y} + \frac{1}{2}\Psi_{\mathbf{x}}\right) = \varepsilon \bar{H}_{*k-1}\left(t, \mathbf{x} + \frac{1}{2}\Psi_{\mathbf{y}}, \mathbf{y} - \frac{1}{2}\Psi_{\mathbf{x}}\right), \quad (10)$$

and R_k is the kth order asymptotic of the expression

$$\varepsilon\left[H_*\left(t, \mathbf{x} - \frac{1}{2}\Psi_{\mathbf{y}}, \mathbf{y} + \frac{1}{2}\Psi_{\mathbf{x}}\right) - \bar{H}_{*k-1}\left(t, \mathbf{x} + \frac{1}{2}\Psi_{\mathbf{y}}, \mathbf{y} - \frac{1}{2}\Psi_{\mathbf{x}}\right) + \bar{H}_{*k-1}(t, \mathbf{x}, \mathbf{y})\right].$$

The chain of Eqs. (8) was derived in [1, 2], where these equations were called homological and written in the form

$$\varepsilon\frac{d\Psi_{k-1}}{dt} + R_k = \varepsilon\bar{H}_{*k-1}, \quad \frac{d\bar{H}_{*k-1}}{dt} = 0, \quad k = 1, 2, \ldots, \quad (11)$$

where the total derivative is calculated for the solution $\mathbf{x}(t, \mathbf{x}_0, \mathbf{y}_0)$, $\mathbf{y}(t, \mathbf{x}_0, \mathbf{y}_0)$ of the unperturbed system. The following quadrature of Eq. (11), which was found in [1, 2]

$$\varepsilon[\Psi_{k-1}(t, \mathbf{x}, \mathbf{y}) - \Psi_{k-1}(0, \mathbf{x}_0, \mathbf{y}_0)] + \int_0^t R_k(t, \mathbf{x}, \mathbf{y})dt = t\varepsilon\bar{H}_{*k-1}(0, \mathbf{x}_0, \mathbf{y}_0),$$

provides the key to solving the problem of normalizing the Hamiltonian. In particular, the asymptotic of the normal form is equal to $\bar{H} = H_0 + \langle R_k\rangle + O(\varepsilon^{k+1})$.

Table 1 compares the above algorithm with the algorithm proposed in [1, 2].

Relation of the generating Hamiltonian G to the function Ψ. In the method proposed in [1, 2], the change $\mathbf{q}, \mathbf{p} \longrightarrow \mathbf{Q}, \mathbf{P}$ is sought on the phase flux of the Hamiltonian system

$$\frac{d\mathbf{X}}{d\tau} = G_Y, \quad \frac{d\mathbf{Y}}{d\tau} = -G_{\mathbf{X}}. \quad (12)$$

At the initial time $\tau = 0$, $\mathbf{X}(0) = \mathbf{q}$, $\mathbf{Y}(0) = \mathbf{p}$; at the time $\tau = \varepsilon$, $\mathbf{X}(\varepsilon) = \mathbf{Q}$, $\mathbf{Y}(\varepsilon) = \mathbf{P}$, where the auxiliary parameter τ in the interval $0 \le \tau \le \varepsilon$ is the analog of time t.

The same change in the present algorithm is realized by parameterization. The function Ψ specifying the mapping on the phase flux of Hamiltonian system (12) is determined from the equation

$$\Psi_\tau(\tau, \mathbf{x}, \mathbf{y}) = G\left(\mathbf{x} + \frac{1}{2}\Psi_{\mathbf{y}}, \mathbf{y} - \frac{1}{2}\Psi_{\mathbf{x}}\right), \quad \Psi(0, \mathbf{x}, \mathbf{y}) = 0.$$

Up to the terms $\tau^3 = \varepsilon^3$, $\Psi = \varepsilon G$. For this reason, the asymptotics of the first two approximations coincide in both methods; i.e., $\Psi_0 = G_0$ and $\Psi_1 = G_1$, and R_1 and R_2 are also identical in both methods. Higher approximations for R_3, R_4, … are different. The normal form as a whole is independent of the method choice.

The very instructive examples in [1, 2] demonstrate substantial simplifications as compared to all methods known previously. This method is as simple as the method [1, 2], but different in that the chain of equations for asymptotics is written in the original Hamiltonian system whether it be autonomous or nonautonomous. In method [1, 2], a nonautonomous system should be reduced to the autonomous system with increasing order, and then the chain of equations for asymptotics is written. Let us apply the method to two systems. Both examples concern forced resonance oscillations. These systems have no classical normal form [3]. In this case, another definition of the normal form must be introduced [5], which is not necessary for the normal form defined in [1, 2], because it exists in the resonant case as well. Let us show how it is defined and how a solution is found.

Example 1. Forced oscillations of the linear oscillator described by the Hamiltonian $H = H_0 + \varepsilon H_*$, where $H_0 = \frac{1}{2}(q^2 + p^2)$ and $H_* = -q\sin t$. The equation of the form $\ddot{q} + q = \varepsilon\sin t$ has the exact solution $q = \left(q_0 - \frac{t\varepsilon}{2}\right)\cos t + \left(p_0 + \frac{\varepsilon}{2}\right)\sin t$. The solution is obtained by the normal form method as follows.

(i) The solution to the unperturbed system is found in the form

$$q = q_0\cos t + p_0\sin t, \quad p = -q_0\sin t + p_0\cos t.$$

(ii) The function $R_1(t, q_0, p_0) = -\varepsilon(q_0\cos t + p_0\sin t)\sin t$ is obtained, and the integral

$$\int R_1 dt = -\frac{\varepsilon}{2}p_0 t + \frac{\varepsilon}{4}(q_0\cos 2t + p_0\sin 2t)$$

is calculated.

(iii) The linear part presents the normal form. To construct the solution according to the Zhuravlev theorem, it is sufficient to know the Hamiltonian $\bar{H}_*(0, Q, P) = -\frac{1}{2}P$, which corresponds to the equations $\dot{Q} = -\frac{1}{2}\varepsilon$, $\dot{P} = 0$ having the solution $Q = Q_0 - \frac{\varepsilon t}{2}$, $P = P_0$. According to the Zhuravlev theorem, the total solution is obtained in the form $Q = \left(Q_0 - \frac{\varepsilon t}{2}\right)\cos t + P_0\sin t$, $P = -\left(Q_0 - \frac{\varepsilon t}{2}\right)\sin t + P_0\cos t$.

(iv) The integrand in (ii), which is limited in time, determines the parametric-change function Ψ. Expressing q_0 and p_0 in terms of the variables q and p and changing them to the parameters x and y, we find $\Psi = -\frac{1}{4}\varepsilon(x\cos t + y\sin t)$. Excluding parameters x and y in the parametric change, we obtain $q = Q + \frac{1}{4}\varepsilon\sin t$ and $p = P - \frac{1}{4}\varepsilon\cos t$ and find the exact solution to the original system.

Example 2. Forced oscillations of the Duffing nonlinear oscillator described by the equation $\ddot{q} + \omega^2 q = \varepsilon(-q^3 + \sin t)$. It is required to find the amplitude–frequency characteristic $\omega(A)$ for which the periodic solution exists. This problem was solved in [1, 6] by the averaging method. For comparison, we present the solution by the normal-form method.

The frequency is sought in the form $\omega = 1 - \varepsilon\lambda$. Up to ε^2, the Hamiltonian of the system is written as $H = H_0 + \varepsilon H_*$, where $H_0 = \frac{1}{2}(q^2 + p^2)$ and $H_* = -\lambda p^2 + \frac{q^4}{4} - q\sin t$. Then, the manipulations of the above example are repeated.

(i) The solution to the unperturbed system is the same as in example 1.

(ii) We find the function

$$R_1(t, q_0, p_0) = \varepsilon\Big[-(q_0\cos t + p_0\sin t)\sin t - \lambda(-q_0\sin t + p_0\cos t)^2 + \frac{1}{4}(q_0\cos t + p_0\sin t)^4\Big].$$

(iii) The part of the integral of R_1 that is linear in t is calculated and determines the normal form $\bar{H} = \frac{1}{2}(Q^2 + P^2) + \varepsilon\bar{H}_*$, where

$$\bar{H}_* = -\frac{1}{2}P - \frac{\lambda}{2}(Q^2 + P^2) + \frac{3}{32}(Q^2 + P^2)^2.$$

From the set of equations

$$\frac{\partial\bar{H}_*}{\partial Q} = \left(-\lambda + \frac{3}{8}A^2\right)Q = 0,$$

$$\frac{\partial\bar{H}_*}{\partial P} = \left(-\lambda + \frac{3}{8}A^2\right)P - \frac{1}{2} = 0$$

we find the stationary point $Q = 0$, $P = \pm A$ and the desired frequency $\lambda = \frac{3}{8}A^2 \pm \frac{1}{2A}$ as a function of the amplitude $A = \sqrt{Q^2 + P^2}$. According to the Zhuravlev theorem and the second Bogolyubov theorem [6], this

stationary point determines the periodic solution to the original nonlinear system. Stability corresponds to the minimum of the function $\bar{H}_*(Q, P)$ at the stationary point. Therefore, the condition of the stability of the periodic solution has the form

$$\frac{\partial^2 H_*}{\partial q^2}\frac{\partial^2 H_*}{\partial p^2} - \left(\frac{\partial^2 H_*}{\partial q \partial p}\right)^2 = \left(-\lambda + \frac{3}{8}A^2\right)\left(-\lambda + \frac{9}{8}A^2\right) > 0,$$

which agrees with the similar condition obtained by the averaging method.

(iv) If necessary, the residue of the part of the integral of R_1 that is linear in time can be calculated, and the function Ψ determining the canonical change can be found. Then, the solution in the original variables can be found.

The application of the parameterization method to the construction of Poincaré mappings and to new problems of classical mechanics and hydrodynamics was exemplified in [7–10].

ACKNOWLEDGMENTS

I am grateful to D.M. Klimov for his interest in the study and to V.F. Zhuravlev for stimulating discussions and remarks.

This work was supported in part by the Russian Foundation for Basic Research, project no. 02-01-00567.

REFERENCES

1. V. F. Zhuravlev, *Foundations of Theoretical Mechanics* (Nauka, Moscow, 1997).
2. V. F. Zhuravlev, Prikl. Mat. Mekh. **66** (3) (2002).
3. V. I. Arnold, *Mathematical Methods of Classical Mechanics* (Editorial URSS, Moscow, 2000; Springer, New York, 1989).
4. G. D. Birkhoff, *Dynamical Systems* (Am. Math. Soc., New York, 1927; Gostekhizdat, Moscow–Leningrad, 1941).
5. A. D. Bryuno, *Restricted Problem of Three Bodies* (Nauka, Moscow, 1990).
6. N. N. Bogolyubov and Yu. A. Mitropol'skiĭ, *Asymptotic Methods in the Theory of Nonlinear Oscillations* (Nauka, Moscow, 1974; Gordon and Breach, New York, 1962).
7. A. G. Petrov, Dokl. Akad. Nauk **368** (4), 483 (1999) [Dokl. Phys. **44**, 698 (1999)].
8. A. G. Petrov, Izv. Akad. Nauk, Ser. Mekh. Zhidk. Gaza, No. 4, 12 (2000).
9. A. G. Petrov, Izv. Akad. Nauk, Mekh. Tverd. Tela, No. 3, 19 (2001).
10. A. G. Petrov, Dokl. Akad. Nauk **382** (1), 15 (2002).

Translated by R. Tyapaev

Doklady Physics, Vol. 47, No. 10, 2002, pp. 747–749. Translated from Doklady Akademii Nauk, Vol. 386, No. 4, 2002, pp. 487–489.

MECHANICS

On the Theory of the Propagation of Elastoplastic Waves through Loose Materials

V. M. Sadovskiĭ

Presented by Academician V.P. Myasnikov June 25, 2002

Received May 31, 2002

The elastic properties of ideal loose media are described by the elasticity-theory models of materials with different moduli and convex stress potential W, which is equal to zero on a certain cone C in the space of strain tensors [1–3]. In accordance with Hooke's law

$$\sigma = \frac{\partial W}{\partial \varepsilon^e}, \tag{1}$$

the stresses corresponding to strains from this cone are also equal to zero. Therefore, for $\varepsilon^e \in C$, the medium loses its bearing capacity.

The dual deformation potential can be found by the Young transformation and has the form

$$W^* = \begin{cases} W_0^*(\sigma), & \text{if } \sigma \in C^* \\ +\infty, & \text{if } \sigma \notin C^*. \end{cases}$$

Here, W_0^* is the regular part of the potential and $C^* = \{\sigma |\ \sigma : \varepsilon^e \le 0 \quad \forall \varepsilon^e \in C\}$ is the conjugate cone. The inclusion $\varepsilon^e \in \partial W^*(\sigma)$ represents the inverted form of Eq. (1), where ∂ is the subdifferential.

For small deformations, W_0^* can be approximated by a quadratic function. In this case, the Haar–Karman inequality is valid [4]:

$$(\bar{\sigma} - \sigma) : (a : \sigma - \varepsilon^e) \ge 0, \quad \sigma, \bar{\sigma} \in C^*, \tag{2}$$

where a is the fourth-rank tensor of the elastic compliance moduli. The solution to inequality (2) is the projection $\sigma = s^\pi$ of the conditional-stress tensor s, which is determined from the equation $a : s = \varepsilon^e$, onto the cone C^* in terms of the Euclidean norm $|\sigma| = \sqrt{\sigma : a : \sigma}$.

The plastic properties of the medium are described by the inclusion $\sigma \in \partial\varphi(\dot{\varepsilon}^p)$, where φ is the convex dissipative potential of stresses. Since the plastic deformation is independent of the time scale, φ is a homogeneous linear function [5]. Therefore, the dual potential of the plastic-deformation rates, $\varphi^*(\sigma)$, is equal to the indicator function of the set $F = \{\sigma |\ \sigma : \dot{\varepsilon}^p \le \varphi(\dot{\varepsilon}^p) \quad \forall \dot{\varepsilon}^p\}$:

$$\varphi^* = \begin{cases} 0, & \text{if } \sigma \in F \\ +\infty, & \text{if } \sigma \notin F. \end{cases}$$

The dual formulation of the plastic-flow law $\dot{\varepsilon}^p \in \partial\varphi^*(\sigma)$ leads to the von Mises inequality

$$(\bar{\sigma} - \sigma) : \dot{\varepsilon}^p \le 0, \quad \sigma, \bar{\sigma} \in F. \tag{3}$$

Inequalities (2) and (3), along with the equations of motion and the kinematic relations

$$\rho \dot{v} = \nabla \cdot \sigma, \quad 2(\dot{\varepsilon}^e + \dot{\varepsilon}^p) = \nabla \boldsymbol{v} + (\nabla \boldsymbol{v})^* \tag{4}$$

form a closed model describing the dynamics of a loose medium. In this model, we consider the class of generalized solutions with a strong discontinuity.

Let U be a vector function composed of the velocity components v and the tensor of conditional stresses s with respect to the Cartesian coordinate system. In terms of U, the model specified by Eqs. (2)–(4) is transformed to the variational inequality

$$(\bar{U} - U^\pi)\left(A\dot{U} - \sum_{k=1}^{n} B^k U^\pi_{,k}\right) \ge 0, \quad U^\pi, \bar{U} \in F, \tag{5}$$

where A and B^k are symmetric matrices (A is positive definite). Taking into account the identity $U^\pi A \dot{U} = U^\pi A \dot{U}^\pi$ following from the definition of a projection on a cone, inequality (5) can be reduced to a divergent inequality. Using its integral generalization and passing to

Institute of Computational Modeling, Siberian Division, Russian Academy of Sciences, Akademgorodok, Krasnoyarsk, 660036 Russia

1028-3358/02/4710-0747$22.00

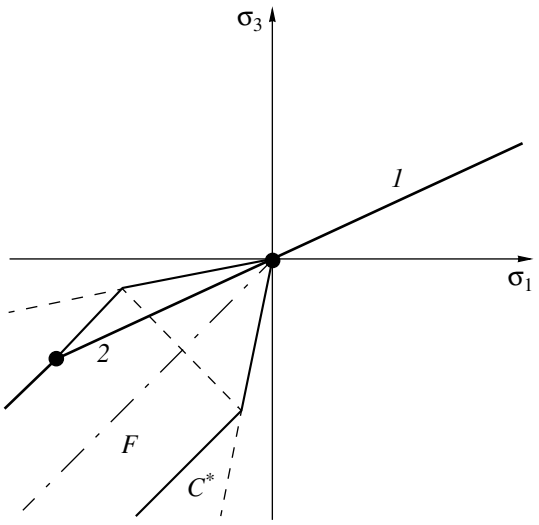

Fig. 1. Stress trajectories in the cases of (*1*) tension and (*2*) compression.

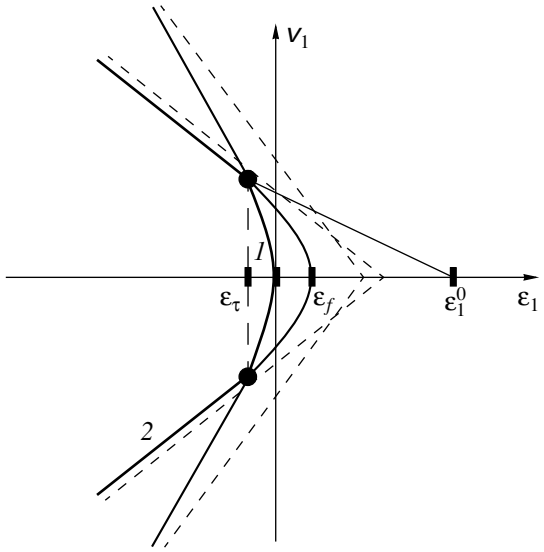

Fig. 2. Shock adiabats of (*1*) elastic and (*2*) plastic signotons.

the limit [6], we find the strong-discontinuity relations

$$(\bar{U} - \langle U^{\pi}\rangle)\left(cA[U] + \sum_{k=1}^{n} \nu_k B^k[U^{\pi}]\right) + c\langle U^{\pi}\rangle A[U - U^{\pi}] \geq 0, \quad U^{\pi}, \bar{U} \in F. \tag{6}$$

Here, $[U]$ is the jump, $\langle U\rangle$ is the average value of the vector-function U on the discontinuity surface, and $c > 0$ is the velocity of the front in the direction of the normal vector $\boldsymbol{\nu}$.

When the deformation of a medium is three-dimensional, it is laborious to classify discontinuous solutions on the basis of inequality (6). We consider only signotons, i.e., plane longitudinal shock waves, in which the strain of an element changes sign. Let the medium in the neighborhood of the uniform-compression state be isotropic and obey the linear Hooke's law, and let the cone C^* and set F be approximated by the von Mises–Schleicher cone and von Mises cylinder, respectively. Then, in the space of principal stresses, the trajectories of uniaxial deformation $\sigma(\varepsilon_1)$ and $s(\varepsilon_1)$ are represented by a broken line on the plane $\sigma_2 = \sigma_3$ (Fig. 1). If the coefficient of internal friction κ lies in the range

$$\frac{2\mu}{\sqrt{3}k} \leq \kappa \leq \frac{\sqrt{3}}{2},$$

where μ and k are the shear modulus and bulk modulus, respectively, the stresses σ_1 and σ_3 in the case of tension are equal to zero:

$$s_1 = \left(k + \frac{4\mu}{3}\right)\varepsilon_1, \quad s_3 = \left(k - \frac{2\mu}{3}\right)\varepsilon_1. \tag{7}$$

In the case of compression, the medium is either in elastic state (7) with $\sigma = s$ or in the plastic state (τ is the shear yield point):

$$\sigma_1 = s_1 = -\frac{2\tau}{\sqrt{3}} + k\varepsilon_1, \quad \sigma_3 = s_3 = \frac{\tau}{\sqrt{3}} + k\varepsilon_1. \tag{8}$$

The limiting elastic compressive strain is equal to $\varepsilon_\tau = -\frac{\sqrt{3}\tau}{2\mu}$.

If the coefficient κ is outside the above range, this model indicates that a medium exhibiting elastic and plastic properties can resist uniaxial tension or can be loosened under compression. Below, such variants of the model are not considered.

Using Eqs. (6)–(8), we construct the following shock adiabats of elastic and plastic signotons (Fig. 2):

$$\left(\frac{v_1 - v_1^0}{c_p}\right)^2 = \varepsilon_1(\varepsilon_1 - \varepsilon_1^0),$$

$$\left(\frac{v_1 - v_1^0}{c_f}\right)^2 = (\varepsilon_1 - \varepsilon_f)(\varepsilon_1 - \varepsilon_1^0) \quad \left(\varepsilon_f = \frac{2\tau}{\sqrt{3}k}\right),$$

where $c_p = \sqrt{\frac{k + 4\mu/3}{\rho}}$ and $c_f = \sqrt{\frac{k}{\rho}}$ are the velocities of the elastic and plastic shock waves, which are the angular coefficients of the corresponding asymptotes. The signoton velocities are determined by the angular coef-

ficients of the secants joining the states (ε_1^0, v_1^0) and (ε_1, v_1) ahead of and behind the front, respectively.

For $\varepsilon_1 \geq \varepsilon_\tau$, the solution to the elastic problem was described in [7]. A typical configuration of discontinuities arising in an elastoplastic medium in the absence of initial stresses contains two shock waves: the elastic precursor wave, which propagates with velocity c_p and behind the front of which the stresses tend to the yield surface, and the plastic wave [6]. This configuration is observed in a densified loose medium ($\varepsilon_1^0 \leq 0$). In a loosened medium, the precursor wave gives way to an elastic signoton moving with the lower velocity

$$c_\tau = c_p\sqrt{-\frac{\varepsilon_\tau}{\varepsilon_1^0 - \varepsilon_\tau}}.$$

If the strain ahead of the front ε_1^0 exceeds ε_f, the velocity of the signoton–precursor is less than c_f. The shock wave turns over, and the two-wave configuration is replaced by a solitary plastic signoton moving with the velocity

$$c = c_f\sqrt{\frac{\varepsilon_f - \varepsilon_1}{\varepsilon_1^0 - \varepsilon_1}} < c_f.$$

Variational inequality (6) allows a discontinuous solution with a solitary plastic signoton under the condition

$$\varepsilon_1(\varepsilon_1^0 - \varepsilon_f) \leq \varepsilon_f(\varepsilon_1^0 - \varepsilon_\tau),$$

even if $\varepsilon_1^0 < \varepsilon_f$. In this case, the unique solution is chosen by the principle of the maximum rate of energy dissipation on the discontinuity. This rate is determined by the left-hand side of inequality (6) at $\bar{U} = 0$. For the plastic signoton, the energy-dissipation rate is equal to

$$d = \frac{1}{2}ck\{\varepsilon_f(\varepsilon_1^0 + \varepsilon_\tau) - \varepsilon_1(\varepsilon_1^0 + \varepsilon_f)\}.$$

On the precursor and plastic shock waves,

$$d_\tau + d_f = \frac{1}{2}c_\tau k\varepsilon_1^0(\varepsilon_f - \varepsilon_\tau) + c_f k\varepsilon_f(\varepsilon_\tau - \varepsilon_1).$$

An analysis shows that inequality $d > d_\tau + d_f$ is satisfied only if $\varepsilon_1^0 > \varepsilon_f$. Thus, in a loose medium whose looseness degree is less than the critical value, the one-wave configuration is not realized.

ACKNOWLEDGMENTS

This work was supported by the Russian Foundation for Basic Research, project nos. 99-01-00453 and 01-01-00921.

REFERENCES

1. V. P. Maslov, V. P. Myasnikov, and V. G. Danilov, *Mathematical Simulation of the Accident Unit of the Chernobyl' Nuclear Power Station* (Nauka, Moscow, 1988).
2. A. I. Oleĭnikov, Dokl. Akad. Nauk **334**, 314 (1994) [Phys. Dokl. **39**, 68 (1994)].
3. V. M. Sadovskiĭ, Mat. Model. **13** (5), 62 (2001).
4. A. Haar and T. Karman, in *Theory of Plasticity*, Ed. by Yu. N. Rabotnov (Inostrannaya Literatura, Moscow, 1948), pp. 41–56.
5. G. I. Bykovtsev and D. D. Ivlev, *Theory of Plasticity* (Dal'nauka, Vladivostok, 1998).
6. V. M. Sadovskiĭ, *Discontinuous Solutions in the Problems of the Dynamics of Elastoplastic Media* (Nauka, Moscow, 1997).
7. V. P. Maslov and P. P. Mosolov, Prikl. Mat. Mekh. **49** (3), 419 (1985).

Translated by Yu. Vishnyakov

Doklady Physics, Vol. 47, No. 10, 2002, pp. 750–751. Translated from Doklady Akademii Nauk, Vol. 386, No. 4, 2002, pp. 490–491.

MECHANICS

Nonintegrability of Variational Equations in Quadratures in Some Dynamic Problems

S. L. Ziglin

Presented by Academician V.V. Kozlov March 13, 2002

Received June 14, 2002

Lyapunov [1] proved that the Euler–Poisson system describing the motion of a heavy rigid body near a stationary point has, in all cases except the familiar Euler, Lagrange, and Kovalevskaya cases, a meromorphic particular solution such that the set of equations in variations along this solution has an ambiguous general solution.

In this paper, I will prove that, in all cases except the three indicated above and the Goryachev–Chaplygin case, this set has a meromorphic particular solution such that the set of equations in variations along this solution is nonintegrable in generalized quadratures. The generalized quadrature is understood as follows (cf. [2–4]). A univalent function of one complex variable is called a generalized meromorphic function if it is analytic in the entire complex plane except at most countable points. A function expressed in terms of generalized meromorphic functions by means of differentiation, integration, superposition, and meromorphic operations is called a generalized quadrature function. (According to [2], the meromorphic operation $\bar{F}$ is the correspondence of the set of n functions $f_1, f_2, \ldots, f_n$ to a meromorphic function F defined for almost all argument values, i.e., $\bar{F}: (f_1, f_2, \ldots, f_n) \mapsto F(f_1, f_2, \ldots, f_n)$.)

A similar result is valid for some other systems. Among these systems are the Henon–Heiles system [5], the Yang–Mills system for a uniform two-component field with the $\mathbb{SU}(2)$ gauge group [6], Suslov's problem of the motion of a rigid body near a stationary point with a nonholonomic constraint in the case considered by Kozlov [7] for unequal moments of inertia with respect to a chosen axis, and the familiar system describing a steady flow of an ideal incompressible fluid with periodic boundary conditions and a velocity field collinear to its curl (see, e.g., [8]), which is called *ABC* flow, for $A^2 = B^2 \neq 0$ and $C^2 \neq \dfrac{2A^2(n^2-1)}{n^2+7}$, where n is an integer, or $C^2 = A^2$.

Theorem. *Each of the systems above has a meromorphic particular solution such that the set of equations in variations along it is nonintegrable in generalized quadratures.*

Note. Therefore, the general solution to these systems is not expressed in terms of generalized quadratures depending analytically on the initial conditions (cf. [1]).

Proof. According to [3], if a linear set of differential equations with meromorphic coefficients is integrable in generalized quadratures, its monodromy group has a triangular (i.e., consisting of triangular matrices in the corresponding basis) normal subgroup of a finite index. Here, the monodromy group is the group of linear transformations under the action of the system when the independent variable goes around closed paths with a common initial point in the complex plane. However, it can also be treated as a group of transformations under the action of this system when the independent variable varies along paths that have a common initial point and whose beginnings and ends differ by the period of coefficients. Indeed, according to [9], a matrix group over a zero-characteristic field has a finite-index triangular normal subgroup even when this group has a finite chain of subgroups embedded into each other. This chain must be such that the first of the subgroups coincides with the entire group and the last subgroup consists of the unit element. Moreover, each subsequent subgroup is the normal subgroup of the preceding subgroup with the commutative or finite factor group, and the monodromy group in the first sense is the normal subgroup of the monodromy group in the second sense with the commutative factor group. We will use this term in the latter sense.

In [10–14], for each of the above systems, the existence of a meromorphic particular solution such that the set of equations in variations along this solution has meromorphic coefficients was proven. Moreover, the monodromy group G of the reduced variational set, i.e., the restrictions of the set in the normal variations to the zero level surface of its first integrals linear in the fibers

Institute of Radio Engineering and Electronics, Russian Academy of Sciences, ul. Mokhovaya 18, Moscow, 103907 Russia

1028-3358/02/4710-0750$22.00

of the normal fiber space (cf. [15]), is a subgroup of the $\mathbb{SL}(2, \mathbb{C})$ group. In addition, its transformations are different from the roots of the identical transformation and have no common eigenvector. The set of eigenvectors of each such transformation coincides with the set of eigenvectors of any of its nonzero powers. Any finite-index normal subgroup of the group G involves each of these transformations in a certain nonzero power and, therefore, is not triangular. Since the group G is the homomorphic image of the monodromy group of the variational set, this set also has no triangular finite-index normal subgroup Q.E.D.

ACKNOWLEDGMENTS

I am grateful to A.G. Khovanskiĭ for valuable discussion and to A.I. Neishtadt for useful remarks.

REFERENCES

1. A. M. Lyapunov, *Collected Works* (Acad. Sci. SSSR, Moscow, 1954), Vol. 1, pp. 402–417.
2. A. G. Khovanskiĭ, Usp. Mat. Nauk **26** (4), 251 (1971).
3. A. G. Khovanskiĭ, J. Dyn. Control Syst. **1** (1), 91 (1995).
4. V. I. Arnol'd and Yu. S. Il'yashenko, *Itogi Nauki Tekh., Sovremennye Problemy Mat., Fundamental'nye Napravleniya* (VINITI, Moscow, 1985), Vol. 1, pp. 7–149.
5. M. Henon and C. Heiles, Astron. J. **9**, 73 (1964).
6. N. N. Bogoliubov and D. V. Shirkov, *Quantum Fields* (Nauka, Moscow, 1980; Reading, Maas, 1982).
7. V. V. Kozlov, Usp. Mekh. **8** (3), 85 (1985).
8. V. M. Arnold, *Mathematical Methods of Classical Mechanics* (Nauka, Moscow, 1974; Springer, New York, 1989).
9. A. G. Khovanskiĭ, Candidate's Dissertation in Physics and Mathematics (Moscow, 1973).
10. S. L. Ziglin, Funkts. Analiz Prilozh. **17** (1), 8 (1983).
11. S. L. Ziglin, Dokl. Akad. Nauk SSSR **292** (4), 804 (1987).
12. S. L. Ziglin, Usp. Mat. Nauk **52** (2), 167 (1997).
13. S. L. Ziglin, Funkts. Analiz Prilozh. **30** (2), 80 (1996).
14. S. L. Ziglin and V. A. Cherepenin, Dokl. Akad. Nauk **369** (2), 173 (1999).
15. S. L. Ziglin, Funkts. Analiz Prilozh. **16** (3), 30 (1982).

Translated by R. Tyapaev

Doklady Physics, Vol. 47, No. 10, 2002, pp. 752–754. Translated from Doklady Akademii Nauk, Vol. 386, No. 5, 2002, pp. 618–620.

MECHANICS

A "Hard" Excitation of Three-Dimensional Finite-Amplitude Perturbations in Free Flows

S. Ya. Gertsenshteĭn and A. V. Zhukova

Presented by Academician G.G. Chernyĭ June 7, 2002

Received June 25, 2002

From a number of theoretical studies [1–3], it is known that the so-called soft excitation of two-dimensional (plane) perturbations (of the type of the famous Karman vortex street) takes place in a mixing layer and free jet flows. This "soft" scenario of transition to turbulence is observed in many experiments [4].

However, a qualitatively different transition was observed in certain experiments [5]. In this case, three-dimensional perturbations were developed, the characteristic scales of perturbations changed, etc. At the same time, these perturbations must not be developed according to Squire's theorem, because two-dimensional perturbations increase faster than three-dimensional perturbations.

It was here that the hypothesis about a possible "hard" instability of the flows under consideration appeared. However, it concerns not conventional plane waves, but three-dimensional finite-amplitude perturbations involving the so-called difference resonance of a pair of symmetric waves propagating at the same angle to the main flow [6–8]:

$$A(t)\Psi_1(y)\sin(\alpha x + \beta z + \omega t) + A(t)\Psi_2(y)\cos(\alpha x + \beta z + \omega t),$$

$$A(t)\Psi_1(y)\sin(\alpha x - \beta z + \omega t) + A(t)\Psi_2(y)\cos(\alpha x - \beta z + \omega t)$$

with the transverse standing wave

$$\varphi_1(y, t)\sin(2\beta z) + \varphi_2(y, t)\cos(2\beta z).$$

In this case, the nonlinear interaction of symmetric waves generates a transverse standing wave, which, in turn, interacting with the primary waves, induces them anew.

Institute of Mechanics, Moscow State University, Michurinskiĭ pr. 1, Moscow, 117192 Russia

According to linear theory, we have

$$A = A_0 e^{a_0 t}, \quad \frac{dA}{dt} = a_0 A.$$

In the nonlinear case, following Landau and the Stuart–Watson method [9], we have

$$\frac{dA}{dt} = f(A) \approx a_0 A + a_3 A^3.$$

We aim at calculating a^3. If $a_3 < 0$, soft excitation takes place; i.e., a small perturbation first rises exponentially (nonlinear terms are small) for $a_0 > 0$. Further, the nonlinear terms weaken the primary rise, and the amplitude tends to a certain limit: $A \longrightarrow \sqrt{-\frac{a_0}{a_3}}$.

If $a_3 > 0$, even for $a_0 < 0$, i.e., when perturbations with a small amplitude attenuate according to linear theory, perturbations rise $\left(\frac{dA}{dt} > 0\right)$ for a sufficiently large initial amplitude $A_2 > -\frac{a_0}{a_3}$.

Mathematically, the investigation reduces to a rather complicated problem of numerical analysis: the three-dimensional time-dependent Navier–Stokes equations must be solved in the intricate region of transition from a laminar flow to the turbulent one. The solution to this problem can be constructed by the Stuart–Watson method in terms of the corresponding expansions of the desired solution for small initial amplitude. In this case, the analysis reduces to solving sets of ordinary differential equations and the solution is actually obtained in the semianalytical form

$$u_i(x, y, z, t) = Ae^{\lambda t}[\varphi_{1i}(y)\sin(\alpha x + \beta z + \omega t) + \phi_{1i}(y)\sin(\alpha x - \beta z + \omega t)$$

1028-3358/02/4710-0752$22.00

$$+ \varphi_{1i}^*(y)\cos(\alpha x + \beta z + \omega t)$$

$$+ \phi_{1i}^*(y)\cos(\alpha x - \beta z + \omega t)]$$

$$+ A^2 e^{2\lambda t}[p_{2i}(y)\sin(2\alpha x + 2\beta z + 2\omega t)$$

$$+ q_{2i}(y)\sin(2\alpha x - 2\beta z + 2\omega t)$$

$$+ p_{2i}^*(y)\cos(2\alpha x + 2\beta z + 2\omega t)$$

$$+ q_{2i}^*(y)\cos(2\alpha x - 2\beta z + 2\omega t)$$

$$+ s_{2i}(y)\sin(2\alpha x + 2\omega t)$$

$$+ r_{2i}(y)\sin(2\beta z) + s_{2i}^*(y)\cos(2\alpha x + 2\omega t)$$

$$+ r_{2i}^*(y)\cos(2\beta z) + w(y)]$$

$$+ A^3 e^{3\lambda t}[\theta_{3i}(y)\sin(\alpha x + \beta z + \omega t)$$

$$+ \theta_{3i}^*(y)\cos(\alpha x + \beta z + \omega t) + \ldots] + \ldots.$$

Here, $\lambda = \lambda_0 + A^2\lambda_2$, $\omega = \omega_0 + A^2\omega_2$, whereas the nonlinear corrections λ_2 and ω_2 are determined from the condition of solvability of the ordinary differential equations for θ_{3i} and θ_{3i}^*, which are obtained when the substitute the above expansions into the original Navier–Stokes equations and equate the coefficients of the corresponding small-parameter powers to zero. The calculations were performed using a system of analytical transformations on a computer.

Thus, the numerical analysis reduces to solving the problem on eigenvalues for the Orr–Sommerfeld equation in the first approximation, to solving differential equations with inhomogeneous right-hand sides in the second approximation, and to using the conditions of solvability for degenerate differential equations in the third approximation.

This study is devoted to jet flows. The calculations were performed along the neutral curve. The numerical analysis established that the jet with the velocity profile

$$U(y) = \begin{cases} \dfrac{1}{\cosh^2(3)}, & y \geq 3, \\ \dfrac{1}{\cosh^2(y)}, & -3 \leq y \leq 3, \\ \dfrac{1}{\cosh^2(-3)}, & y \leq -3 \end{cases}$$

manifests hard instability with respect to finite-amplitude three-dimensional perturbations. For a fixed wave number α, the coefficient a_3 responsible for the character of perturbation (Fig. 1) can both increase and decrease with increasing Reynolds number. For certain wave numbers α, this coefficient decreases with increasing wave number β (Fig. 2). In the region of the "nose" of the neutral curve, a_3 is close to zero.

In this study, we obtained the distributions of perturbation velocities for certain sets of the parameters (wave numbers and Reynolds number) in the first and second approximations. In the first approximation, these are X and Y components u_{11} and u_{12} of the wave velocity. The Z component u_{13} is qualitatively similar to the X component and differs from the latter only quantitatively. The functions u_{11} and u_{13} are antisymmetric, whereas u_{12} is symmetric (Fig. 3). The behavior of u_{11} is virtually independent of the parameters, whereas the behavior of u_{12} changes strongly with variation of the parameters. For example, the amplitude for a large Reynolds number takes a maximum value at zero and then decreases smoothly.

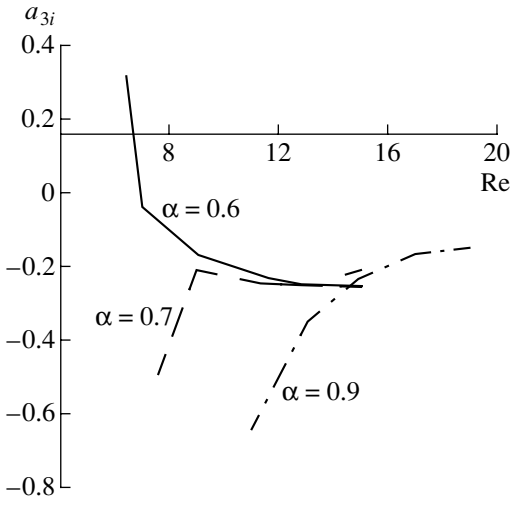

Fig. 1.

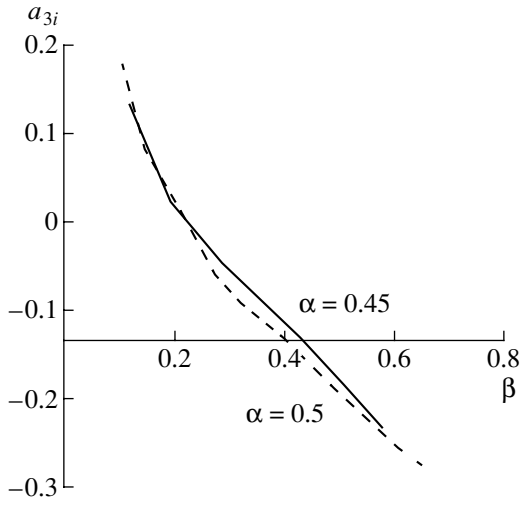

Fig. 2.

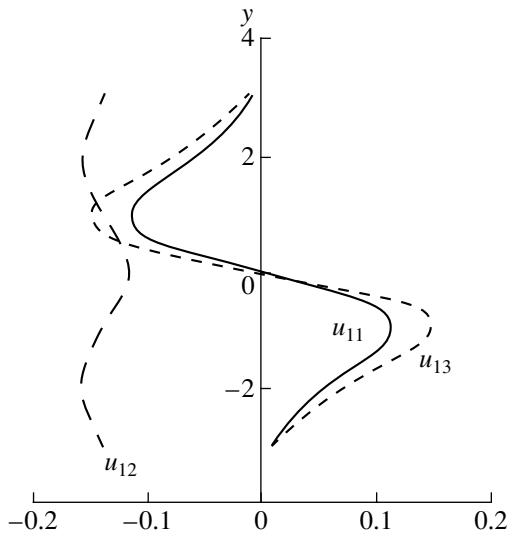

Fig. 3.

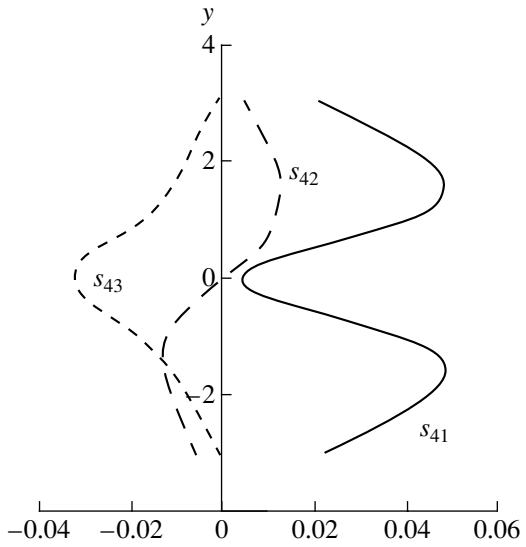

Fig. 4.

As was mentioned above, interaction in the second approximation gives rise to several new waves—$2\alpha x$ (s_{31}, s_{32}), $2\alpha x + 2\beta z$ (s_{11}, s_{12}, s_{13}), $2\beta z$ (s_{41}, s_{42}, s_{43}) (Fig. 4) and to the free term. The behavior of the free term is virtually the same: it has a minimum at the jet axis and tends to zero when y approaches 4 and –4. The X and Z components of the velocity of the waves s_{11} and s_{13} behave identically: they are symmetric, whereas the Y component is antisymmetric. Moreover, the Y components of the $2\alpha x$ and $2\alpha x + 2\beta z$ waves are virtually identical. The functions s_{31}, s_{32}, s_{11}, s_{12}, and s_{13} are not plotted, because they are qualitatively similar to the functions in the linear approximation, and the only difference is that the X and Y components change places. The lowest order has the $(2\alpha x + 2\beta z)$ wave: 10^{-3}–10^{-2}.

Thus, we showed that the transition to chaos for large initial perturbations can qualitatively differ from the transition for small initial perturbations; i.e., the ordinary character of transition can change radically in the case of large initial three-dimensional perturbations.

The region of hard instability was also found in [7] for an axisymmetric jet flow in a circular tube. In this case, hard finite-amplitude instability arises due to a similar mechanism of perturbation initiation: a pair of symmetric spiral waves nonlinearly interacts with the appearing transverse standing wave. In [7], as well as in this study, hard instability was observed at the upper branch of the neutral curve. Instability was not observed in the region of the nose of the neutral curve.

REFERENCES

1. S. Ya. Gertsenshteĭn and Yu. M. Shtemler, Dokl. Akad. Nauk **234**, 1277 (1977) [Sov. Phys. Dokl. **22**, 300 (1977)].
2. S. Ya. Gertsenshteĭn and Yu. M. Shtemler, Izv. Akad. Nauk SSSR, Ser. Mekh. Zhidk. Gaza, No. 1, 150 (1976).
3. Yu. M. Shtemler, Candidate's Dissertation in Physics and Mathematics (Inst. Mekh., Mosk. Gos. Univ., Moscow, 1979).
4. *Album of Fluid Motion*, Ed. by M. Van Dyke (Parabolic Press, Stanford, 1982; Mir, Moscow, 1986).
5. A. A. Pavel'ev, in *Turbulent Flows* (Nauka, Moscow, 1974), p. 185.
6. S. Ya. Gertsenshteĭn, N. V. Nikitin, E. B. Rodichev, and A. N. Sukhorukov, in *Proceedings of the III International Symposium on Turbulence, Novosibirsk, 1984*, p. 46.
7. S. Ya. Gertsenshteĭn and A. N. Sukhorukov, Dokl. Akad. Nauk **359**, 629 (1998) [Dokl. Phys. **43**, 245 (1998)].
8. S. Ya. Gertsenshteĭn and A. V. Zhukova, Dokl. Akad. Nauk **362**, 47 (1998) [Dokl. Phys. **43**, 573 (1998)].
9. L. D. Landau and E. M. Lifshitz, *Mechanics of Continuous Media* (Gostekhizdat, Moscow, 1953), pp. 137–142.

Translated by V. Bukhanov

Doklady Physics, Vol. 47, No. 10, 2002, pp. 755–757. Translated from Doklady Akademii Nauk, Vol. 386, No. 5, 2002, pp. 621–623.

MECHANICS

Numerical Analysis of the Vortex Intensification of Heat Transfer in a Channel with a Set of Deep Spherical Dimples on One of the Walls

S. A. Isaev*, Academician A. I. Leontiev, P. A. Baranov*, I. A. Pyshnyĭ*, and A. E. Usachov*****

Received March 21, 2002

Experimental studies of heat transfer in narrow channels with dimples on the walls (see, e.g., [1, 2]) testify to the promising features of this method for intensifying heat-and-mass exchange processes including cooling of devices for various applications. For a set of deep (on the order of 0.25–0.3 diameters) spherical dimples, a heat-transfer rise by a factor of 2.4–2.5 compared to a smooth-walled channel was demonstrated along with a moderate increase in the hydraulic loss (by a factor of approximately 1.5).

Experimental methods applied to the analysis of the physical mechanism of the heat-transfer intensification turned out to be limited in a certain sense. This is associated with both the multiplicity of affecting causes and a complication of structural features of spatial vortex flows. Therefore, the emphasis in investigations of such flows is all the more shifted towards numerical modeling. At the same time, a unique case of such modeling performed abroad (see, e.g., [3]) was not very informative.

Recently, the authors of the present paper have carried out calculations of convective heat transfer when flowing around a sole dimple located on a plane [4–7]. In the process of these calculations, significant experience in the identification of spatial jet-vortex structures in dimples was accumulated.

The present paper is devoted to calculations of turbulent flows and the heat transfer in a narrow plate-parallel channel with a set of 15 spherical dimples of a considerable depth (0.29) and dense packing (1.155) on one of the channel walls. The channel configuration under consideration is similar to that (Fig. 1a) chosen in [2] for analysis of the convective heat transfer and differs only in the smaller number of dimples in rows and smaller number of elements in each row (Fig. 1b).

In the calculations, the Reynolds number was taken equal to 6×10^3, while the temperature of the hot wall containing dimples attained 350 K, as was the case in the experiment of [2].

We consider a plate-parallel channel with the relative length 30.372, height of 1, and width of 6. The channel is covered with a nonuniform rectangular $78 \times 56 \times 46$ mesh (with the total number of cells on the order of 200000). The mesh steps in the longitudinal and transverse directions of the middle part of the channel are chosen equal to 0.2. The mesh steps near the lower or upper walls and lateral walls are taken to be 0.0005 and 0.005, respectively.

The area with 15 dimples disposed in the staggered order is covered by an additional rectangular mesh with a size of $7.372 \times 0.175 \times 3.866$ and containing $160 \times 20 \times 80$ cells (with their total number on the order of 300000). In the longitudinal and transverse directions, the minimal steps are 0.05, while the size of the near-wall step is 0.0005.

Each of the 15 equal spherical dimples with a relative depth of 0.29 (with respect to the dimple diameter) has a sharp edge. The distance between the dimple rows and between the dimple centers in each row is 1.155 of the dimple diameter.

Each dimple is covered with a cylindrical mesh. It is adapted to a wall, and its shape is close to orthogonal. This mesh is generated with the help of an elliptical procedure with nodes concentrated as the wall is approached. The near-wall step is 0.0005. Along the circumferential coordinate and along a vertical line, 40 and 37 cells are chosen, respectively. Between the dimple center and the sharp edge and in the ring-shaped subdomain with the size of 0.115, 16 and 7 cells are disposed, respectively. It is worth noting that near the axis, the cylindrical mesh in each dimple is replaced by a rectangular one whose cell size agrees with that of the cylindrical mesh.

* *Academy of Civil Aviation, St. Petersburg, Russia*

** *Bauman Moscow State Technical University, Vtoraya Baumanskaya ul. 5, Moscow, 107005 Russia*

*** *State Research Center (TsAGI), ul. Radio 17, Moscow, 107005 Russia*

1028-3358/02/4710-0755$22.00

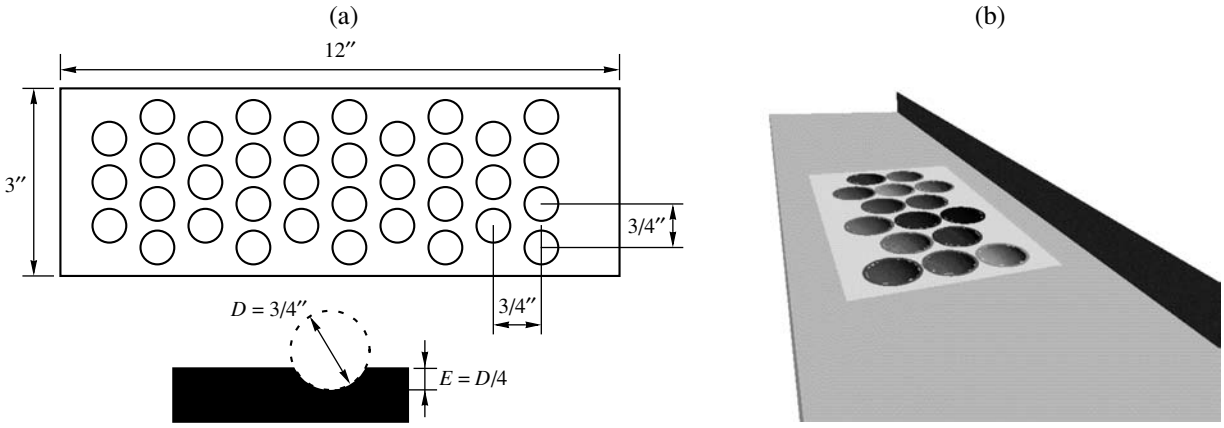

Fig. 1. Configuration of walls with dimple sets in (a) physical experiments and (b) in the given numerical study.

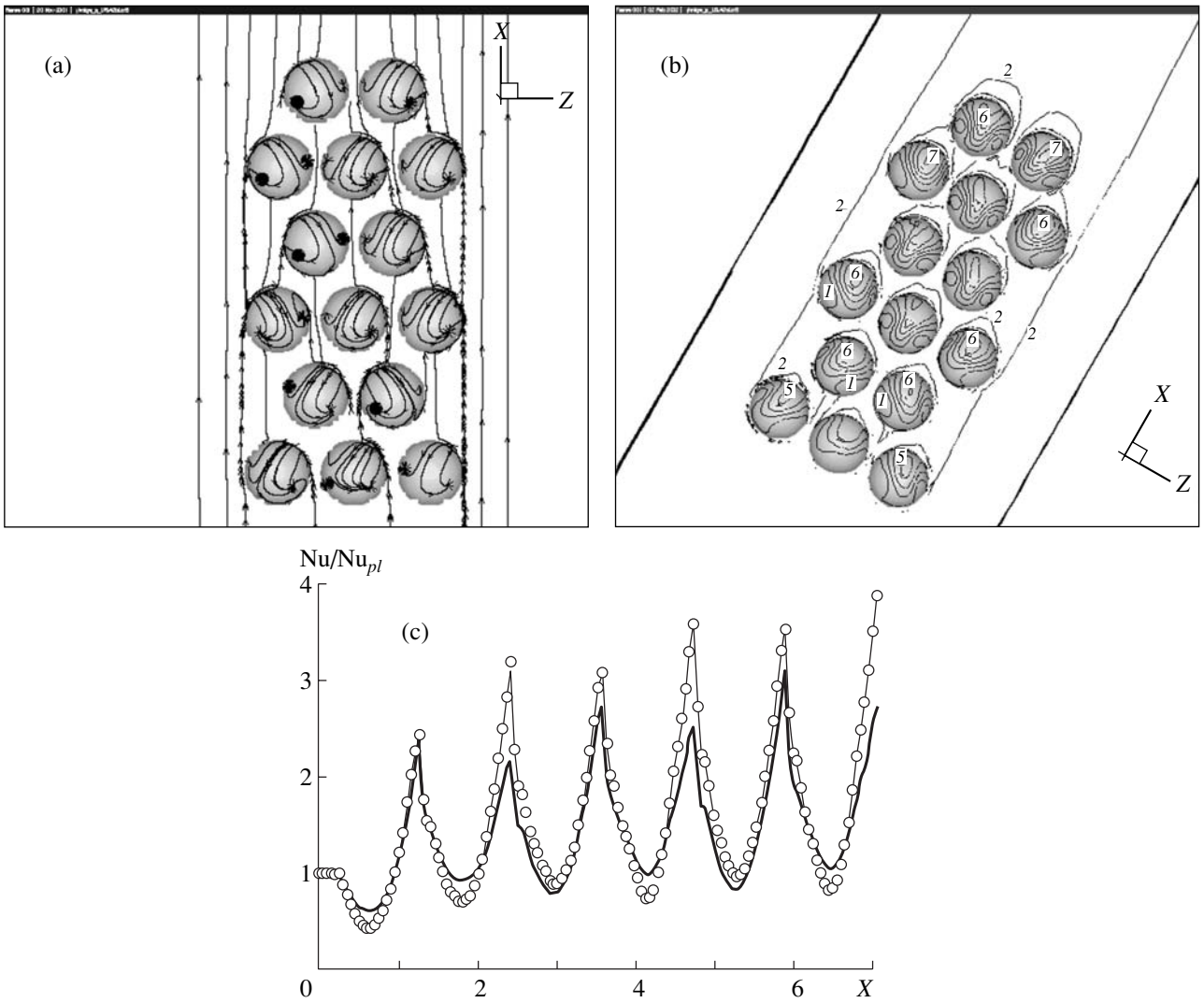

Fig. 2. (a) Patterns for flows around dimples (view from above); (b) isotherms in the near-wall layer (at the altitude of 0.00025 from the wall) in the vicinity of the wall with dimples (axonometry); (c) distributions over the longitudinal coordinate of the relative heat transfer on the wall with dimples while varying the average bandwidth over the transverse coordinate. Solid lines and dots correspond to bandwidths of 4.266 and 2.133, respectively. The digitized isotherms are plotted with a step of 0.5° from 74° to 77° [T = (*1*) 77°; (*2*) 76.5°; (*5*) 75°; (*6*) 74.5°; (*7*) 74°].

In the neighborhood of the dimples, there are approximately 580000 calculation cells.

In the channel input section, a uniform velocity profile is given. At the output boundary, soft boundary conditions are set (conditions of solution continuation). On the channel walls, the adhesion condition is fulfilled. Side walls are assumed to be heat-insulated, while the opposite "cold" wall is considered to be isothermal with a temperature of 293 K. The incoming-flow velocity outside the boundary layer and the dimple diameter are used as normalization parameters. While solving the thermal problem, the laminar and turbulent Prandtl numbers are taken to be 0.7 and 0.9, respectively. Some of the numerical results obtained with the use of a TECPLOT-7.5 system for the computer visualization of spatial fields are presented in Fig. 2.

The analysis of the pattern for flows around the dimple relief (Fig. 2a) shows that asymmetric vortex structures are formed within the dimples. These structures are similar to those observed in [6] for a sole deep dimple. We should note that starting from the third row, the flow patterns in dimples become topologically analogous; i.e., a synchronization of the detached flow in the dimple set is observed.

The pattern of isotherms in the near-wall layer (at a distance of 0.00025 from the wall) and the plot of relative thermal loads averaged over the transverse coordinate in bands of different sizes demonstrate the nonuniformity of the thermal-flow fields on the dimple relief. The most significant fact is the rise of thermal loads, which increases with the number of dimple rows. As is seen from Fig. 2b, the increase in the local heat transfer occurs not only within the dimples but (more importantly) in the near wake beyond them. It is of interest that in this case, the minima of thermal loads onto the wall with dimples remain approximately the same (Fig. 2c).

For the rectangular domain with the size of 7.372×4.266 completely covering the dimple set, the heat-exchange coefficient C_q related to the equivalent area of the smooth wall is equal to 1.62. In the case of a narrower band (as wide as half of the previous one and equal to 2.133), the value of C_q turns out to be higher and equals 1.93. This more adequately corresponds to the situation in the dimple set of a longer extension. It is expedient to determine the relative heat transfer from the dimples by ignoring the effect of the first rows. In order to do this, it is of interest to estimate the heat transfer from the last two dimple rows in the set of 15 dimples under consideration for bandwidth 2.133. It turns out that $C_q = 2.37$, which is consistent with experimental data. It is noteworthy that a weak dependence of C_q on the Reynolds number is found in experiments. This fact makes it possible to correctly perform comparisons similar to the ones mentioned above.

The estimate of an increase in the hydraulic loss for the part of the channel covered with dimples shows that this increase reaches 37%, which also corresponds well to the experimental data of [2].

In conclusion, this study has revealed the interrelation between, on the one hand, the synchronization of large-scale vortex structures generated in the dimple set on one of the walls in a narrow channel and, on the other hand, the intensification of the heat transfer in the channel. In this case, an increase in the heat transfer considerably anticipates a rise of the hydraulic resistance in the channel with dimples. In addition, the efficiency of the developed multibank calculation algorithm is also demonstrated.

ACKNOWLEDGMENTS

The work was supported by the Russian Foundation for Basic Research, project nos. 02-01-01160 and 02-02-17562.

REFERENCES

1. V. V. Alekseev, I. A. Gachechiladze, G. I. Kiknadze, *et al.*, in *Proceeding of the II National Conference on Heat Transfer* (Mosk. Énerg. Inst., Moscow, 1998), Vol. 6, p. 33.
2. M. K. Chyu, Y. Yu, H. Ding, J. P. Downs, and F. O. Soechting, ASME Pap., No. 97-GT-437 (1997).
3. Y.-L. Lin, T. I.-P. Shih, and M. K. Chyu, ASME Pap., No. 99-GT-263 (1999).
4. S. A. Isaev, in *Proceedings of the XII School–Seminar of Young Scientists and Specialists* (Mosk. Énerg. Inst., Moscow, 1999), p. 17.
5. S. A. Isaev, A. I. Leontiev, and P. A. Baranov, Pis'ma Zh. Tekh. Fiz. **26**, 28 (2000) [Tech. Phys. Lett. **26**, 15 (2000)].
6. S. A. Isaev, A. I. Leontiev, P. A. Baranov, and A. E. Usachov, Dokl. Akad. Nauk **373**, 615 (2000) [Dokl. Phys. **45**, 389 (2000)].
7. S. A. Isaev, A. I. Leontiev, P. A. Baranov, *et al.*, J. Phys. Eng. & Thermophys. **74**, 62 (2001).
8. F. R. Menter, AIAA J. **32**, 1598 (1994).

Translated by G. Merzon

Doklady Physics, Vol. 47, No. 10, 2002, pp. 758–761. Translated from Doklady Akademii Nauk, Vol. 386, No. 5, 2002, pp. 624–627.

MECHANICS

Methods of Measuring the Diffusion Coefficient and Sizes of Nanoparticles in a Rarefied Gas

V. Ya. Rudyak[a,c], S. L. Krasnolutskiĭ[a], A. G. Nasibulin[b], and E. I. Kauppinen[b]

Presented by Academician A.K. Rebrov February 17, 2002

Received May 5, 2002

In view of rapid progress in nanotechnologies, it is necessary to develop new methods of determining the diverse physical properties of nanoparticles. The sizes and diffusion coefficient of particles are basic properties. In practice, these properties are determined by so-called differential mobility (electromobility) analyzers (DMAs).[1] The feasibility of using DMAs in this range was shown in [1]. The interpretation of data obtained by this method is based on the Stokes law of resistance with the Canningham–Millikan–Davis corrections. For example, the diffusion coefficient is determined by the formula

$$D_k = \frac{kT}{\gamma_k}, \qquad (1)$$

$$\gamma_k = 6\pi\eta R\left[1 + 1.257\mathrm{Kn} + 0.4\mathrm{Kn}\exp\left(-\frac{1.1}{\mathrm{Kn}}\right)\right]^{-1} = \frac{6\pi\eta R}{C},$$

where $\mathrm{Kn} = \frac{l}{R}$ is the Knudsen number, R is the radius of a particle, and T and η are the temperature and viscosity of the base gas, respectively.

As is known, the Stokes coefficient of resistance $\gamma_s = 6\pi\eta R$ is obtained by solving the Navier–Stokes equations, but the hydrodynamic approximation is inapplicable to nanoparticles (particles with sizes of about 1–100 nm). The Canningham–Millikan–Davis correction does not improve the description. It is introduced only to take into account the rarefaction of a base medium.

In [2], the diffusion of nanoparticles was described by kinetic theory, and the interaction of nanoparticles with base-gas molecules was described by the potential taken from [3]. In particular, Eq. (1) was shown to be valid in a very narrow temperature range. For small particle radii (below 20 nm), the kinetic calculations differ systematically from the values obtained by phenomenological Eq. (1).

In this study, we measured the diffusion coefficient as a function of the diameter of particles in the range mentioned above in order to test both the adequacy of using Eq. (1) to interpret experimental data and its applicability to the diffusion of nanoparticles. Simultaneously, the diffusion coefficient was calculated in kinetic theory [2]. In order to obtain unbiased experimental data, the particle diameters were measured by both the DMA method and electron microscopy (EM). The comparison of the experimental data with theoretical results indicates that, in the range of small sizes, the DMA method leads to a systematic error that is associated with the use of Eq. (1) and can reach several tens of percent for the diffusion coefficient and the sizes of nanoparticles. At the same time, kinetic theory [2] describes the experimental data concerning the diffusion of nanoparticles, at the least, within the experimental errors.

In our experiments, we used nanoparticles of copper oxide Cu_2O, which were produced by the thermal decomposition of the metallorganic precursor of copper acetylacetonate [4, 5]. The experiments were performed in a vertical laminar-flow reactor (its detailed description is available in [4]). As a base gas, we used nitrogen, whose bulk concentration was equal to 99.999%.

In the range 2–200 nm, the size distribution of disperse particles was measured by a differential mobility analyzer consisting of a radioactive ionizer, a classifier [6], and a condensation particle counter (CPC) TSI 3027. An electrostatic precipitator (ESP, InTox) was used to collect the particles on a carbon-coated copper

[1] To date, so-called diffusion batteries are extensively used. However, they face problems when measuring the sizes of rather small particles. On the other hand, this method is also based on relations (1). Therefore, the below analysis of the applicability of the DMA method also largely concerns the method where diffusion batteries are used.

[a] *Novosibirsk State Architectural and Building University, Novosibirsk, Russia*

[b] *VTT Aerosol Technology Group, P.O. Box 1401, FIN-02044 VTT, Finland*

[c] *e-mail: rudyak@ngasu.nsk.ru*

1028-3358/02/4710-0758$22.00

mesh (SPI). The sizes and crystal properties of particles were investigated with a transmission electron microscope (Philips, CM200 FEG).

The operation of DMAs is based on the separation of charged particles in accordance with their mobility. Charged particles (in our case, these are Cu_2O) moving in a potential applied to the plates of a DMA deviate and fall into a narrow split if the particles possess certain mobility [5]. Measuring the electric mobility of the particles Z, we find their diffusion coefficient to be

$$D_D = \frac{ZkT}{ne}, \quad (2)$$

where the particle charge n is measured in units of elementary charge e.

Mobility measured in experiments is related to particle diameter $d = 2R$ as

$$Z = \frac{ne}{\gamma_k}. \quad (3)$$

As a result, using the DMA, we measured the particle diameters d_D (Table 1). In addition, the particle diameters were independently measured by EM, d_E. Figure 1 shows the normalized particle distributions obtained by both methods. It is seen that the curves differ noticeably from each other, and the DMA method overestimates particle sizes. For small particle diameters, these differences reach 20–30%.

The experimental diffusion coefficient can be calculated by Eq. (2). Relating this diffusion coefficient to the particle diameter measured by the DMA and EM methods, we find the DMA diffusion coefficient D_D and the diffusion coefficients D_E. The results are presented in Fig. 2, where the dashed curve corresponds to D_D obtained by using the Canningham–Millikan–Davis correlation (1), whereas points correspond to D_E. For small particle sizes, these coefficients differ considerably from each other.

To obtain the theoretical dependence, we applied the kinetic theory of rarefied gases. As was shown in [7, 8], transport processes in rarefied fine aerosols can be well described by the system of Boltzmann kinetic equations. Then, the diffusion coefficient is determined by the formula [2]

$$D = \frac{3}{16}\frac{\sqrt{2\pi\mu kT}}{n\mu\pi R^2\Omega_{ij}^{(1,1)*}(T^*, \sigma_{ij}/R)}. \quad (4)$$

Here, $\mu = \frac{mM}{(m+M)}$, where m and M are the masses of a base-gas molecule and a disperse particle, respectively;

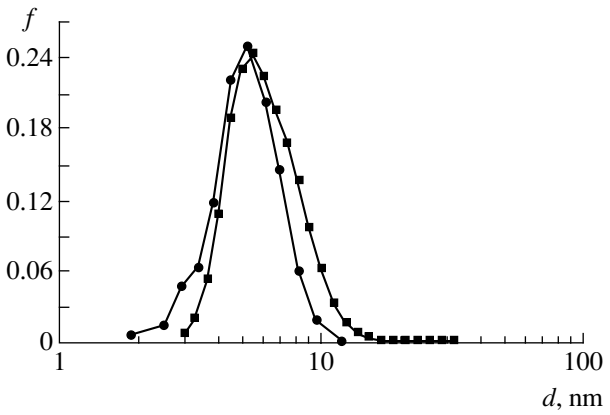

Fig. 1. Distribution function f of the particle diameters d obtained on the basis of the (squares) DMA and (circles) EM measurements.

$T^* = \frac{T}{\varepsilon_{ij}}$; $\Omega_{ij}^{(l,r)*}$ are the so-called reduced Ω-integrals [9]; and ε_{ij} and σ_{ij} are the parameters of the Lennard-Jones potential $\Phi_{ij} = 4\varepsilon_{ij}\left[\left(\frac{\sigma_{ij}}{r}\right)^{12} - \left(\frac{\sigma_{ij}}{r}\right)^{6}\right]$ describing the interaction between base-gas molecules and the atoms (or molecules) of a disperse particle.

In order to use Eq. (4), it is necessary to have an interaction potential between base-gas molecules and the atoms (or molecules) of a disperse particle as a function of the size of this particle. Such a potential was constructed in [3] as a sum of potentials between a given molecule and all atoms of the particle, which was considered as an aggregate of atoms (or molecules). If a solid particle has the radius R and the interaction between its atoms (molecules) and a molecule of the

Table 1. Nanoparticle diameters d_D and d_E measured by the DMA and EM methods, respectively

d_D, nm	d_E, nm
11.26	8.94
9.18	7.54
7.48	6.32
6.75	5.84
6.10	5.35
5.51	4.79
4.98	4.51
4.50	3.87
4.06	3.33
3.67	2.94
3.32	2.55

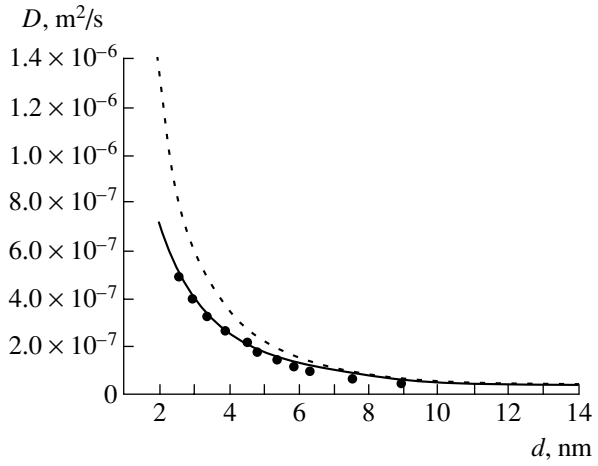

Fig. 2. Diffusion coefficient D vs. the particle diameter d. The solid and dashed curves are obtained with potential (5) and by Canningham–Millikan–Davis formula (1), respectively, and points are experimental data.

base gas is described by the Lenard-Jones potential, the desired potential has the form

$$\Phi(r) = \Phi_9(r) - \Phi_3(r),$$
$$\Phi_i(r) = C_i\{[(r-R)^{-i} - (r+R)^{-i}] - a_i[(r-R)^{-(i-1)} - (r+R)^{-(i-1)}]\}. \quad (5)$$

Here, $a_9 = \frac{9}{8r}$, $a_3 = \frac{3}{2r}$, $C_9 = \frac{4\pi\varepsilon_{ij}\sigma_{ij}^{12}}{45V}$, and $C_3 = \frac{2\pi\varepsilon_{ij}\sigma_{ij}^{6}}{3V}$, where V is the effective volume per molecule of the disperse particle.

It is necessary to calculate the diffusion coefficient of Cu_2O particles in N_2 at atmospheric pressure and temperature T = 21°C. This calculation requires the constants of the pair interaction potential of a base-gas molecule with an atom (molecule) of the particle. To find these constants, we used the combination relations

$$\sigma_{ij} = \sqrt{\sigma_{ii}\sigma_{jj}}, \quad \varepsilon_{ij} = \sqrt{\varepsilon_{ii}\varepsilon_{jj}}.$$

For N_2 molecules, we used ε_{jj} = 71.4 K and σ_{jj} = 3.798 Å [10].

The parameters of the potential of Cu_2O were determined by using the law of corresponding states. Describing the interaction between Cu_2O molecules by the Lenard–Jones potential, we take $\varepsilon_{ii} = 1.92kT_m$, where T_m is the melting point, and $\sigma_{ii} = \sqrt[3]{1.8v_m}$, where v_m is the volume per molecule of the solid phase at the melting point [11]. In calculations, we used the following reference data for Cu_2O: T_m = 1242°C and ρ = 6.1 g/cm³. As a result, we obtain ε_{ii} = 2909 K and σ_{ii} = 4.124 Å. Hence, applying the above combination relations, we find the following constants of the pair interaction potential between a nitrogen molecule and a copper-oxide molecule: ε_{ij} = 455.8 K and σ_{ij} = 3.957 Å.

The solid line in Fig. 2 is the diffusion coefficient obtained in kinetic theory [i.e., by Eqs. (4) and (5)] as a function of the radius of particles. As expected, the difference between the diffusion coefficients is especially noticeable for small disperse particles. The theoretical curve is in good agreement with the experimental data even for particle sizes of about 1 nm. As is seen, with decreasing diameter of particles, diffusion coefficient (1) differs more strongly both from the calculation by Eqs. (4) and (5) and from the experimental data. Table 2 presents the results for the diffusion coefficient. For small radii, the DMA method with the use of the Canningham–Millikan–Davis correlation (1) strongly overestimates the diffusion coefficient. For example, for particles with a typical size of about 2 nm, diffusion coefficient (1) is more than twice as large as both the experimental value (obtained by EM to determine the particle diameter) and theoretical result.

Table 2. Diffusion coefficient D as a function of the particle diameter d

d, nm	D_D, m²/s	D_E, m²/s	D (4), m²/s
8.94	6.701×10^{-8}	4.373×10^{-8}	6.694×10^{-8}
7.54	9.385×10^{-8}	6.543×10^{-8}	9.044×10^{-8}
6.32	1.331×10^{-7}	9.810×10^{-8}	1.215×10^{-7}
5.84	1.557×10^{-7}	1.202×10^{-7}	1.397×10^{-7}
5.35	1.853×10^{-7}	1.470×10^{-7}	1.601×10^{-7}
4.79	2.308×10^{-7}	1.798×10^{-7}	1.932×10^{-7}
4.51	2.602×10^{-7}	2.198×10^{-7}	2.118×10^{-7}
3.87	3.528×10^{-7}	2.689×10^{-7}	2.678×10^{-7}
3.33	4.758×10^{-7}	3.299×10^{-7}	3.418×10^{-7}
2.94	6.097×10^{-7}	4.034×10^{-7}	4.102×10^{-7}
2.55	8.097×10^{-7}	4.925×10^{-7}	5.063×10^{-7}

In summary, we arrive at two basic conclusions.

(i) The DMA method determines the sizes of ultradispersed (below 10 nm) particles with systematic error, because these sizes are determined in terms of electromobility by using Eq. (3) as

$$d = \frac{neC}{3\pi\eta Z}.$$

This formula is valid for sufficiently large particles, but is inapplicable for nanoparticles. As a result, the DMA method leads to systematic errors in the diffusion coefficients of nanoparticles, since the diffusion coefficient is associated with the incorrect particle diameter. As was seen, the errors can reach 100%.

Disadvantages associated with the use of Eq. (1) are inherent in not only the DMA method, but also other methods of measuring the diffusion coefficient of nano-

particles. The method using so-called diffusion batteries also faces similar problems.

(ii) The kinetic theory proposed in [2] satisfactorily describes the diffusion of nanoparticles over a wide temperature range. At the same time, the empirical Canningham–Millikan–Davis Eq. (1) is valid only in the room-temperature range, where its parameters were determined. We emphasize that the diffusion coefficient and the mobility of nanoparticles depend generally not only on the particle diameter but also on the type of base gas and the material of disperse particles. The kinetic theory developed in [2] takes these dependences into account via the interaction potential between base-gas molecules and a dispersive particle.

ACKNOWLEDGMENTS

The authors are grateful to Academician A.K. Rebrov for his interest in the work, stimulating discussions, and support.

This work was supported in part by the Russian Foundation for Basic Research, project nos. 00-15-96164 and 01-01-00045, and National Technology Agency, Finland.

REFERENCES

1. E. O. Knutson and K. T. Whitby, J. Aerosol Sci. **6**, 443 (1975).
2. V. Ya. Rudyak and S. L. Krasnolutskiĭ, Dokl. Akad. Nauk **381**, 623 (2001) [Dokl. Phys. **46**, 897 (2001)].
3. V. Y. Rudyak and S. L. Krasnolucki, in *Proceedings of the XXI International Symposium on Rarefied Gas Dynamics, Marseille, 1999*, Vol. 1, p. 263.
4. A. G. Nasibulin, E. I. Kauppinen, D. P. Brown, and J. K. Jokiniemi, J. Phys. Chem. B **105**, 11067 (2001).
5. A. G. Nasibulin, P. P. Ahonen, O. Richard, *et al.*, J. Nanopart. Res. **3** (5/6), 383 (2001).
6. W. Winklmayr, G. P. Reischl, A. O. Linder, and A. Berner, J. Aerosol Sci. **22** (3), 289 (1991).
7. V. Ya. Rudyak, Pis'ma Zh. Tekh. Fiz. **18** (20), 77 (1992) [Sov. Tech. Phys. Lett. **18**, 681 (1992)].
8. M. Yu. Gladkov and V. Ya. Rudyak, Zh. Tekh. Fiz. **64** (4), 170 (1994) [Tech. Phys. **39**, 441 (1994)].
9. J. Ferziger and H. Kaper, *Mathematical Theory of Transport Processes in Gases* (North-Holland, Amsterdam, 1972; Mir, Moscow, 1976).
10. R. C. Reid, J. M. Prausnitz, and T. K. Sherwood, *Properties of Gases and Liquids* (McGraw-Hill, New York, 1977; Khimiya, Leningrad, 1982).
11. J. O. Hirschfelder, C. F. Curtiss, and R. B. Bird, *Molecular Theory of Gases and Liquids* (Wiley, New York, 1954; Inostrannaya Literatura, Moscow, 1961).

Translated by Yu. Vishnyakov

Doklady Physics, Vol. 47, No. 10, 2002, pp. 762–766. Translated from Doklady Akademii Nauk, Vol. 386, No. 6, 2002, pp. 756–760.

MECHANICS

Numerical Simulation of the Far Momentumless Turbulent Wake in a Linearly Stratified Medium

O. F. Voropaeva*, B. B. Ilyushin, and G. G. Chernykh***

Presented by Academician A.K. Rebrov February 18, 2002

Received March 6, 2002

Free turbulent flows are among the classical objects studied in theoretical, computational, and applied hydrodynamics. Such flows play an important role in flow around a body, in geophysical phenomena, and in power-engineering and ecology problems.

The turbulent wake arising behind an axisymmetric body in a stable stratified medium is an interesting example of a free turbulent flow in space. In the case of comparatively low stratification, the turbulent flow is first developed as in a homogeneous fluid and expands symmetrically. However, buoyancy forces hinder turbulent diffusion in the vertical direction so that the wake becomes oblate far from the body and finally ceases to grow in this direction.

Turbulent wakes behind axisymmetric bodies in a stratified medium were considered in a number of studies [1–10]. A detailed experimental investigation of the turbulent characteristics in the momentumless wake behind a body moving in a linearly stratified liquid was performed in [5]. Studies devoted to experimental modeling, theoretical calculation, and numerical simulation of the dynamics of the momentumless turbulent wake in such a medium were reviewed in [10], where the results of numerical simulation based on the hierarchy of classical semiempirical models of the second-order turbulence were also presented. It was shown that algebraic models of Reynolds stresses make it possible to satisfactorily describe the geometrical characteristics of the wake. The calculated and measured intensities of turbulent fluctuations for the vertical and horizontal velocity components are significantly different. In contrast, models including differential transport equations of normal Reynolds stresses satisfactorily describe the degeneracy of intensities but reproduce the vertical wake size with significant errors.

In this study, we propose an original numerical model of the far momentumless wake in a linearly stratified fluid, which makes it possible to satisfactorily describe the anisotropic degeneracy of the wake. The model is based on the refined approximations of the triple correlations of the velocity field.

STATEMENT OF THE PROBLEM

To describe a flow in the far turbulent wake behind an axisymmetric body in a stratified medium, we apply the following parabolized system of averaged equations of motion, incompressibility, and continuity in the Oberbeck–Boussinesq approximation:

$$U_\infty\frac{\partial U_d}{\partial x}+V\frac{\partial U_d}{\partial y}+W\frac{\partial U_d}{\partial z}=\frac{\partial}{\partial y}\langle u'v'\rangle+\frac{\partial}{\partial z}\langle u'w'\rangle, \quad (1)$$

$$\begin{aligned}U_\infty\frac{\partial V}{\partial x}+V\frac{\partial V}{\partial y}+W\frac{\partial V}{\partial z}\\ =-\frac{1}{\rho_0}\frac{\partial\langle p_1\rangle}{\partial y}-\frac{\partial}{\partial y}\langle v'^2\rangle-\frac{\partial}{\partial z}\langle v'w'\rangle,\end{aligned} \quad (2)$$

$$\begin{aligned}U_\infty\frac{\partial W}{\partial x}+V\frac{\partial W}{\partial y}+W\frac{\partial W}{\partial z}\\ =-\frac{1}{\rho_0}\frac{\partial\langle p_1\rangle}{\partial z}-\frac{\partial}{\partial y}\langle v'w'\rangle-\frac{\partial}{\partial z}\langle w'^2\rangle-g\frac{\langle\rho_1\rangle}{\rho_0},\end{aligned} \quad (3)$$

$$\begin{aligned}U_\infty\frac{\partial\langle\rho_1\rangle}{\partial x}+V\frac{\partial\langle\rho_1\rangle}{\partial y}+W\frac{\partial\langle\rho_1\rangle}{\partial z}+W\frac{d\rho_s}{dz}\\ =-\frac{\partial}{\partial y}\langle v'\rho'\rangle-\frac{\partial}{\partial z}\langle w'\rho'\rangle,\end{aligned} \quad (4)$$

$$\frac{\partial V}{\partial y}+\frac{\partial W}{\partial z}=0. \quad (5)$$

Here, U_∞ is the velocity of the undisturbed liquid; $U_d = U_\infty - U$ is the defect of the averaged longitudinal com-

* *Institute of Computational Technologies, Siberian Branch, Russian Academy of Sciences, pr. Akademika Lavrent'eva 6, Novosibirsk, 630090 Russia*

** *Institute of Thermophysics, Siberian Branch, Russian Academy of Sciences, pr. Akademika Lavrent'eva 1, Novosibirsk, 630090 Russia*

1028-3358/02/4710-0762$22.00

ponent of the velocity; $U = U_1$, $V = U_2$, and $W = U_3$ are the velocity components of the averaged motion along the x, y, and z axes, respectively; p_1 is the deviation of the pressure from hydrostatic pressure associated with the stratification of ρ_s; g is the acceleration of gravity; $\rho_1 = \rho - \rho_s$; $\langle\rho_1\rangle$ is the averaged density defect; $\rho_s = \rho_s(z)$ is the density of the undisturbed liquid: $\frac{d\rho_s}{dz} \le 0$ (stable stratification); $\rho_0 = \rho_s(0)$; the prime denotes pulsating components; and the angular brackets mean averaging. The coordinate system is fixed to the moving body such that the velocity of the body is equal to $-U_\infty$ and the z axis is directed upwards, i.e., opposite to the force of gravity. It is assumed that the density of the liquid is a linear function of temperature and stratification is weak. The terms responsible for molecular viscosity and diffusion in Eqs. (1)–(4) and $\frac{\partial U}{\partial x}$ in Eq. (5) are assumed to be small and are omitted (this assumption is discussed in [6, 10]).

The system of equations (1)–(5) is nonclosed. Taking into account the specific character of the flow in the wake, we write the Reynolds stresses $\langle u'v'\rangle$ and $\langle u'w'\rangle$ in the form [9, 10]

$$\langle u'v'\rangle = \frac{1-c_2}{c_1}\frac{e\langle v'^2\rangle}{\varepsilon}\frac{\partial U_d}{\partial y} = K_y\frac{\partial U_d}{\partial y}, \tag{6}$$

$$\langle u'w'\rangle = \frac{(1-c_2)e\langle w'^2\rangle - \frac{(1-c_3)(1-c_{2T})}{c_{1T}}\frac{g}{\rho_0}\frac{e^2}{\varepsilon}\langle w'\rho'\rangle}{c_1\varepsilon\left(1-\frac{(1-c_3)}{c_1c_{1T}}\frac{g}{\rho_0}\frac{e^2}{\varepsilon^2}\frac{\partial\langle\rho\rangle}{\partial z}\right)} \times\frac{\partial U_d}{\partial z} = K_z\frac{\partial U_d}{\partial z}. \tag{7}$$

The components of the Reynolds stress tensor can be found by solving the differential transport equations [11] ($i = j = 1, 2, 3$; $i = 2, j = 3$)

$$U_\infty\frac{\partial\langle u_i'u_j'\rangle}{\partial x} + V\frac{\partial\langle u_i'u_j'\rangle}{\partial y} + W\frac{\partial\langle u_i'u_j'\rangle}{\partial z} = -\frac{\partial}{\partial x_l}\langle u_l'u_i'u_j'\rangle + P_{ij} + G_{ij} - \frac{2}{3}\delta_{ij}\varepsilon - c_1\frac{\varepsilon}{e}\left(\langle u_i'u_j'\rangle - \frac{2}{3}\delta_{ij}e\right) - c_2\left(P_{ij} - \frac{2}{3}\delta_{ij}P\right) - c_2\left(G_{ij} - \frac{2}{3}\delta_{ij}G\right), \tag{8}$$

$$P_{ij} = -\left\{\langle u_i'u_k'\rangle\frac{\partial U_j}{\partial x_k} + \langle u_j'u_k'\rangle\frac{\partial U_i}{\partial x_k}\right\},$$

$$G_{ij} = \frac{1}{\rho_0}(\langle u_i'\rho'\rangle g_j + \langle u_j'\rho'\rangle g_i), \quad i, j, k = 1, 2, 3, \tag{9}$$

$$e = \frac{1}{2}(\langle u'^2\rangle + \langle v'^2\rangle + \langle w'^2\rangle),$$

$$\mathbf{g} = (0, 0, -g), \quad 2P = P_{ii}, \quad 2G = G_{ii}.$$

Hereafter, summation over repeated indices is assumed.

The triple correlations of the pulsating components of the velocity field are calculated from the relationships [12]

$$\langle u_l'u_i'u_j'\rangle = \frac{\langle u_l'u_i'u_j'\rangle^0 - \frac{\lambda}{c_3}\frac{g}{\rho_0}\frac{e}{\varepsilon}\langle u_i'u_j'\rho'\rangle}{1-\frac{\lambda}{c_3c_{3\theta}}\frac{g}{\rho_0}\frac{e^2}{\varepsilon^2}\frac{\partial\langle\rho\rangle}{\partial z}}, \tag{10}$$

$$\lambda = \delta_{l3} + \delta_{i3} + \delta_{j3},$$

where the moments $\langle u_l'u_i'u_j'\rangle^0$ and $\langle u_i'u_j'\rho'\rangle$ are determined as [13, 14]

$$-\langle u_l'u_i'u_j'\rangle^0 = c_s\frac{e}{\varepsilon}\langle u_k'u_l'\rangle\frac{\partial\langle u_i'u_j'\rangle}{\partial x_k}, \tag{11}$$

$$-\langle u_i'u_j'\rho'\rangle = c_{s\varphi}\frac{e}{\varepsilon}\left(\langle u_k'u_j'\rangle\frac{\partial\langle u_i'\rho'\rangle}{\partial x_k} + \langle u_k'u_i'\rangle\frac{\partial\langle u_j'\rho'\rangle}{\partial x_k}\right) \approx c_{s\varphi}\frac{e}{\varepsilon}\left(\langle u_j'u_j'\rangle\frac{\partial\langle u_i'\rho'\rangle}{\partial x_j} + \langle u_i'u_i'\rangle\frac{\partial\langle u_j'\rho'\rangle}{\partial x_i}\right). \tag{12}$$

For the more detailed description of the vertical diffusion of the quantity $\langle w'^3\rangle$, we use the differential equation [12]

$$U_\infty\frac{\partial\langle w'^3\rangle}{\partial x} + V\frac{\partial\langle w'^3\rangle}{\partial y} + W\frac{\partial\langle w'^3\rangle}{\partial z} = -\frac{\partial}{\partial y}C_{3332} - \frac{\partial}{\partial z}C_{3333} - 3\left\{\langle v'w'\rangle\frac{\partial\langle w'^2\rangle}{\partial y} + \langle w'^2\rangle\frac{\partial\langle w'^2\rangle}{\partial z}\right\} - 3\frac{g}{\rho_0}\langle w'^2\rho'\rangle - c_{3w}\frac{\langle w'^3\rangle\varepsilon}{e}, \tag{13}$$

where the functions C_{3332} and C_{3333} are fourth-order cumulants, which are approximated as [12]

$$C_{3332} = -\frac{1}{c_4}\frac{e\langle v'^2\rangle}{\varepsilon\left(1-\frac{3}{c_4c_{4\theta}}\frac{g}{\rho_0}\frac{e^2}{\varepsilon^2}\frac{\partial\langle\rho\rangle}{\partial z}\right)}\frac{\partial\langle w'^3\rangle}{\partial y},$$

$$C_{3333} = -\frac{4}{c_4}\frac{e\langle w'^2\rangle}{\varepsilon\left(1-\frac{4}{c_4c_{4\theta}}\frac{g}{\rho_0}\frac{e^2}{\varepsilon^2}\frac{\partial\langle\rho\rangle}{\partial z}\right)}\frac{\partial\langle w'^3\rangle}{\partial z}.$$

The dissipation rate ε is found from the differential equation

$$U_\infty\frac{\partial\varepsilon}{\partial x}+V\frac{\partial\varepsilon}{\partial y}+W\frac{\partial\varepsilon}{\partial z}=\frac{\partial}{\partial y}\frac{c_s e}{\sigma\varepsilon}\langle v'^2\rangle\frac{\partial\varepsilon}{\partial y}+\frac{\partial}{\partial z}\frac{c_s e}{\sigma\varepsilon}\langle w'^2\rangle\frac{\partial\varepsilon}{\partial z}+c_{\varepsilon1}\frac{\varepsilon}{e}(P+G)-c_{\varepsilon2}\frac{\varepsilon^2}{e}. \quad (14)$$

The turbulent flows $\langle u_i'\rho'\rangle$ and the variance of the density fluctuations $\langle\rho'^2\rangle$ are determined on the basis of the local equilibrium representations:

$$\langle\rho'^2\rangle = -\frac{2}{c_T}\frac{e}{\varepsilon}\langle w'\rho'\rangle\frac{\partial\langle\rho\rangle}{\partial z},$$

$$-\langle u'\rho'\rangle = \frac{1}{c_{1T}}\frac{e}{\varepsilon}\left[\langle u'w'\rangle\frac{\partial\langle\rho\rangle}{\partial z}+(1-c_{2T})\langle w'\rho'\rangle\frac{\partial U}{\partial z}\right],$$

$$-\langle v'\rho'\rangle = \frac{1}{c_{1T}}\frac{e}{\varepsilon}\langle v'^2\rangle\frac{\partial\langle\rho\rangle}{\partial y} = K_{\rho y}\frac{\partial\langle\rho\rangle}{\partial y},$$

$$-\langle w'\rho'\rangle = \frac{e}{c_{1T}\varepsilon}\left[\langle w'^2\rangle\frac{\partial\langle\rho\rangle}{\partial z}+(1-c_{2T})\frac{g}{\rho_0}\langle\rho'^2\rangle\right]$$

$$= \frac{e\langle w'^2\rangle}{c_{1T}\varepsilon\left(1-2\frac{1-c_{2T}}{c_{1T}c_T}\frac{g}{\rho_0}\frac{e^2}{\varepsilon^2}\frac{\partial\langle\rho\rangle}{\partial z}\right)}\frac{\partial\langle\rho\rangle}{\partial z} = K_{\rho z}\frac{\partial\langle\rho\rangle}{\partial z}.$$

The empirical constants in this model are quite generally accepted [11–14]: $c_1 = 2.2$, $c_2 = 0.55$, $c_{1T} = 3.2$, $c_{2T} = 0.5$, $c_T = 1.25$, $c_{\varepsilon1} = 1.45$, $c_{\varepsilon2} = 1.9$, $c_s = 0.22$, $\sigma = 1.3$, $c_{s\varphi} = 0.11$, $c_3 = 4.5$, $c_{3\theta} = 4.5$, $c_{3w} = \frac{3}{c_s}$, $c_4 = 2c_{3w} - 1$, and $c_{4\theta} = \frac{2}{c_{s\varphi}} - 1$.

The variable x in Eqs. (1)–(4), (8), (13), and (14) plays the role of time: $t = \frac{x}{U_\infty}$. The initial conditions are consistent with experimental data on the evolution of a momentumless turbulent wake in a homogeneous liquid [5, 6] and are set at a distance $x_0 = 8D$ from the body.

The problem is solved numerically in dimensionless variables, where lengths and velocities are measured in the body diameter D and the incident flow velocity U_∞, respectively. Then, the characteristic parameters of the flow in the momentumless wake in a stratified medium—the Froude number F_D and the Väsälä–Brunt period T—are determined as

$$F_D = \frac{U_\infty T}{D}, \quad T = \frac{2\pi}{\sqrt{ag}}; \quad a = -\frac{1}{\rho_0}\frac{d\rho_s}{dz}, \quad z = 0.$$

The computational finite-difference algorithm is based on the splitting method with respect to spatial variables and was explained in detail in [9, 10].

CALCULATION RESULTS

Dynamics of the momentumless turbulent wake in the linearly stratified medium is illustrated in Figs. 1–3. Here, curves *1* correspond to the numerical calculations

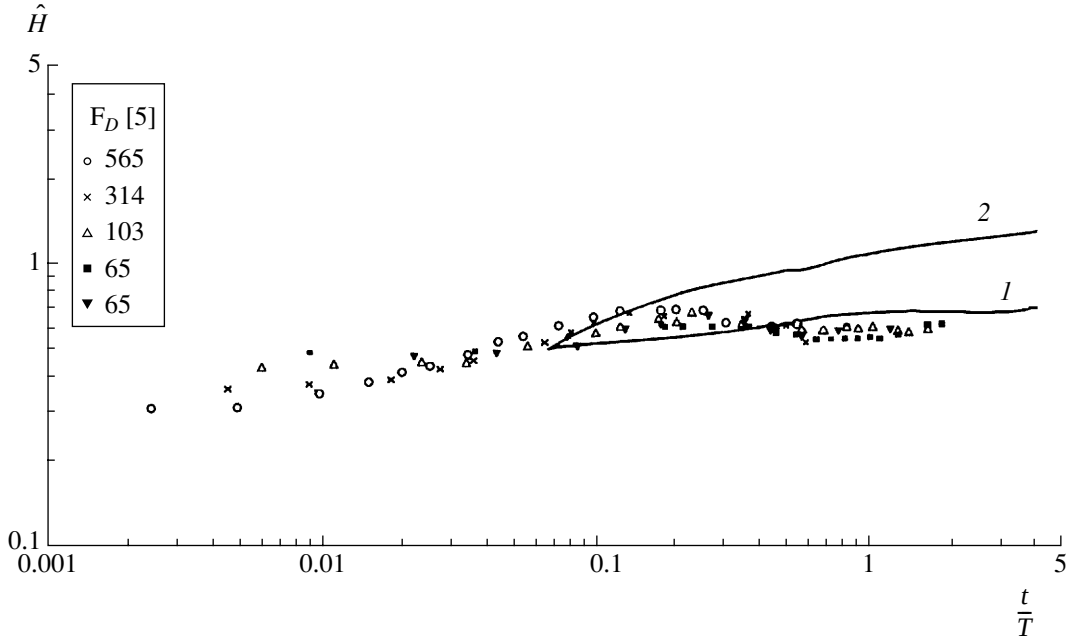

Fig. 1. Evolution of the vertical size of the turbulent wake.

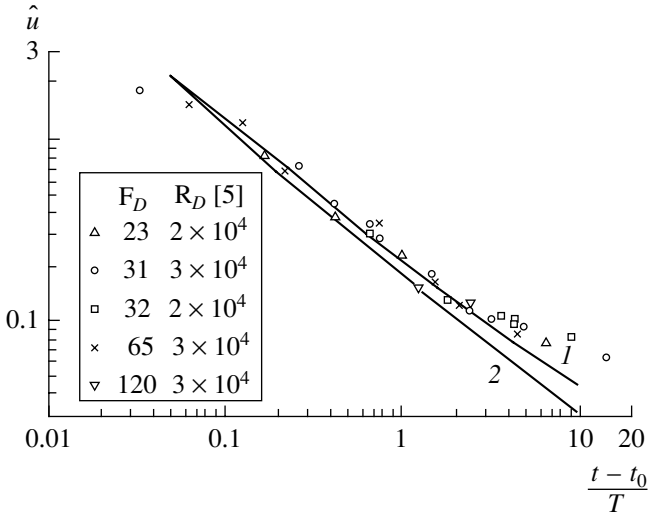

Fig. 2. Dimensionless intensity of the turbulent fluctuations of the longitudinal velocity at the wake axis.

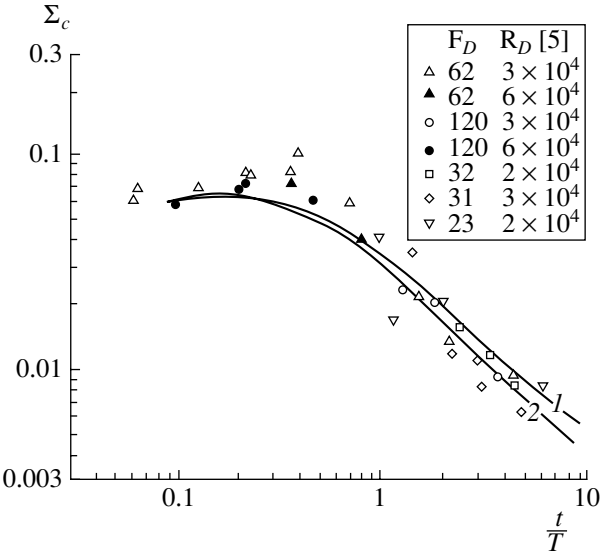

Fig. 3. Dimensionless axial variance of turbulent fluctuations of the density field.

based on the above model, points are the data of laboratory experiments [5], and curves *2* are the results obtained in the mathematical model [10], where in contrast to our model, the classical approximations of all triple correlations of the velocity field were used:

$$\langle u_l' u_i' u_j' \rangle = \langle u_l' u_i' u_j' \rangle^0.$$

Figure 1 shows the variation of the vertical size H of the wake in a plane orthogonal to the direction of the body motion. The value of H was determined from the relationship

$$e(t, 0, H) = 0.01 e(t, 0, 0), \quad \hat{H} = \frac{2H}{D(c_D F_D)^{1/4}},$$

where $c_D = 0.22$ is the drag coefficient. As is seen in Fig. 1, the results obtained in our model are in good agreement with the experimental data.

Figure 2 shows the evolution of the axial intensities for the turbulent fluctuations $\hat{u}$ of the longitudinal velocity

$$\hat{u} = \left(\frac{F_D^{3/2} \langle u'^2(t, 0, 0) \rangle}{U_\infty^2} \right)^{1/2}, \quad t_0 = \frac{2}{F_D}.$$

It is seen that the proposed model with the refined approximations of triple correlations (10) and differential equation (13) is more adequate at large $\frac{t}{T}$. The values of the vertical velocity that were calculated in this model also satisfactorily agree with the experimental data of [5].

Figure 3 shows the calculated intensities of turbulent density fluctuations

$$\Sigma_c = \frac{(\langle \rho'^2(t, 0, 0) \rangle)^{1/2}}{aD\rho_0 F_D^{1/4}}$$

and corresponding experimental data of [5]. The calculations agree well with the experimental data.

Thus, in this study, a numerical model of a far momentumless turbulent wake in a linearly stratified fluid was constructed on the basis of refined approximations for the triple correlations of turbulent fluctuations. The calculated and experimental results are in good agreement.

ACKNOWLEDGMENTS

This work was supported by the Russian Foundation for Basic Research (project no. 01-01-00783), the Siberian Branch of RAS (integration project no. 2000-1), and the INTAS (grant no. 97-2022).

REFERENCES

1. A. H. Schooley and R. W. Stewart, J. Fluid Mech. **15**, Part 1, 83 (1963).
2. A. T. Onufriev, Prikl. Mekh. Tekh. Fiz., No. 5, 68 (1970).
3. O. F. Vasil'ev, B. G. Kuznetsov, Yu. M. Lytkin, and G. G. Chernykh, Izv. Akad. Nauk SSSR, Mekh. Zhidk. Gaza, No. 3, 45 (1974).
4. W. S. Lewellen, M. E. Teske, and C. D. Donaldson, AIAA J. **14**, 382 (1976).
5. J. T. Lin and Y. H. Pao, Annu. Rev. Fluid Mech. **11**, 317 (1979).

6. S. Hassid, J. Hydronautics **14**, 25 (1980).
7. A. Yu. Danilenko, V. I. Kostin, and A. I. Tolstykh, *On Implicit Algorithm for Calculation of Flows of Homogeneous and Inhomogeneous Fluid* (Vych. Tsentr Akad. Nauk SSSR, Moscow, 1985).
8. G. S. Glushko, A. G. Gumilevskiĭ, and V. I. Polezhaev, Izv. Akad. Nauk, Mekh. Zhidk. Gaza, No. 1, 13 (1994).
9. O. F. Voropaeva and G. G. Chernykh, Mat. Model. **10** (6), 75 (1998).
10. G. G. Chernykh and O. F. Voropayeva, Comput. Fluids **28**, 281 (1999).
11. M. M. Gibson and B. E. Launder, J. Fluid Mech. **86**, 491 (1978).
12. B. B. Ilyushin, in *Closure Strategies for Turbulent and Transition Flows*, Ed. by B. E. Launder and N. D. Sandham (Cambridge Univ. Press, Cambridge, 2001), pp. 424–448.
13. B. J. Daly and F. H. Harlow, J. Phys. Fluids **13**, 2634 (1970).
14. B. E. Launder, in *Turbulence, Topics in Applied Physics*, Ed. by P. Bradshow (Springer, Berlin, 1976), Vol. 12, Chap. 6.

Translated by Yu. Vishnyakov

Doklady Physics, Vol. 47, No. 10, 2002, pp. 767–771. From Doklady Akademii Nauk, Vol. 386, No. 6, 2002, pp. 761–766.

MECHANICS

Solution to the Herrmann–Smith Problem[1]

O. N. Kirillov and A. P. Seyranian

Presented by Academician A.Yu. Ishlinskiĭ May 29, 2002

Received May 31, 2002

In 1958, a problem was posed by Dzhanelidze [1] on the stability of a cantilever column compressed at the free end by a force inclined at a certain angle to the tangent of the elastic line (partially following force). It was shown that, depending on the values of problem parameters, this nonconservative system is subjected to both static (divergence) and dynamic (flutter) instability. Kordas and Życzkowski [2] have thoroughly analyzed the boundaries of stability and instability domains in this problem. Furthermore, Smith and Herrmann [3] have generalized the problem by considering a column attached to the Winkler elastic foundation. They found that the critical load causing the flutter does not depend on the modulus of the uniform elastic foundation. This effect, known as the Herrmann–Smith paradox, has stimulated considerable interest and many publications throughout the world [4–9].

In the present paper, the complete solution to the Herrmann–Smith problem is given. The effect of the elastic-base modulus κ on the stability, flutter, and divergence domains in the plane of parameters (follower force p–deviation angle η) is analyzed. It turned out that the increase in the elastic-foundation modulus shifts the static-instability domain away expanding the stability domain. Since the flutter boundary of the circulatory system is determined by the multiple eigenvalues with the Keldysh chain, the derivative of the critical flutter load with respect to κ at the flutter boundary is zero, whence follows the invariance of the flutter boundary with respect to the variation of the parameter κ. The explicit expression for the gradient of the critical flutter load with respect to the distribution of the elastic-foundation modulus $\kappa(x)$ along the column length is obtained. It is shown that the gradient function has alternating sign. Therefore, the rearrangement of the elastic-foundation modulus $\kappa(x)$ along the column may lead to both an increase and a decrease in the critical flutter load. It turned out that within the range $0.6 \lesssim \eta \le 1$, the free end of the column is the most sensitive to the change of the uniformity of $\kappa(x)$ with respect to the critical load.

[1] The article was submitted by the authors in English.

Institute of Mechanics, Moscow State University, Michurinskiĭ pr. 1, Moscow, 117192 Russia

1. STABILITY DIAGRAM FOR A COLUMN ATTACHED TO AN ELASTIC FOUNDATION

We consider a uniform elastic cantilever column of length L attached to an elastic Winkler base having the constant modulus of rigidity χ (Fig. 1). It is assumed that the free end of the column is loaded by a non-conservative force P whose direction is determined by the parameter η. The case $\eta = 1$ implies that the column is loaded by a purely tangential follower force (Beck's problem). If $\eta = 0$, then the force P is potential (conservative).

We consider plane transverse vibrations of the column introducing dimensionless variables

$$x = \frac{X}{L}, \quad y = \frac{Y}{L}, \quad \tau = t\sqrt{\frac{EI}{\rho A L^4}},$$

$$q = \frac{PL^2}{EI}, \quad \kappa = \frac{\chi L^4}{EI},$$

where t is time, ρ is the column material density, A is the cross-section area, E is the Young modulus, and I is the

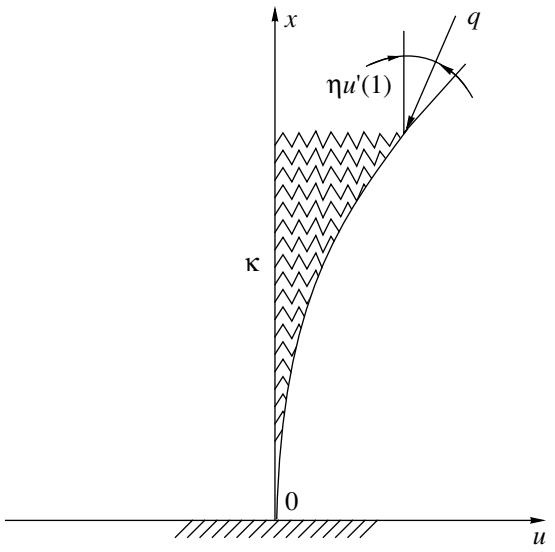

Fig. 1. Column installed on an elastic foundation and loaded by the tangential follower force.

1028-3358/02/4710-0767$22.00

moment of inertia of the column cross section. The differential equation describing small column vibrations and the appropriate boundary conditions have the form

$$y''''(x,\tau) + qy''(x,\tau) + \kappa y(x,\tau) + \ddot{y}(x,\tau) = 0,$$
$$y(0,\tau) = y'(0,\tau) = y''(1,\tau) = y'''(1,\tau) + (1-\eta)qy'(1,\tau) = 0. \quad (1)$$

Here, dots and primes imply differentiation with respect to time τ and coordinate x, respectively. Isolating time in the relationship $y(x,\tau) = u(x)\exp(i\sqrt{\lambda}\tau)$, we arrive at the eigenvalue problem [3]

$$u'''' + qu'' + \kappa u = \lambda u, \quad u(0) = u''(1) = u'(0) = u'''(1) + (1-\eta)qu'(1) = 0. \quad (2)$$

The adjoint problem has the form

$$v'''' + qv'' + \kappa v = \lambda v, \quad v(0) = v''(1) + \eta q v(1) = v'(0) = v'''(1) + qv'(1) = 0. \quad (3)$$

Eigenfunctions for adjoint eigenvalue problems (2) and (3) are

$$u(x) = \cosh(ax) - \cos(bx) + \frac{a^2\cosh a + b^2\cos b}{ab(a\sinh a + b\sin b)} \times (a\sin(bx) - b\sinh(ax)), \quad (4)$$

$$v(x) = \cosh(ax) - \cos(bx) + \frac{(a^2+\eta q)\cosh a + (b^2-\eta q)\cos b}{b(a^2+\eta q)\sinh a + a(b^2-\eta q)\sin b} \times (a\sin(bx) - b\sinh(ax)), \quad (5)$$

$$a = \sqrt{-\frac{q}{2} + \sqrt{\frac{q^2}{4} + \lambda - \kappa}}, \quad b = \sqrt{\frac{q}{2} + \sqrt{\frac{q^2}{4} + \lambda - \kappa}}, \quad \kappa \neq \frac{q^2}{4} + \lambda. \quad (6)$$

Eigenvalues λ are solutions to the characteristic equation

$$\Delta(\eta, q, \lambda - \kappa) \equiv (2(\lambda-\kappa) + (1-\eta)q^2) \times (1 + \cosh a\cos b) + q(2\eta - 1)(q + ab\sinh a\sin b) = 0. \quad (7)$$

Solution of the boundary value problem (1) is stable if and only if all the eigenvalues λ of eigenvalue problem (2) are positive and semisimple. If for all $\lambda \in \mathbb{R}$, some of them are negative, then the system is statically unstable (the case of divergence). The existence of at least one $\lambda \in \mathbb{C}$ implies the dynamic instability (flutter).

For given values of the parameters $\eta = \eta_0$, $q = q_0$ and real-valued λ, zeros of the function $\Delta(\lambda - \kappa)$ differ from zeros of $\Delta(\lambda)$ by the quantity κ, while their multiplicities remain the same. Since the flutter boundary is defined by the multiple real-valued eigenvalues, the point (κ, η_0, q_0) belongs to the flutter boundary for arbitrary κ if the point $(0, \eta_0, q_0)$ also belongs to this boundary. The boundary between the stability and divergence domains determined by zero eigenvalues has to change while varying the modulus κ of the elastic foundation, since the eigenvalue $\lambda_0 = 0$ becomes nonzero after the shift $\lambda = \kappa$.

We now find the divergence domain in the Herrmann–Smith problem. Substituting $\lambda = 0$ into both characteristic equation (7) and expressions (6), we obtain

$$\eta(q,\kappa) = \frac{r_2 q - r_1(q^2 - 2\kappa)}{2r_2 q - r_1 q^2}, \quad r_1 = 1 + \cosh a\cos b, \quad r_2 = q + ab\sinh a\sin b. \quad (8)$$

The function $\eta(q, 0)$ attains its maximum $\eta_* = \frac{1}{2}$ at $q_* = (2j+1)^2\pi^2$, $j = 0, 1, \ldots$, whereas $\eta(q, 0) \longrightarrow -\infty$ at the points $q_{**} = (2j)^2\pi^2$ [2]. For arbitrary $\kappa > 0$, the function $\eta(q)$ $(q > 0)$ defined in (8) represents a smooth curve of zero eigenvalues on the plane of the parameters η and q. In this case, the maximum value of η_* and the corresponding value of the parameter q_* change when varying the parameter κ. The numerical solution to the equation $\frac{d\eta}{dq} = 0$ at different values of κ yields the function $q_*(\kappa)$ and [with the use of (8)] $\eta_*(\kappa)$. Knowledge of these functions allows us to find the trajectory in the plane of the parameters η and q of the point $\mathbf{p}_* = (\eta_*, q_*)$ that corresponds, e.g., to the first maximum associated with a change in the parameter κ. The point of the first maximum of the function $\eta(q)$ with an increase in κ moves along the q axis oscillating and tending to the line $\eta = \frac{1}{2}$ as $\kappa \longrightarrow \infty$. It can be shown that all other maxima of the function $\eta(q)$ manifest the same behavior. Therefore, for $\eta > \frac{1}{2}$, the divergence is absent for any $\kappa \geq 0$.

Figure 2 demonstrates stability diagrams for $\eta \in [0, 1]$ and $q \in [0, 150]$. As is seen, within this range of parameters, there exist two curves for double real-valued eigenvalues invariable with respect to the change of the parameter κ. Certain parts of these curves form the flutter boundary (F). The lower curve corresponds to the confluence of the first two eigenvalues, while the

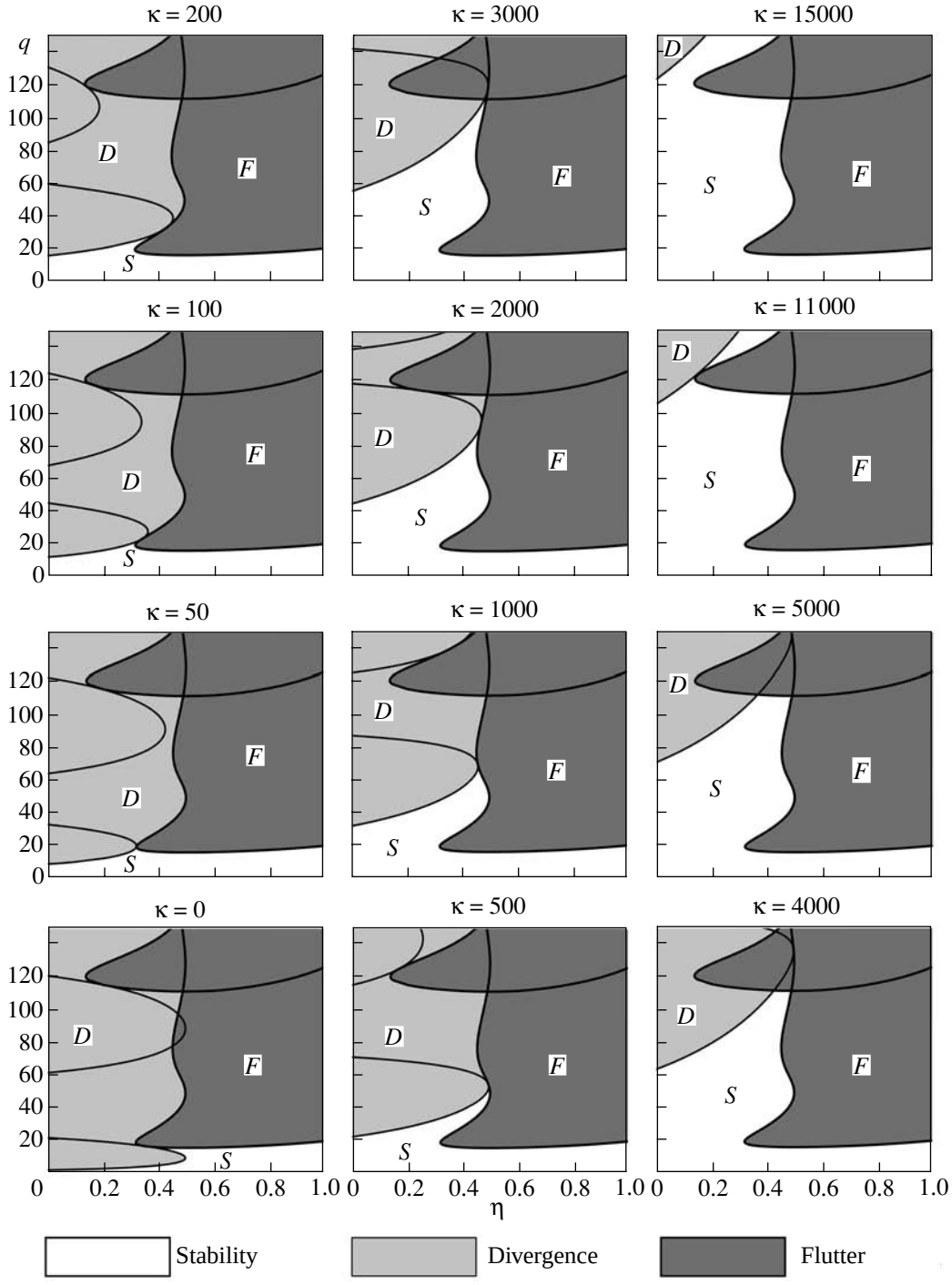

Fig. 2. Shift of the divergence domain due to an increase in the base modulus of rigidity κ.

upper curve corresponds to the coincidence of the third and fourth eigenvalues. In the region of Fig. 2 corresponding to $\kappa < 3000$, there also exist two curves of zero eigenvalues. At the points of the upper curve, the third and the fourth eigenvalues change their sign. The second eigenvalue passes through the zero at the points of the upper part of the lower curve. The part of the lower curve in which the first eigenvalue changes its sign forms the boundary between the stability and divergence domains.

In [2, 10] it was shown that for $\kappa = 0$ at the flutter boundary, there exists a point $\mathbf{p}_0 = (0.35431330, 17.0695748)$ corresponding to the double zero eigenvalue (0^2) at which the curve of the simple zero eigenvalues is tangent to the flutter boundary, Fig. 2. With the increase of the modulus of the elastic foundation,

the flutter boundary preserves its form while the double real-valued eigenvalues linearly change with the variation of κ. As a consequence, the double zero eigenvalue moves along the flutter boundary. Since the curve of the zero eigenvalues and the flutter boundary have the same tangent at the point 0^2, the curves of the zero eigenvalues and the divergence domain travel together with them in the plane of the parameters η and q with the increase in κ clearing the place for the stability domain. This process is reproduced in Fig. 2 for $\kappa \in [0, 15000]$. In the case of $\kappa > 3000$, only the lowest curve of the zero eigenvalues remains within the range $\eta \in [0, 1]$, $q \in [0, 150]$. At $\kappa = 15000$, the divergence domain almost completely goes out of this range, and we have in this region a vast stability domain, as shown in Fig. 2.

Of all publications devoted to the Herrmann–Smith problem, probably only in [8] was the question of the change of the stability diagram in the plane of the parameters η, q while varying the modulus κ of the elastic foundation touched upon. However, the authors of [8] did not find the necessary curves in the parameter plane and omitted the phenomenon of the divergence domain traveling along the flutter boundary. In [2], the stability diagram for $\kappa = 0$ was found without the fragment of the flutter boundary, which corresponds to the negative double eigenvalues since it does not correspond to any physical interpretation [2]. As is seen from Fig. 2, introducing the parameter κ considerably changes the problem, transforming this curve segment into the boundary between the flutter domain and stability domain.

2. SENSITIVITY OF THE CRITICAL LOAD TO THE NONHOMOGENEITY OF AN ELASTIC FOUNDATION

We consider the point $\mathbf{p}_0 = (\kappa_0, \eta_0, q_0)$ on the flutter boundary, which corresponds to the double real eigenvalue λ_0 with the Keldysh chain of length 2. The chain consists of the eigenfunction u_0 and the associated function u_1. The adjoint eigenfunction and associated function of the eigenvalue λ_0 are denoted by v_0 and v_1, respectively. The functions u_0, u_1, v_0, and v_1 can be chosen real-valued. Since the eigenvalue λ_0 has the Keldysh chain, the eigenfunctions u_0 and v_0 are orthogonal: $\int_0^1 u_0 v_0 dx = 0$, [10].

In [3], it was shown that the critical flutter load q_0 in the Herrmann–Smith problem does not depend on the modulus of the uniform elastic foundation κ. We now study the sensitivity of this load with respect to the small inhomogeneity of the base. In doing this, we consider the variation of the rigidity of the elastic foundation $\kappa(x) = \kappa_0 + \delta\kappa(x)$, where $\delta\kappa(x) = \epsilon e_\kappa(x)$ and $\epsilon \geq 0$ is a small parameter. In that case, the parameters η and q take the increments

$$\eta = \eta_0 + \epsilon e_\eta + o(\epsilon), \quad q = q_0 + \epsilon e_q + o(\epsilon).$$

Substituting these variations into the eigenvalue problem (2) and taking into account the expansions

$$\lambda = \lambda_0 + \epsilon^{1/2}\lambda_1 + \epsilon\lambda_2 + \epsilon^{3/2}\lambda_3 + \ldots,$$
$$u = u_0 + \epsilon^{1/2}w_1 + \epsilon w_2 + \epsilon^{3/2}w_3 + \ldots,$$

valid for the double eigenvalue, we arrive at the boundary value problems determining the first coefficients to these expansions:

$$w_1'''' + q_0 w_1'' + \kappa_0 w_1 = \lambda_0 w_1 + \lambda_1 u_0,$$
$$w_1(0) = w_1'(0) = w_1''(1) = w_1'''(1) + (1-\eta_0)q_0 w_1'''(1) = 0; \tag{9}$$

$$w_2'''' + q_0 w_2'' + \kappa_0 w_2 = \lambda_0 w_2 + \lambda_1 w_1 + \lambda_2 u_0 - e_q u_0'' - e_\kappa(x) u_0,$$
$$w_2(0) = w_2'(0) = w_2''(1) = w_2'''(1) + (1-\eta_0)q_0 w_2'''(1) + [e_q(1-\eta_0) - e_\eta q_0]u_0'(1) = 0. \tag{10}$$

After taking the scalar product of Eq. (10) and the eigenfunction v_0 and substituting the solution w_1 of problem (9) into the resulting product, we found the approximate formula describing the splitting of the double real-valued eigenvalue λ_0

$$\lambda = \lambda_0 \pm \sqrt{\frac{(\delta\kappa(x)u_0, v_0)}{(u_0, v_1)} + \frac{q_0 u_0'(1) v_0(1)}{(u_0, v_1)}\Delta\eta + \frac{(u_0'', v_0) - (1-\eta_0)u_0'(1)v_0(1)}{(u_0, v_1)}\Delta q}. \tag{11}$$

Here, $\Delta\eta = \eta - \eta_0$, $\Delta q = q - q_0$ and $(\phi, \psi) = \int_0^1 \phi\bar{\psi}dx$ denotes the scalar product. In the first approximation, the double eigenvalue λ_0 splits due to the variation of the parameters into two simple eigenvalues (stability or divergence depending on the sign of λ_0) if the radicand in formula (11) is positive. If the radicand is negative, then the double eigenvalue λ_0 splits into the complex-

adjoint pair (flutter). Zero radicand in (11) implies the absence of splitting of λ_0. The corresponding condition can be written in the form

$$\Delta q = -\frac{(\delta\kappa(x)u_0, v_0)}{(u_0'', v_0) - (1-\eta_0)u_0'(1)v_0(1)} - \frac{q_0 u_0'(1)v_0(1)}{(u_0'', v_0) - (1-\eta_0)u_0'(1)v_0(1)}\Delta\eta. \quad (12)$$

Formula (12) represents the linear part of the increment of the critical flutter load q_0 while changing the parameter η and the rearrangement of the rigidity of the elastic foundation κ along the column. If the base modulus increases uniformly so that $\delta\kappa = \text{const}$, then

$$\int_0^1 \delta\kappa u_0 v_0 dx = \delta\kappa \int_0^1 u_0 v_0 dx = 0$$

and the flutter load does not depend on the rigidity κ of the uniform elastic foundation.

Introducing the function of the gradient of the critical flutter load with respect to the distribution of the elastic-base modulus $\kappa(x)$

$$g(x) = \frac{-u_0(x)v_0(x)}{\int_0^1 u_0'' v_0 dx - (1-\eta_0)u_0'(1)v_0(1)}, \quad (13)$$

we rewrite formula (12) in the form

$$\Delta q = \int_0^1 g(x)\delta\kappa(x)dx + \frac{\partial q}{\partial\eta}\Delta\eta,$$
$$\frac{\partial q}{\partial\eta} = \frac{-q_0 u_0'(1)v_0(1)}{\int_0^1 u_0'' v_0 dx - (1-\eta_0)u_0'(1)v_0(1)}. \quad (14)$$

We consider, e.g., the point ($\kappa_0 = \text{const}$, $\eta_0 = 1$, $q_0 = 20.0509536$) on the boundary between the flutter domain and stability domain corresponding to the purely tangential follower force. Substituting into (13) the eigenfunctions $u_0(x)$ and $v_0(x)$ evaluated at this point with the use of (4)–(6), we find the gradient function $g(x)$. From Fig. 3, it is seen that the gradient is an oscillating function. Hence, for $\eta_0 = 1$, the column's free end is the most sensitive to a variation of the modulus κ.

We now vary the parameter κ in the gradient direction: $\delta\kappa(x) = \gamma g(x)$. Assuming the parameter η_0 to be fixed and substituting $\delta\kappa(x)$ into (14), we find the approximate expression for the critical flutter load for $\eta_0 = 1$ and $q_0 = 20.0509536$:

$$q = q_0 + \gamma\int_0^1 g^2(x)dx = q_0 + \gamma\cdot 0.00708579.$$

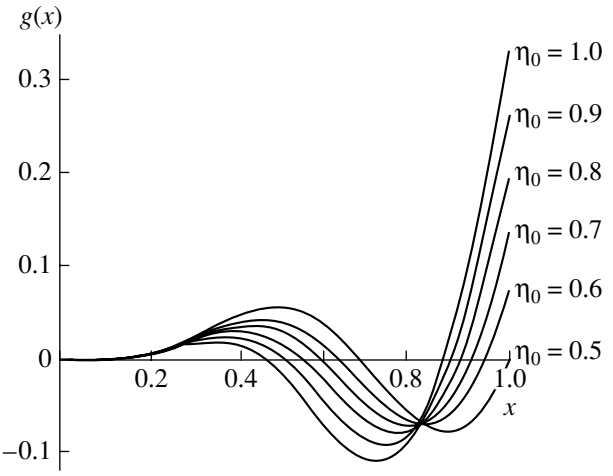

Fig. 3. Gradient function $g(x)$ of the critical flutter load with respect to $\kappa(x)$.

The formula obtained shows that the violation of the uniformity of the elastic foundation can both increase ($\gamma > 0$) and decrease ($\gamma < 0$) the critical flutter load.

ACKNOWLEDGMENTS

This work was supported by the International Association for the Promotion of Cooperation with Scientists from the Independent States of the Former Soviet Union, project no. INTAS YSF 01/1-057.

REFERENCES

1. G. Yu. Dzhanelidze, Tr. Leningr. Politekh. Inst., No. 192, 21 (1958).
2. Z. Kordas and M. Życzkowski, Arch. Mech. Stosow. **15** (1), 7 (1963).
3. T. E. Smith and G. Herrmann, Trans. ASME. J. Appl. Mech. **39** (2), 628 (1972).
4. C. Sundararajan, J. Sound and Vibr. **37** (1), 79 (1974).
5. W. Hauger and K. Vetter, J. Sound and Vibr. **47** (2), 296 (1976).
6. I. I. Voloshin and V. G. Gromov, Izv. Akad. Nauk, Mekh. Tverd. Tela **12** (4), 169 (1977).
7. Ya. G. Panovko and I. I. Gubanova, *Stability and Oscillations of Elastic Systems: Advanced Concepts, Paradoxes, and Errors* (Nauka, Moscow, 1987).
8. S. Y. Lee, J. C. Lin, and K. C. Hsu, Comput. Struct. **59**, 983 (1996).
9. I. Elishakoff and N. Impollonia, Trans. ASME, J. Appl. Mech. **68** (2), 206 (2001).
10. O. N. Kirillov and A. P. Seyranian, in *Proceedings of Seminar on Time, Chaos, and Mathematical Problems, Mosk. Gos. Univ.*, No. 2, 217 (2000).

Doklady Physics, Vol. 47, No. 10, 2002, pp. 772–774. Translated from Doklady Akademii Nauk, Vol. 386, No. 6, 2002, pp. 767–769.

MECHANICS

Decomposition of the Problem of Controlling a Mobile One-Wheel Robot with an Unperturbed Gyrostabilized Platform

Yu. G. Martynenko, A. V. Lenskiĭ, and A. I. Kobrin

Presented by Academician A.Yu. Ishlinskiĭ March 25, 2002

Received April 18, 2002

A mobile one-wheel robot with a gyroscopic stabilization system is investigated both theoretically and experimentally. The equations of motion are separated into the equations of longitudinal and lateral motions. The conditions of imperturbability of the platform of the mobile robot are discussed.

The design of the mobile robot under consideration is based on the analysis of the classical problem of rolling a heavy disc that carries a flywheel and whose rotation axis *Cz* is perpendicular to the disc plane and passes through its center of mass *C* on an absolutely rough horizontal plane [1] (see Fig. 1). The nonholonomic mechanical system "disc + flywheel" has four degrees of freedom and is a gyrostat. Its position is uniquely specified by six generalized coordinates: Euler angles ψ, θ, and φ between the trihedron rigidly bound to the principal central axes of inertia of the disc and stationary trihedron $OX^*Y^*Z^*$, angle γ of the flywheel rotation with respect to the disc about the *Cz* axis, and coordinates x and y of the projection of the disc's center of mass in the plane OX^*Y^*, where the disc rolls. The problem involves three cyclic coordinates ψ, θ, and φ and the energy integral. Thus, the analytical analysis of the equations of motion of a disc with a flywheel reduces to integrating one second-order linear differential equation of the form

$$\frac{d^2y}{d\theta^2} + \cot\theta\frac{dy}{d\theta} - \frac{mr^2I_3}{a_1a_3}y = \frac{mr^2H}{a_1a_3} \qquad (1)$$

in quadratures. Here, $y = \dot\psi\cos\theta + \dot\varphi$ is the projection of the angular velocity of the disc onto its symmetry axis; $H = J_3(\dot\psi\cos\theta + \dot\varphi + \dot\gamma)$ is the kinetic moment of the flywheel; $a_1 = I_1 + J_1$; $a_2 = a_1 + mr^2$; $a_3 = I_3 + mr^2$, I_1, I_3, J_1, and J_3 are the moments of inertia of the disc and flywheel, respectively; and m is the mass of the gyrostat. The change $z = \cos^2\theta$ transforms Eq. (1) into the familiar Gauss hypergeometric equation. The necessary and sufficient conditions of the stability of the steady-state motions of the system make it possible to reveal the effect of the gyrostat on its dynamic behavior and the properties of uncontrollable trajectories. Moreover, the exact integration of the gyrostat equations simplifies the solution to the problem of motion control, because the controlled motion can be assembled from the fragments of free (ballistic) trajectories.

To accelerate, decelerate, and turn the one-wheel robot *Gyrowheel* and to place useful equipment on it, the disc–flywheel system is supplemented by a platform and enclosure which are similar to the outer and inner rings of a universal joint and ensure additional degrees of freedom of the flywheel with respect to the disc. As a result, the system consists of four rigid bodies joined by cylindrical hinges. This system is shown in Fig. 2, where *1* is the wheel, *2* is the platform, and *3* is the enclosure containing the flywheel. The mathematical model of the system is supplemented by two generalized coordinates—the angle α between the platform and the wheel and the angle β between the enclosure and the platform. The platform is inserted into the cylindrical hole inside the wheel with a certain clear-

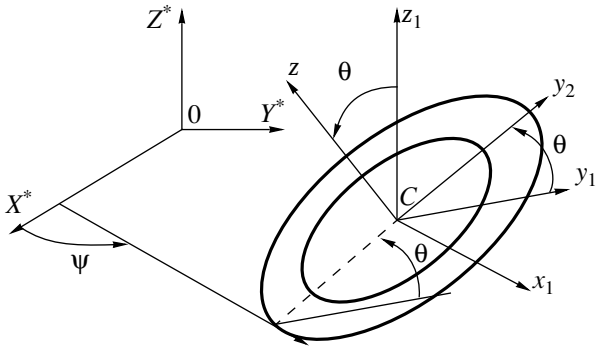

Fig. 1.

Moscow Power Institute, ul. Krasnokazarmennaya 14, Moscow, 111250 Russia
Institute of Mechanics, Moscow State University, Michurinskiĭ pr. 1, Moscow, 117192 Russia

1028-3358/02/4710-0772$22.00

ance filled with small-diameter balls (original-design bearing).

This gyroscopic-stabilization system in the arrangement of the kinetic moment vector coincides with the Brennan scheme of a one-rail railroad [2, p. 213]. In the latter scheme, the kinetic-moment vector is normal to the plane of motion; however, the gyroscope precession axis is vertical, whereas this axis is horizontal in the system under consideration.

The robot's motion is controlled by two dc engines. Engine *4* creates the moment M_α between platform *2* and wheel *1* and, if platform *2* is pendulous, accelerates and decelerates the robot. Engine *5* creates the moment M_β along the precession axis of enclosure *3* (Fig. 2) and, due to the inclination of the wheel, ensures the precession of the kinetic-moment vector about the vertical axis and, therefore, turns the robot.

The generalized-coordinate vector $\boldsymbol{q}_1 = |\psi\theta\varphi\alpha\beta|^T$ satisfies the set of Chaplygin nonlinear differential equations presented in matrix form [3]:

$$\frac{d}{dt}\left(\frac{\partial\Theta}{\partial\dot{\mathbf{q}}_1}\right)^T - \left(\frac{\partial\Theta}{\partial\mathbf{q}_1}\right)^T = \left(\frac{\partial U}{\partial\mathbf{q}_1}\right)^T + \left[\frac{d\mathbf{A}^T}{dt} - \left(\frac{\partial(\mathbf{A}\dot{\mathbf{q}}_1)}{\partial\mathbf{q}_1}\right)^T\right](\mathbf{p}_2 + \mathbf{Q}_U). \quad (2)$$

Here, Θ is the reduced kinetic energy, U is the force function of weight, $\mathbf{A}$ is the matrix in the nonholonomic constraints $|\dot{x}\dot{y}|^T = \mathbf{A}\dot{\mathbf{q}}_1$, $\mathbf{p}_2 = m|\dot{x}\dot{y}|^T$ is the generalized momentum, and $\mathbf{Q}_U = |0\ 0\ 0\ M_\alpha\ M_\beta|^T$ is the vector of the generalized controlling forces. Set (2) in scalar form is a set of nonlinear differential equations of tenth order. To numerically solve this set and visualize it online, a special software package was developed.

In the absence of controlling forces, the equations of motion of system (2) have a particular solution of the form

$$\dot{\psi} = 0, \quad \theta = \frac{\pi}{2}, \quad \dot{\varphi} = \omega, \quad \dot{\alpha} = -\omega, \quad \beta = 0, \quad (3)$$

which corresponds to motion such that the wheel rolls along a straight line, the wheel plane is vertical, the wheel's center moves with the constant velocity $|\omega r|$, the center of mass of the platform is in the lowest position, the enclosure axis is horizontal, and the kinetic-moment vector is normal to the plane of motion.

The linearization near solution (3) decomposes the equations of motion (2) into the sixth-order subset for ψ, θ, and β with the scalar control M_β and fourth-order subset for φ and α with the scalar control M_α. These subsets describe the lateral and longitudinal motions, respectively.

The determinant of the controllability matrix for the linear stationary set describing lateral motion is identically equal to zero; i.e., the lateral-motion set is not completely controllable. The cause is that the lateral-motion set has the first integral expressing the constancy of the kinetic moment about the vertical axis. If the robot can detect the angle β of the flywheel enclosure, the equation of lateral motion can be supplemented by the observer equation $\Delta = \mathbf{h}^T\mathbf{z}$, where $\mathbf{h}^T = |0\ 0\ 0\ 1\ 0|$ and $\mathbf{z}^T = \left|\psi\ \theta\ \dot{\theta}\ \beta\ \dot{\beta}\right|$. A test of the observability conditions indicates that the lateral motion of the gyrowheel is observable in the variables $\dot{\psi}$, θ, β.

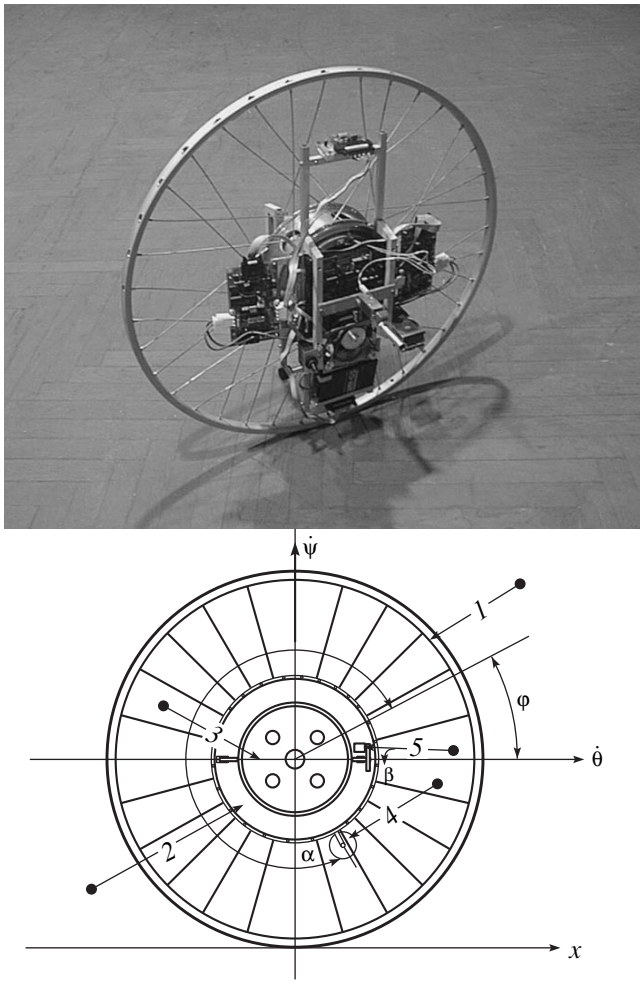

Fig. 2.

The characteristic equation for the equations of uncontrolled lateral motion has one positive, one negative, one zero, and two imaginary roots. Transforming the matrix of the equations of controlled lateral motion to diagonal form, one can estimate the controllability region for the unstable equilibrium position of the lateral-motion set and formulate the requirements for the engine creating the moment along the flywheel-enclosure axis.

The lateral motion of the gyrowheel is investigated with allowance for the effect of the reducer transmitting the engine moment to the wheel. In this case, a moment

that is equal in magnitude but opposite in direction is applied to the platform and induces its angular motion (which is generally not small). The special choice of the parameters of the engine and gyrowheel transmission, in particular, the special choice of the transfer ratios of the gears and reduced moments of inertia ensures the imperturbability of the gyrowheel platform. Let the condition

$$\left(m_1 + m_2 + m_3 + \frac{I_1}{r^2} + \frac{I_p i_1^2}{r^2}\right) r = \frac{I_p i_1 (i_1 + 1)}{r} + m_2 a + m_3 (r_2 + r_3) \quad (4)$$

be valid for a reducer consisting of a pair of gears. Here, m_1, m_2, and m_3 are the masses of the wheel, platform, and gear, respectively; I_p is the gear moment of inertia; a is the distance between the centers of mass of the platform and wheel; r_2 and r_3 are the radii of the platform bearing and gear, respectively; and i_1 is the transfer ratio of the reducer. In this case, the coefficient of the moment created by the engine in the equation for the angle $\sigma = \varphi + \alpha$ determining the deviation of the platform from the vertical is equal to zero. In a certain sense, condition (4) is similar to the condition of the imperturbability of inertial navigation systems [4, 5].

Theoretical investigation and analysis of the actual motion of the one-wheel robot *Gyrowheel*, which was engineered at the Institute of Mechanics, Moscow State University, were carried out at the Moscow Power Institute. As a result, we concluded that the gyroscopic stabilization system of the one-wheel robot is serviceable. Therefore, a mobile one-wheel apparatus performing autonomous controllable motion can be designed.

ACKNOWLEDGMENTS

This work was supported by the Russian Foundation for Basic Research (project no. 00-01-00602) and by the Program “Universities of Russia” (project no. UR.04.01.032).

REFERENCES

1. Yu. G. Martynenko, in *Proceedings of the International Conference on Problems of Mechanics of Advanced Machine, Ulan-Ude, 2000*, Vol. 1, p. 96.
2. B. V. Bulgakov, *Applied Theory of Gyroscopes* (Gos. Izd. Tekh. Teor. Lit., Moscow, 1955).
3. Yu. G. Martynenko, in *Collection of Scientific-Methodical Papers in Theoretical Mechanics* (Mosk. Gos. Univ., Moscow, 2000), No. 23.
4. A. Yu. Ishlinskiĭ, *Orientation, Hyroscopes, and Inertial Navigation* (Nauka, Moscow, 1976).
5. D. M. Klimov, *Inertial Navigation in Sea* (Nauka, Moscow, 1984).

Translated by R. Tyapaev